Computational Aspects of Energy Minimization of the Landau-de Gennes Model for Liquid Crystals

A THESIS
SUBMITTED TO THE FACULTY OF THE GRADUATE SCHOOL
OF THE UNIVERSITY OF MINNESOTA
BY

Paula Andrea Elma Dassbach

IN PARTIAL FULFILLMENT OF THE REQUIREMENTS
FOR THE DEGREE OF
DOCTOR OF PHILOSOPHY

DR. CARME CALDERER AND DR. DOUGLAS ARNOLD

June, 2017

Acknowledgements

There are many people that have earned my gratitude for their contribution to my time in graduate school.

First, I would like to express my appreciation for my advisors Dr. Carme Calderer and Dr. Douglas Arnold. To Dr. Carme Calderer, thank you for your sustained belief in me and your absolute dedication to helping me succeed. I will forever be thankful for the hours spent together discussing mathematics. To Dr. Douglas Arnold, thank you for your steadfast patience and invaluable numerical insight. Our converstions motivated me to continue improving and to, ultimately, become a better mathematician.

Next, I would like to thank my parents. Without their love and support none of this would have been possible.

Finally, Kim and Shay Logan whose unwavering support helped me through some of the toughest obstacles I experienced while in graduate school.

Dedication

To my parents who made me who I am today by teaching me to perservere, inspiring me to continue learning, and supporting me through all of life's journeys.

Contents

List of Tables

List of Figures

Chapter 1

Introduction

Liquid crystals are phases of matter intermediate between crystalline solid and liquid. The ubiquitousness of these partially ordered phases, in both natural and synthetic settings, has had a major impact in the display industry and has also been an important tool in the understanding of soft matter and its role in describing order and function in biology [1].

Materials that show liquid crystal phases usually consist of rod-like elongated and rigid molecules that tend to follow a preferred direction of alignment. In the nematic phase, the molecules have orientational order but their centers of mass of lack positional order [2]. The arrangement of these molecules can be characterized by a unit vector $\boldsymbol{n}$, the director, which describes the average molecular alignment of the liquid crystal molecules in a region.

A central theme in liquid crystal research is the ability to enforce macroscopic-sized regions of uniform molecular alignment, an example of which is found in optical and display devices by electromagnetic fields [3]. Whereas electromagnetic fields for driving liquid crystal alignment have been at the core of liquid crystal research and the ensuing technology, the current trend focuses on topological control, with liquid crystal colloidal systems being at the center of these new directions. Liquid crystal colloidal systems are composed of small insoluable particles suspended in a liquid crystal matrix. These insoluable particles provide surfaces on which alignment can be enforced resulting in the development of complex topologies. The intricate patterns and structure seen in liquid crystal colloids are due to the abundance of many types of defects, i.e., regions in which the director becomes discontinuous.

This Ph.D. dissertation is devoted to the computational study of liquid crystal defects. By first establishing a rigorous mathematical and numerical foundation, we provide accurate computation and visualization of defects, not previously found in literature. Key problems

on the subject are revisited from a rigorous numerical perspective and new solution structures are found that better align with theoretical and experimental data. These methods are then applied to computing the defect structures of colloidal systems.

A signature feature of liquid crystals is the wealth of visual patterns when observed in the optical microscope. These are due to the defects that are present in the long range molecular behavior of the material as observed and first described by Otto Lehman [4] and Georges Friedel [5]. These defects are specific to each liquid crystal phase and serve to classify the liquid crystal phases that are known today. Within these phases, there exist two types of symmetries, uniaxial and biaxial, with molecules tending to follow one or two distinguished directions of alignment, respectively. A great deal of the research in liquid crystals has focused on the study of the detailed structure of the individual defects, the nature of their cores, and the way that groups of defects organize themselves. Early research on liquid crystals focused on uniaxial phases, since the discovery of the biaxial nematic did not occur until 1980 [6].

A landmark fact, relevant to the present thesis, is the realization in 1971 that discs in the plane with radial alignment on the boundaries can have liquid crystal configurations which escape to the third dimension, that is, out of the plane of orientational order [7], [8]. This type of domain was previously believed to have a discontinuity in the director at the center, namely a point defect. Subsequently, a full topological characterization of defects in the nematic phase was carried out in the 1970s by researchers in France [9] and the Soviet Union [10].

Defects can be understood as points or lines where multiple directions of alignment come together, so $\boldsymbol{n}$ becomes undefined. These defects can be classified according to their topological order. For $\mathcal{S}$ any oriented surface and $\boldsymbol{u}$ a mapping from $\mathcal{S}$ onto $\mathbb{S}^2$, there is an integer associated with this map called *the degree or order of* $\boldsymbol{u}$. It is computed through the following formula:

$$\deg(\boldsymbol{u}) = \frac{1}{4\pi} \int_{\mathcal{S}} (\nabla_s \boldsymbol{u})^* \boldsymbol{\nu} \cdot \boldsymbol{u} \; da \tag{1.1}$$

where $(\nabla_s \boldsymbol{u})^*$ is the adjoint of the surface gradient of $\boldsymbol{u}$ on $\mathcal{S}$, $\boldsymbol{\nu}$ is a normal of $\mathcal{S}$, and a denotes the area-measure [2]. Due to the invariance of the liquid crystal properties with respect to changes of $\boldsymbol{n}$ to -$\boldsymbol{n}$, defects of fractional degree $\pm 1/2$ are allowed. These also happen to be very relevant to the research of this dissertation. These defects were called *Mobius defects* by Sir Charles Frank due to their topological equivalence to the Mobius band. A comprehensive outline of research on liquid crystal defects prior to 1980 can be found in the article by Brinkman and Cladis [11].

The first continuum theory of nematic liquid crystals is due to Frank, who in 1958 proposed an elastic energy that penalizes the distortion of the molecular alignment from a preferred equilibrium direction [12]. His work gave a mathematical framework to earlier ideas by Zocher (1925) and Oseen (1933). Also, a very successful theory of nematics is the statistical one proposed by Maier and Saupe [13]. This theory includes contributions from an attractive intermolecular potential from an induced dipole moment between adjacent liquid crystal molecules. This anisotropic attractive force stabilizes parallel alignment of neighboring molecules. The theory considers a mean-field average of the interactions. The most general continuum theory for nematic liquid crystals was introduced by de Gennes in 1974 and developed from the Landau theory of phase transitions. Consistency between this theory and that of Maier-Saupe was not shown until recent work on the latter [14].

In this thesis, we discuss the Oseen-Frank and Landau-de Gennes models focusing on their analogies and subtle differences in order to motivate our choice of model for numerical simulations. The chapters that follow contain computations using FEniCS, a computing platform which uses finite elements to solve PDEs. Much of the past numerical work has relied heavily on the use of simplified models and assumptions, and we take steps to give a more robust numerical view of the behavior and structure of defects in various nematic liquid crystal domains.

From the perspective of liquid crystal models, distortion from the preferred direction of alignment causes the elastic energy to increase. Specifically, point, line, and surface defects are locations with very large elastic energy where the director becomes discontinuous. They often arise as a result of incompatible aligning mechanisms such as those coming from molecular anchoring at the outer and inner boundaries. Controlling surface alignment and the subsequent defects formed in the bulk of the liquid crystal is one main mechanism to control the behavior of the system. There are two main types of *anchoring: strong* and *weak*. The former corresponds to enforcing a molecular alignment on contact boundaries, that is, prescribing Dirichlet boundary conditions on the fields of the problem. In weak anchoring, a surface energy term penalizes departure from the preferred alignment direction imposed by treatment of the surface.

A liquid crystal colloid is a system in which anchoring takes a pivotal role in defect formation. A colloid is a mixture in which microscopically dispersed particles are suspended throughout a liquid crystal. The main defects observed are of topological degrees $+1$, and $-1/2$, with associated defect rings known as *Saturn rings*. These rings are a type of disclination line which have been studied in liquid crystals for decades [15]. Recent experimental and numerical analysis conclude that this is the preferred defect for confined

geometries, which our numerical computations confirm. The core of these defects was once believed to be isotropic, but it was recently discovered that the core is composed of liquid crystals in the biaxial phase [16], an issue explored further in our numerical computations.

We first introduce the Oseen-Frank model in which uniaxial nematic liquid crystal configurations are described by a unit vector field, $\boldsymbol{n}$, the director of the theory. A few deficiencies of this model will be illuminated, starting with the fact that line defects in three dimensions may have infinite energy under the Oseen-Frank description. This model also cannot account for fractional order defects, which are prevalent in colloidal systems. Additionally, since this model can only describe uniaxial liquid crystal alignment, it can result in minimizing configurations which are not observed in physical systems. These issues are resolved with the Landau-de Gennes model.

The inadequacies of the Oseen-Frank model motivated the development of the Landau-de Gennes model. In contrast, the field that describes molecular alignment in the Landau-de Gennes model is a symmetric, traceless, second order tensor Q. Unlike $\boldsymbol{n}$, the tensor Q respects the head-to-tail symmetry of the molecular alignment. Additionally, this model accomodates a description of biaxial phases, and therefore more accurately characterizes liquid crystal defect structures. Another important issue resolved with the use of Q is that of orientability: a line field of a specific degree of smoothness is *orientable* if it can be associated to a unit vector field with the same degree of smoothness. This is not a trivial issue and we easily find liquid crystal configurations which are not orientable, such as the one corresponding to the $-1/2$ order defect. In other words, a line field provides a more accurate description of molecular behavior within the liquid crystal and also allows for more possible minimizing configurations.

Our numerical computations begin by considering a simplified two-by-two tensor Q in the Landau-de Gennes energy and the minimization is done over two-dimensional domains. First, a manufactured solution over an annulus is examined in order to lay the groundwork for the computations that follow. In some domains exact agreement with previous theoretical and numerical work is found, such as the case when particle interactions are considered. For annular domains in which we allow the inner radius to vary, we found that the restriction of Q to purely uniaxial configurations resulted in a digression from previous results since we could only resolve the purely planar radial solution. A pivotal result for this simplified energy concerns the minimization over discs of various radii. In the literature, numerical computations over a disc with normal Dirchlet boundary conditions resulted in a *split core* defect, characterized by two $-1/2$ defects, for radii over a threshold value r_c [17], [18]. By refining the mesh further and studying the convergence of our numerically

approximated solution, we show that this defect structure is an artifact of improper mesh refinement.

We later take Q to be a three-by-three tensor and the numerical computations are done over three-dimensional domains. Again, the method of manufactured solutions establishes a rigorous foundation for the computational work that follows. The two particle domain again gives agreement with previously described experimental and numerical results. There is also a qualitative agreement with the single particle system, but our work contains a more detailed study of the core structure not previously established. Specifically, the analytically established result of Schophol and Sluckin, which states that the core of a Saturn ring defect is uniaxial with negative scalar order parameter, is numerically verified for the first time [19].

For concentric cylinder domains, the minimizing configurations are compared to a fundamental paper by Bethuel, Brezis, and Coleman [20]. Using the Oseen-Frank energy expression, they prove that for $\rho \geq e^{-\pi}$, where ρ is the ratio of the inner to the outer radius, the planar radial configuration is the minimizing configuration. For $\rho < e^{-\pi}$, the *escape solution*, characterized by a non-zero z-component, is the minimizer. Since they consider the Oseen-Frank model, the configurations predicted by the theory are necessarily uniaxial. Every minimizer found in our calculations had some level of biaxial behavior, which is consistent with the theoretical predictions by Biscari and Virga using the Landau-de Gennes energy [21]. In addition, our numerical procedure found three possible minimizing configurations which, unlike the Bethuel et al. minimizers, transitioned continuously to one another.

The effects of using symmetry to simplify three-dimensional calculations are studied in the last chapter. In annular domains, the results are analogous to those seen in the concentric cylinder domains. In domains with particle interactions, this is no longer the case. Projecting uniaxial configurations which cross in three-dimensions onto a two-dimensional domain causes defects to form. For this reason, domains with colloidal particles contained larger defect region when viewing the cross-sectional area and therefore can only give qualitative agreement.

In Chapter 2, we give a mathematical background which includes a description of both the Oseen-Frank and the Landau-de Gennes models. When introducing these models, the complexities and nuances of liquid crystal modeling are discussed. The Chapter ends with a proof of existence of minimizers for the Landau-de Gennes model and the energy is non-dimensionalized. In Chapter 3, we present two-dimensional simulations in a variety of domains using a simplified two-dimensional version of the Landau-de Gennes energy

expression. In Chapter 4, the focus is on fully three-dimensional domains using the full Landau-de Gennes model to find minimizing configurations in a variety of domains with varying boundary conditions. Finally, in Chapter 5, symmetry is used to simplify the three-dimensional domains in order to illustrate that in certain domains, this simplification can only give qualitative agreement.

Chapter 2

Mathematical Background

2.1 What is a Liquid Crystal?

The three most prevalent phases of matter are solid, liquid, and gas, but this list is not exhaustive. Material states differ from one another because the molecules in each state possess distinct amounts of order. In the solid phase, the molecules have both positional and orientational order which are both lost when the material is heated enough to become a liquid. Between the solid and liquid states, certain materials exhibit an intermediate phase in which the molecules have no positional order and diffuse about as in a liquid but maintain some orientational order. These materials have elongated semi-rigid molecules and their order is described in well-known models by a director $\boldsymbol{n}$, which describes the average alignment of these molecules. Since this phase is more ordered than a liquid, but less ordered then a solid, it was given the name liquid cystal.

The optical properties of this material provide a useful way to study liquid crystal behavior. When a liquid crystal is placed between two crossed polarizers the orientational order within the material allows light to pass through certain areas as seen in Figure 2.1. When light passes through a medium, the wavelength and velocity decrease by a factor called the index of refraction. In a liquid crystal, unlike a standard liquid, the index of refraction for polarized light is different in different directions. More specifically, light polarized parallel to the director propagates according to one index of refraction and light polarized perpendicular to the director has another index of refraction. This phenonmenon is called *birefringence* and results in the stunning patterns seen in Figure 2.1.

Birefringence is used to determine molecular alignment in the liquid crystal. This is best understood by studying the director's behavior in the regions in which no light passes

Figure 2.1: Liquid Crystal between Two Cross Polarizers

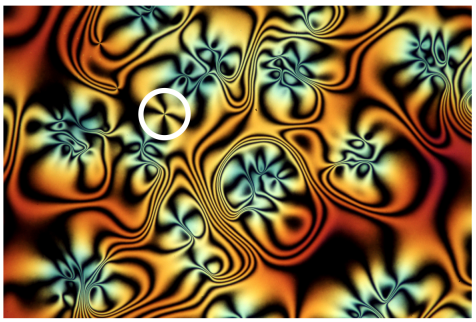

When a thin layer of liquid crystal is placed between two crossed polarizers, varying amount of light can pass though depending on the orientation of the molecules. Notice there is a white circle placed over the top of this image that may not be visible when printed. (Image used with permission of Oleg Lavrentovich [22].)

through. Consider the drawing in Figure 2.2, which describes a liquid crystal between two crossed polarizers. On the bottom plate, the region surrounded by a dashed line denotes a location in the liquid crystal where the director is perfectly aligned with the direction of the bottom polarizer. As light passes through the material, no light is visible in this region on the top plate. This is due to the fact that the light propagates according to a single index of refraction and therefore has no change in polarization. The top plate extinguishes this light and the liquid crystal appears dark in this location [23].

Figure 2.2: Crossed Polarizer Diagram

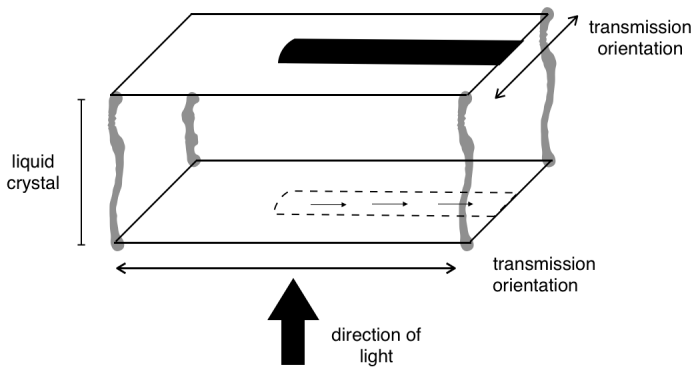

When the director of the liquid crystal is parallel to one of the polarizers, light cannot pass and the result is a black region.

The director in the black regions seen in Figure 2.1 must lie parallel to one of the crossed polarizer. In lighter regions, the directors have components in both directions which allows some light to pass. These optical properties are not just an interesting phenomenon, but can also be controlled through magnetic and electrical fields which attributes to the development of the display devices we interact with on a daily basis.

2.2 Liquid Crystal Colloids

A colloid is a substance in which microscopically small insoluble particles are suspended in a liquid matrix, much like a solution. There are a few defining factors which differentiate a colloid from a solution. In a solution, the amount of particles placed into the surrounding medium is relatively small in comparison with the surrounding liquid mass. Molecular interactions oftentimes break apart the particles. Because of this, the size of the resulting particles is approximately the same order of magnitude as molecules in the surrounding liquid. In comparison, within a colloid, the particles retain their shape and are large compared with the molecules in the surrounding medium. In the colloids of interest, the particle size varies between 1 and 1000 nanometers. The relatively large size of the particles, in this case, implies that the volume taken up by the particles is of the same order of magnitude as the volume of the surrounding fluid. One last differentiating characteristic is that in a colloid, one is able to separate the particle from the surrounding fluid medium, while in a solution this is not the case [24].

We are interested in modeling colloids in which the surrounding medium is a liquid crystal. In order to better understand liquid crystal colloids, let us describe how they differ from a colloid composed of a standard liquid. A classic example of a standard colloid is milk. The particles are the milkfat globules dispersed in a water-like substance. They move around the surrounding medium fairly freely, bouncing off one another and the walls. There is minimal constraint on motion, but this is not the case in liquid crystal based colloids. By controlling the boundary conditions on the walls of the liquid crystal container, defects form in the liquid crystal. These defects are seen experimentally through their optical effects and described mathematically as regions where there is no longer one preferred direction of alignment for the molecules. The formation of defects around colloidal particles results in a net particle-particle separation, as well as a separation between the particles and the walls of the container. When multiple particles are present, the defects in the liquid crystal are ubiquitous and cause the particles in the liquid crystal to lock together to create chains of particles. Since the behavior of a liquid crystal colloid varies substantially from that of a

standard colloid, a material with new properties often emerges. There are two main steps in understading colloid behavior, the first being the unraveling of the interaction between a single particle and the liquid crystal. The second ingredient is the interplay between two particles. The first type of interaction is a direct result of the anchoring property of a liquid crystal molecule with a solid surface. Many techologies have been developed to enforce a preferred angle between the molecules and the surface normal, tangential and perpendicular (*homeotropic*) being the standard ones. In many instances, the anchoring property, instead of being formulated as a Dirichlet boundary condition, referred to as *strong anchoring*, enters the model as a surface energy penalty, known as *weak anchoring*.

2.3 Historical Background: Modeling Liquid Crystals

The Oseen-Frank model was the first widely accepted static model for liquid crystal energy and it consists of five terms which are dependent on a vector field, that describes the director, and its derivative multiplied by elastic constants, which are material parameters. The model was first introduced by Oseen in 1932, but in 1958 Frank discovered some inaccuracies with the model coefficients and proposed a revised version [25], [12]. The existence of solutions in the Oseen-Frank model and their partial regularity were established many years later by Hardt, Kinderlehrer, and Lin in 1986 [26].

Experimental evidence suggested that in addition to point defects, liquid crystals also present line defects, called *disclinations*, which are lines along which the optical director $\boldsymbol{n}$ is singular. As we will show in a later section, the Oseen-Frank energy diverges in these types of defect locations. In 1985, J.L. Ericksen proposed that this difficulty be circumvented by modifying the Oseen-Frank model and permitting variations of the degree of orientation quantified by the order parameter s [27]. Existence, local uniqueness, and global regularity for this model were established in 1991 by Lin [28]. Defect regions were now described by $s = 0$, implying that these are locations where the material becomes isotropic. Later experimental evidence and theory suggests that the defect regions may not be regions of isotropic melt, but instead locations where there are two preferred directions of alignment, a phenomenon referred to as biaxiality. Neither the Oseen-Frank nor the Ericksen model can account for this behavior.

The most general continuum theory for nematic liquid crystals developed, from the Landau theory of phase transitions, was introduced by de Gennes in 1974 [29]. He proposed a Ginzburg-Landau expansion for the free energy of the liquid crystal near the point of

nematic-isotropic phase transition and that molecular orientation be described by a symmetric traceless tensor. In the case that two eigenvalues of the tensor are equal and distinct from the third one, the eigenvector associated with the latter roughly corresponds to the director field $\boldsymbol{n}$ of the Oseen-Frank Theory. Unlike the models previously developed, the Landau- de Gennes model accounts for both line defects and biaxiality, and is one of the major reasons de Gennes was awarded a Nobel prize for physics in 1991. Over twenty years after its introduction, in 1998, Davis and Gartland established existence and regularity of the Landau-de Gennes model [30]. While this model encompasses all the behavior observed in liquid crystal domains, its added complexity has hindered its total adoption.

In this thesis, the Oseen-Frank model will be used to illustrate some of the subtleties and complexities of liquid crystal modeling. Once there is a better understanding of the relevant issues and short-coming of this model, the Landau-de Gennes model will be introduced and a detailed description will be given. Existence will be established and all of the numerical computations will be done using the Landau-de Gennes model.

2.4 Liquid Crystal Defects and Their Order

Defects are characterized by regions in which there is no well-defined direction of average molecular alignment, i.e., a discontinuity in the director. Experimentally, the presence of defects is identified by the behavior of the liquid crystal placed in crossed polarizers as illustrated in Section 2.1. Let us consider the circular region in Figure 2.1. As described, the black regions denote locations in which the director is aligned parallel to one of the polarizers. The lighter regions give us locations in which the director has components in the directions of both polarizers. At the very center, where these various regions of alignment meet, the director cannot be defined. This is labeled as a defect being present in the liquid crystal. Note that these defects are not confined to plane-like regions, but also occur in three-dimensions and result in entire lines, called *disclinations*, or surfaces where the molecular orientation is lost.

The presence of a defect results from an alignment incompatibility between the prescribed anchoring direction of the liquid crystals on different surfaces in the domain. There are two types of molecular alignments that can be enforced on the domain surfaces: *weak anchoring* and *strong anchoring*. These are imposed by treating the surface with a surfactant or by rubbing it in a set direction in order to align the liquid crystal molecules. Mathematically, strong anchoring is represented by defining a Dirichlet boundary condition and will be reflected in the choice of admissible set. Weak anchoring is taken into account

by inducing a surface penalty term in the energy. Later, we will introduce an expression for the weak anchoring energy, but in our numerical computations only strong anchoring will be considered.

Defects can be classified according to their topological order. Assume $\mathcal{S}$ is any oriented surface and $\boldsymbol{u}$ is a mapping from $\mathcal{S}$ onto $\mathbb{S}^2$. There is an integer associated with this map called *the degree or order of* $\boldsymbol{u}$. It can be computed through the following formula:

$$\deg(\boldsymbol{u}) = \frac{1}{4\pi} \int_{\mathcal{S}} (\nabla_s \boldsymbol{u})^* \boldsymbol{\nu} \cdot \boldsymbol{u} \, da \tag{2.1}$$

where $(\nabla_s \boldsymbol{u})^*$ is the adjoint of the surface gradient of $\boldsymbol{u}$ on $\mathcal{S}$, $\boldsymbol{\nu}$ is a normal of $\mathcal{S}$, and a denotes the area-measure [2]. Intuitively, this order is found by intersecting the defect with a plane, considering a 2π rotation around the defect, and measuring the corresponding change in angle of the director. In other words, the order k defines the $2\pi k$ change of the angle in the director as we move around the defect. To better understand how the degree of a defect is calculated, consider Figure 2.3.

Figure 2.3: Defect Orders

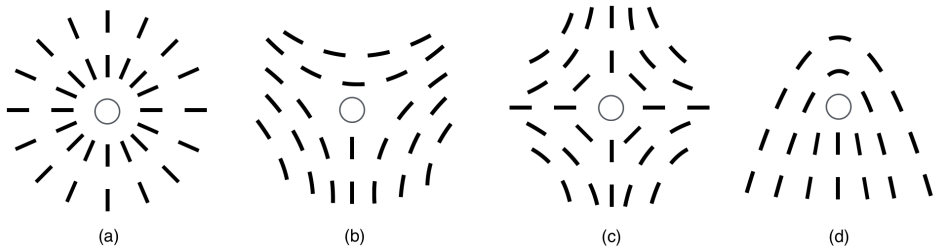

In the images above, the defect is denoted by a circle in the center. (a) shows a $+1$ defect since during a 2π rotation around the defect region the direction of the molecules also completes a 2π rotation. By similar analysis, (b) is a $-1/2$ ordered defect, (c) a -1 ordered defect and (d) a $1/2$ defect.

In the case of a single spherical particle with radial alignment in a uniformly aligned cell, the far-field behavior has order zero, i.e., a zero topological charge. By the conservation law, the interior must also have a zero charge. The radial alignment on the particle surface forms a $+1$ charge and, therefore, the liquid crystal must have defects in the bulk which sum to -1. Experiments have shown that there are two possibilities, the hedgehog or the Saturn ring defect, and their occurence depends on a variety of factors such as the strength of alignment, confinement, and the size of the particles in unconfined domains. The hedgehog is characterized by a -1 order and the Saturn ring corresponds to two $-1/2$ defects. Figure

2.4 provides a two-dimensional sketch of these defects.

Figure 2.4: Single Particle Defects

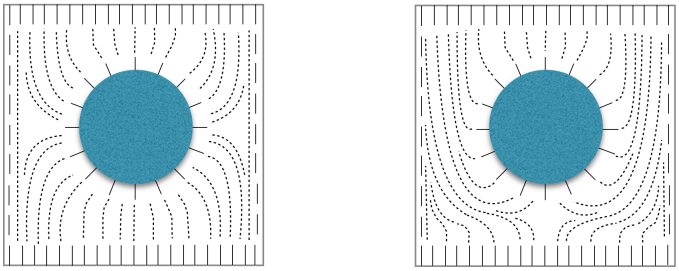

These diagrams represent a two-dimensional cross section of the possible defect behavior for a single particle in a uniformly aligned cell. The hedgehog defect is shown on the left and on the right the Saturn ring defect is shown. Note that in three dimensions, the Saturn ring will be a defect region which wraps around the entire colloidal particle.

Such configurations have been verified in a number of articles both experimentally [31],[32], [33], [34], [35], [36] and numerically with the use of Oseen-Frank model, [37], [38], [39], and to some extent using the Landau-de Gennes energy expression [40],[41], [42], [43], [44], [45], [46], [47], [48], [49], [50]. More specifically, experimental evidence suggest that in confined domains a single particle with normal liquid crystal alignment on the surface will result in a Saturn ring, which will be verified numerically in the following chapters [31], [33].

2.5 Oseen-Frank Theory and the Existence of a Minimizer

Now that the physical background of liquid crystals has been established, we introduce and discuss the first most widely used models for liquid crystal energy: The Oseen-Frank model. Although this is not the model used in simulations, it is useful for illustrating some of the subtleties in modeling liquid crystal systems. In this model, the orientation of the molecules is described by a unit vector, $\boldsymbol{n}$, called the director. As stated previously, this vector gives the average direction of molecular alignment. The equilibrium states of a nematic liquid crystal are minimizers of the following total energy:

$$E_{OF}(\boldsymbol{n}) = \int_{\Omega} W(\nabla \boldsymbol{n}, \boldsymbol{n})\, d\boldsymbol{x},\ |\boldsymbol{n}| = 1, \tag{2.2}$$

where

$$W(\nabla \boldsymbol{n}, \boldsymbol{n}) = k_1(\nabla \cdot \boldsymbol{n})^2 + k_2(\boldsymbol{n} \cdot \nabla \times \boldsymbol{n})^2 + k_3|\boldsymbol{n} \times \nabla \times \boldsymbol{n}|^2 \\ +(k_2 + k_4)(\text{tr } (\nabla \boldsymbol{n})^2 - (\nabla \cdot \boldsymbol{n})^2), \tag{2.3}$$

$\Omega \in \mathbb{R}^3$ is the open bounded region with smooth boundary occupied by the liquid crystal, and the Frank constants, k_i, are experimentally measured [12], [2]. Note that the unit director constraint $|\boldsymbol{n}| = 1$ results in a non-convex admissible set. Before delving into the nuances of modeling liquid crystal systems, the existence of a minimizer for this energy expression is established. Let us begin by assuming:

$$k_1, k_2, k_3 > 0, \ k_2 \geq |k_4|, \text{ and } \ 2k_1 \geq k_2 + k_4 \tag{2.4}$$

and present a classical result from Hardt, Kinderlehrer, and Lin [26]. Their paper proves the existence of global minimizer for the Oseen-Frank energy expression and also contains some partial regularity results. Here, we present the results concerning the existence of a minimizer and point out some relevant issues in the proofs. Let

$$H^1(\Omega, \mathbb{S}^2) = \{\boldsymbol{u} \in H^1(\Omega, \mathbb{R}^2) : |\boldsymbol{u}| = 1 \text{ a.e. in } \Omega\},$$

and define our admissible to be

$$\mathcal{A}(\boldsymbol{n}_0) = \{\boldsymbol{u} \in H^1(\Omega, \mathbb{S}^2) : \boldsymbol{n}_0 = \text{ trace of } \boldsymbol{u} \text{ on } \partial\Omega\}$$

The goal is to show that there is an $\boldsymbol{n} \in \mathcal{A}(\boldsymbol{n}_0)$ such that

$$E_{OF}(\boldsymbol{n}) = \inf_{\boldsymbol{u} \in \mathcal{A}(\boldsymbol{n}_0)} E_{OF}(\boldsymbol{u}) < \infty$$

To accomplish this, weak lower semi-continuity of the energy functional and coerciveness in $\mathcal{A}(\boldsymbol{n}_0)$ are required. Let us begin by ensuring that the admissible set is nonempty. This is established by the first lemma in Hardt et al.

Lemma 2.5.1. ([26], lemma 1.1): *If $\boldsymbol{n}_0 : \partial\Omega \to \mathbb{S}^2$ is Lipschitz, then the family $\mathcal{A}(\boldsymbol{n}_0)$ is nonempty.*

We observe that the first three terms of the energy in (2.3) are positive. However, to establish that the energy is bounded from below, we need to focus on the $(k_2 + k_4)$ term. For this, consider the following identity:

$$\text{tr } (\nabla \boldsymbol{n})^2 - (\nabla \cdot \boldsymbol{n})^2 = \nabla \cdot [(\nabla \boldsymbol{n})\boldsymbol{n} - (\nabla \cdot \boldsymbol{n})\boldsymbol{n}]$$

Applying this identity to the last term in $W(\nabla \boldsymbol{n}, \boldsymbol{n})$, it can be written as a pure divergence, which further implies the following lemma.

Lemma 2.5.2. ([26], lemma 1.2): *For any Lipschitz function* $\boldsymbol{n}_0 : \partial\Omega \to \mathbb{S}^2$*, there is a number* $\mathcal{S}(\boldsymbol{n}_0)$ *such that for all* $\boldsymbol{u} \in \mathcal{A}(\boldsymbol{n}_0)$

$$\mathcal{S}(n_0) = \frac{1}{2}\int_\Omega [\mathrm{tr}(\nabla \boldsymbol{u})^2 - (\nabla \cdot \boldsymbol{u})^2]\ d\boldsymbol{x} \tag{2.5}$$

In the case of strong anchoring with $\boldsymbol{n}_0$ prescribed, this term depends completely on boundary data, $\boldsymbol{n}_0$, and its tangential derivatives. For this reason, when Dirichlet boundary conditions are considered, this term is often set equal to zero by setting $k_2 = -k_4$. Of course, this is not the case for weak anchoring.

Let us now consider the modified expression

$$\widetilde{E_{OF}}(\boldsymbol{u}) = \int_\Omega \widetilde{W}(\nabla \boldsymbol{u}, \boldsymbol{u})\ d\boldsymbol{x}, \tag{2.6}$$

where

$$\begin{aligned}\widetilde{W}(\nabla \boldsymbol{u}, \boldsymbol{u}) &= W(\nabla \boldsymbol{u}, \boldsymbol{u}) + (\alpha - k_2 - k_4)(\mathrm{tr}\ (\nabla \boldsymbol{u})^2 - (\nabla \cdot \boldsymbol{u})^2) \\ &= k_1(\nabla \cdot \boldsymbol{u})^2 + k_2(\boldsymbol{u} \cdot \nabla \times \boldsymbol{u})^2 \\ &\quad + k_3|\boldsymbol{u} \times \nabla \times \boldsymbol{u}|^2 + \alpha(\mathrm{tr}\ (\nabla \boldsymbol{u})^2 - (\nabla \cdot \boldsymbol{u})^2)\end{aligned} \tag{2.7}$$

with $\alpha = \min\{k_1, k_2, k_3\}$. This new energy expression and the original expression are simultaneously minimized:

Corollary 2.5.3. ([26], Corollary 1.3): *For any Lipschitz function* $\boldsymbol{n}_0 : \partial\Omega \to \mathbb{S}^2$ *and* $\boldsymbol{n} \in \mathcal{A}(\boldsymbol{n}_0)$*,* $\boldsymbol{n}$ *minimizes* E_{OF} *in* $\mathcal{A}(\boldsymbol{n}_0)$ *if and only if* $\boldsymbol{n}$ *minimizes* $\widetilde{E_{OF}}$ *in* $\mathcal{A}(\boldsymbol{n}_0)$*.*

Proof. For any $\boldsymbol{u} \in \mathcal{A}(\boldsymbol{n}_0)$, from Lemma 3.2, we have that

$$\begin{aligned}\widetilde{E_{OF}}(\boldsymbol{u}) - \widetilde{E_{OF}}(\boldsymbol{n}) &= E_{OF}(\boldsymbol{u}) + (\alpha - k_2 - k_4)\mathcal{S}(\boldsymbol{n}_0) \\ &\quad - (E_{OF}(\boldsymbol{n}) + (\alpha - k_2 - k_4)\mathcal{S}(\boldsymbol{n}_0)) \\ &= E_{OF}(\boldsymbol{u}) - E_{OF}(\boldsymbol{n})\end{aligned}$$

□

From the following Lemma, it will be clear that this new integrand has the properties required for energy minimization.

Lemma 2.5.4. ([26], lemma 1.4): $\frac{1}{2}\alpha|\nabla \boldsymbol{u}|^2 \leq \widetilde{W}(\nabla \boldsymbol{u}, \boldsymbol{u}) \leq \beta|\nabla \boldsymbol{u}|^2$ *for* $\beta = 3(k_1 + k_2 + k_3)$ *and* $\boldsymbol{u} \in H^1(\Omega, \mathbb{S}^2)$*. Furthermore,* $\widetilde{E_{OF}}$ *is weak lower semi-continuous in* $H^1(\Omega, \mathbb{S}^2)$*.*

Existence of a minimizer for the Oseen-Frank energy can now be established:

Theorem 2.5.5. ([26], Theorem 1.5): *For any Lipschitz function* $\boldsymbol{n}_0 : \partial\Omega \to \mathbb{S}^2$*, there exists an* $\boldsymbol{n} \in \mathcal{A}(\boldsymbol{n}_0)$ *such that* $E_{OF}(\boldsymbol{n}) = \inf_{\boldsymbol{u}\in\mathcal{A}(\boldsymbol{n}_0)} E_{OF}(\boldsymbol{u})$.

Proof. Assume that $\boldsymbol{n}_k$ is a minimizing sequence of $\widetilde{E_{OF}}$ in $\mathcal{A}(\boldsymbol{n}_0)$. By Lemma 2.5.4, this sequence is bounded in H^1 and therefore there exists a weakly convergent subsequence where $\boldsymbol{n}_{k_j} \rightharpoonup \boldsymbol{n}$ in $H^1(\Omega, \mathbb{R}^2)$. This sequence converges strongly in L^2, since H^1 is compactly embedded in L^2, and by the property of traces $\boldsymbol{n} \in \mathcal{A}(\boldsymbol{n}_0)$. By weak lower semi-conitinuity in Lemma 2.5.4, $\widetilde{E_{OF}}(\boldsymbol{n}) = \inf_{\boldsymbol{u}\in\mathcal{A}(\boldsymbol{n}_0)} \widetilde{E_{OF}}(\boldsymbol{u})$, and the Theorem follows from Corollary 2.5.3. □

In addition to existence, Hardt, Kinderlehrer, and Lin also prove the following regularity result:

Theorem 2.5.6. ([26], Theorem 2.6): *If* $\boldsymbol{n} \in H^1(\Omega, \mathbb{S}^2)$ *is a minimizer of* E_{OF}*, as in (2.2), then* $\boldsymbol{n}$ *is analytic on* Ω/Z *for some relatively closed subset of* Z *of* Ω *which has a one-dimensional Hausdorff measure zero.*

These sets of measure zero are exactly defect locations in the liquid crystal. While the existence of a minimizer for the Oseen-Frank model is guaranteed and the liquid crystal is necessarily well-behaved away from these defect regions, this model may not be the most appropriate for studying the minimizing configurations for domains with larger defect regions. Notice the regularity result only allows for point defects in the theory, but line defects may occur which will have infinite energy when described in the Oseen-Frank model, as will be discussed further in the section to follow. Furthermore, the use of this model necessarily implies that there is one preferred direction of alignment in the bulk of the liquid crystal. This may not always be the case and numerical computations in Chapter 3 and 4 will show that this assumption fails to capture some of the behavior seen in certain liquid crystal domains.

2.6 Defects in the Oseen-Frank Model

In Section 2.4, defects were described as locations in which the director became singular. It of interest how these singular regions are reflected in the Oseen-Frank model. Consider the case where $k_1 = k_2 = k_3 = K$ and $k_4 = 0$. Under these assumptions, energy (2.2) reduces to a Dirchlet integral:

$$E^*_{OF}(\boldsymbol{n}) = K \int_\Omega |\nabla \boldsymbol{n}|^2 \, d\boldsymbol{x}. \tag{2.8}$$

This simplified version is referred to as the *one-constant approximation of the Oseen-Frank energy* and helps provide intuition about the behavior of the full model. Suppose that the liquid crystal domain, $\Omega \in \mathbb{R}^n$, $n = 2, 3$, is a ball of radius one centered at the origin, and such that the director has the form $\boldsymbol{n} = \boldsymbol{x}/|\boldsymbol{x}|$. From Figure 2.3, it is clear that this configuration results in the degree one defect at the origin which is referred to as the hedgehog defect. First, assume $n = 3$. We begin by converting our energy integral to spherical coordinates using

$$\begin{aligned}
\frac{\partial}{\partial x} &= \sin\theta\cos\phi\frac{\partial}{\partial r} + \frac{\cos\theta\cos\phi}{r}\frac{\partial}{\partial\theta} - \frac{\sin\phi}{r\sin\theta}\frac{\partial}{\partial\phi} \\
\frac{\partial}{\partial y} &= \sin\theta\sin\phi\frac{\partial}{\partial r} + \frac{\cos\theta\sin\phi}{r}\frac{\partial}{\partial\theta} + \frac{\cos\phi}{r\sin\theta}\frac{\partial}{\partial\phi} \\
\frac{\partial}{\partial z} &= \cos\theta\frac{\partial}{\partial r} - \frac{\sin\theta}{r}\frac{\partial}{\partial\theta}
\end{aligned}$$

where $x = r\cos\phi\sin\theta$, $y = r\sin\phi\sin\theta$, and $z = r\cos\theta$, $0 < \theta < \pi$, $0 < \phi < 2\pi$. Evaluating the energy gives:

$$\begin{aligned}
E^*_{OF}\left(\frac{\boldsymbol{x}}{|\boldsymbol{x}|}\right) = K\int_{B_1(0)}\frac{3}{|\boldsymbol{x}|^2}\,d\boldsymbol{x} &= K\int_0^1\int_0^{2\pi}\int_0^{\pi}\frac{3}{r^2}r^2\sin\theta\;d\theta d\phi dr \\
&= 6\pi K\int_0^{\pi}\sin\theta\;d\theta = 12\pi K.
\end{aligned}$$

This implies that the hedgehog defect in a three dimensional domains has a finite energy. Now, consider that same defect in two dimensions:

$$E^*_{OF}\left(\frac{\boldsymbol{x}}{|\boldsymbol{x}|}\right) = K\int_{B_1(0)}\left|\nabla\left(\frac{\boldsymbol{x}}{|\boldsymbol{x}|}\right)\right|^2 d\boldsymbol{x} = K\int_{B_1(0)}\frac{2}{|\boldsymbol{x}|^2}\,d\boldsymbol{x}.$$

Rewritting the integral in polar coordinates (r, θ):

$$E^*_{OF}(\boldsymbol{n}) = K\int_0^{2\pi}\int_0^1\frac{2}{r^2}r\;drd\theta = 4\pi K\ln r\Big|_0^1$$

Clearly, this two dimensional configuration will have infinite energy. This structure would correspond to the two-dimensional cross section of the line defect hypothesized to exist for a cylinder with radial planar alignment on its lateral boundaries [51], [7],[52]. The infinite energy of some line defects in the Oseen-Frank energy was a motivating factor for developing other liquid crystal models. The later models were more complicated and therefore the Oseen-Frank model was still used for analytic studies and numerical computations. In these cases, an infinite energy value was avoided by removing a small area around the defect and assigning an energy value to this removed volume, but these manipulations were artificial

and not ideal for truly understanding the liquid crystal system even if for certain domains they gave qualitative understanding. We note, that an infinite energy for this configuration may not be as inaccurate as once considered. More recent works hypothesize that the capillary with planar radial alignment on the lateral boundaries may never have the planar radial solution as the minimizing configuration. This implies that the configuration resulting in a central line defect is not energetically favorable, an issue which will be discussed further in Chapters 3, 4, and 5.

2.7 Liquid Crystal Alignment: Biaxial vs. Uniaxial

We now give a description of the types of symmetry of the nematic phase and how they affect the nature of defects. These three types of symmetry associated with the bulk arangements are *isotropic, unaxial* and *biaxial*. The state in which there is no preferred direction of alignment is referred to as isotropic. In the uniaxial symmetry, the molecules are aligned along a single preferred direction and are therefore rotationally symmetric. Since there is a single direction governing anisotropy, rotating the material around this preferred direction does not change optical behavior. In a biaxial system, there are two preferred directions of alignment and rotational symmetry is lost. There are instead two perpendicular axes which allow for reflectional symmetry and, therefore, two optical axes along which light can propagate without birefringence [53]. It was not until nearly 100 years after the discovery of the liquid crystal phase that the biaxial symmetry was theoretically predicted by Freiser in 1970 [54]. This theory was later experimentally confirmed in 1980 by Yu and Saupe [6].

The Oseen-Frank theory solely models uniaxial liquid crystal phases. Since biaxial phases are known to occur in liquid crystals, this model cannot capture all the behavior seen in liquid crystal domains. Additionally, this theory necessarily describes defect regions as locations where the liquid crystal becomes isotropic. While it was originally believed that the Saturn ring, as shown in Figure 2.4, was a region in which the liquid crystal became isotropic, later papers contested this assumption. Kralj, Virga, and Zumer explain, in [16], that the Saturn ring is not a line along which the liquid crystal becomes isotropic, but instead a torus in which the liquid crystal becomes biaxial in contrast to the uniaxial behavior in the surrounding medium. More specifically, Schopohl and Sluckin in [19] discuss that all defects cores have a region of biaxiality surrounding a core which is uniaxial with negative scalar order parameter. When the order parameter is negative, the particles align in a plane perpendicular to the order parameter and can appear to have an isotropic or biaxial behavior. An important contribution of this thesis is the numerical verification of

this core structure which will be presented in Chapters 4 and 5.

2.8 Detailed Description of the Tensor Order Parameter Q

We now introduce the order tensor Q, which is the main variable of the Landau-de Gennes theory. This tensor describes molecular alignment in a way that respects the head-to-tail symmetry of the molecules and allows for biaxial alignment. In order to define this tensor, we begin with a probability measure $\mu(p)$. At each point in the region occupied by the liquid crystal, $\mu(p)$ gives the probability that the molecules in a given small neighborhood point in the direction p. The head-to-tail symmetry of the models results in a zero-valued first moment and the first non-trivial information on μ comes from the second moments. Define

$$M := \int_{\mathbb{S}^2} p \otimes p \; d\mu(p).$$

If the nematic liquid crystal is isotropic, then $d\mu(p) = \frac{1}{4\pi} dA$ and

$$M_0 := \frac{1}{4\pi} \int_{\mathbb{S}^2} p \otimes p \; dA = \frac{1}{3} Id.$$

The de Gennes order-parameter tensor is defined to be:

$$Q := M - M_0.$$

Since Q is a symmetric and traceless the most general form, when the liquid crystal alignment is biaxial, is given by:

$$Q = \lambda_1 \boldsymbol{n}_1 \otimes \boldsymbol{n}_1 + \lambda_2 \boldsymbol{n}_2 \otimes \boldsymbol{n}_2 + \lambda_3 \boldsymbol{n}_3 \otimes \boldsymbol{n}_3 \tag{2.9}$$

where $\{\boldsymbol{n}_i\}$ is an orthonormal basis of eigenvectors for Q with corresponding eigenvectors $\lambda_1, \lambda_2, \lambda_3$ and $\lambda_1 + \lambda_2 + \lambda_3 = 0$ with $-1/3 \leq \lambda_i \leq 2/3$. The alignment of the molecules is encoded in the behavior of these eigenvalues. When $\lambda_1 > \lambda_2 > \lambda_3$, the liquid cystal exhibits the biaxial state. In this case, molecular alignment is not rotationally symmetric around a single preferred direction. If $\lambda_1 > 0 > \lambda_2 = \lambda_3$ the liquid crystal is uniaxial with positive scalar order parameter λ_1. Here, the unique preferred direction is given by the eigenvector associated to λ_1 and the thermal vibrations of the molecules are rotationally symmetric about this direction. For $\lambda_3 < 0 < \lambda_2 = \lambda_1$, the liquid crystal is said to be unaxial with negative scalar order parameter. For this state, the molecules prefer to align themselves in the plane perpendicular to the eigenvector associated with λ_3. This alignment does not

have a well-defined direction on the plane and results in a very disordered state confined to a planar region.

Expression (2.10) is often rewritten in the following form

$$Q = s(\boldsymbol{n} \otimes \boldsymbol{n} - \frac{1}{3}I) + r(\boldsymbol{m} \otimes \boldsymbol{m} - \frac{1}{3}I), \tag{2.10}$$

where $\boldsymbol{n} = \boldsymbol{n}_1$, $\boldsymbol{m} = \boldsymbol{n}_2$, and the order parameters $s, r \in \mathbb{R}$, with $s = 2\lambda_1 + \lambda_2$, and $r = \lambda_1 + 2\lambda_2$. For the biaxial alignment, the two eigenvector $\boldsymbol{n}$ and $\boldsymbol{m}$ give the two preferred directions of alignment for the biaxial phase. The parameters r and s give the quality of alignment respectively. Note that the definition of Q is independent of whether we choose to describe alignment with $\boldsymbol{n}$ and $\boldsymbol{m}$ or the negative of these vectors, respecting the head-to-tail symmetry of the molecules. Since $\boldsymbol{n}$ and $\boldsymbol{m}$ are of unit length, letting θ, ϕ, and ψ denote the Euler angles, we write these directors in the following way:

$$\boldsymbol{n} = (\cos\theta\cos\phi, \cos\theta\sin\phi, \sin\theta). \tag{2.11}$$

Since $\boldsymbol{m}$ is perpendicular to $\boldsymbol{n}$:

$$\boldsymbol{m} = (\sin\phi\cos\psi - \cos\phi\sin\psi\sin\theta, -\sin\phi\sin\psi\sin\theta - \cos\phi\cos\psi, \sin\psi\cos\theta) \tag{2.12}$$

where ψ is the angle from $\boldsymbol{m}$ to the direction $(\sin\phi, -\cos\phi, 0)$ in the xy-plane, which is perpendicular to $\boldsymbol{n}$. Consider the following matrix representation for Q:

$$Q = \begin{pmatrix} q_0 & q_2 & q_3 \\ q_2 & q_1 & q_4 \\ q_3 & q_4 & -q_0 - q_1 \end{pmatrix} \tag{2.13}$$

Following the article by Mottram and Newton [53], using (2.11) and (2.12), write the components of Q in terms of θ, ϕ, and ψ:

$$\begin{aligned}
q_0 &= s\cos^2\theta\cos^2\phi + r(\sin\phi\cos\psi - cos\phi\sin\psi\sin\theta)^2 - \frac{1}{3}(s+r) \\
q_1 &= s\cos^2\theta\sin^2\phi + r(\cos\phi\cos\psi + \sin\phi\sin\psi\sin\theta)^2 - \frac{1}{3}(s+r) \\
q_2 &= s\cos^2\theta\sin\phi\cos\phi - r(\cos\phi\cos\psi + \sin\phi\sin\psi\sin\theta)(\sin\phi\cos\psi - \cos\phi\sin\psi\sin\theta) \\
q_3 &= s\sin\theta\cos\theta\cos\phi + r\sin\psi\cos\theta(\sin\phi\cos\psi - \cos\phi\sin\psi\sin\theta) \\
q_4 &= s\cos\theta\sin\theta\sin\phi - r\sin\psi\cos\theta(\cos\phi\cos\psi + \sin\phi\sin\psi\sin\theta)
\end{aligned}$$

Now, let the directors $\boldsymbol{n}$ and $\boldsymbol{m}$ lie along the x and y axes, the laboratory frame of reference. Then $\theta = 0$, $\phi = 0$, and $\psi = \pi$, and the above terms simplify to:

$$q_0 = \frac{1}{3}(2s - r),$$

$$q_1 = \frac{1}{3}(2r - s),$$
$$q_2 = q_3 = q_4 = 0.$$

The restriction to the uniaxial phase requires two eigenvalues to be equal, which happens in three possible cases:

$$q_0 = -q_0 - q_1 \implies q_0 = \frac{r}{3},$$
$$q_1 = -q_0 - q_1 \implies q_1 = \frac{s}{3},$$
$$q_0 = q_1 = \frac{s}{3} = \frac{r}{3}.$$

When one of these occurs, the uniaxial tensor Q is becomes:

$$Q = s_0(\boldsymbol{n} \otimes \boldsymbol{n} - \frac{1}{3}I) \tag{2.14}$$

where $s_0 \in (-1/3, 1)$. Note that in this case, $\boldsymbol{n}$ corresponds to the director previously described for the Oseen-Frank model.

A parameter of high interest in this work is the biaxiality parameter, β, which describes the degree of biaxiality throughout the domain of interest. It is defined as:

$$\beta(Q) = 1 - 6\frac{(\text{tr } Q^3)^2}{(\text{tr } Q^2)^3}. \tag{2.15}$$

By Lemma 1, in [55], $\beta(Q) \in [0, 1]$ and $\beta(Q) = 0$ if and only if Q is uniaxial. For highly concentrated biaxial defect regions, the bulk is unaxial with positive order parameter away from the defects, and therefore has a nice representation for the line field in terms of the dominant eigenvector [19]. This fact will exploited for visualization purposes in Chapters 4 and 5. In some domains the biaxial behavior is not concentrated, as in the case with concentric cylinders, and the line field will not be well-defined. In these cases, the biaxiality parameter will be the only constructive way to understand the liquid crystal behavior in the system.

2.9 The Landau-de Gennes Model

The most general continuum theory for nematic liquid crystals is the Landau-de Gennes theory which can account for uniaxial and biaxial phases. In the Landau-de Gennes framework, the state of a nematic liquid crystal is modeled by the symmetric, traceless three-by-three matrix Q as defined above. In this model, three energy contributions are considered: energy

due to elastic distortions, E_E, energy due to homogenous alignment, E_B, and energy due to liquid crystal alignment on domain surfaces, E_S. The total energy is:

$$\begin{aligned} E_{LDG} &= E_E(\nabla Q) + E_B(Q) + E_S(Q) \\ &= \int_\Omega (f_E(\nabla Q) + f_B(Q)) + \int_\Gamma (f_S(Q)). \end{aligned} \tag{2.16}$$

f_E is the elastic energy density that represents the contribution of the gradient of Q and therefore penalizes spatial variations in the tensor field. f_S is the surface free-energy density and penalizes disagreement between the tensor field and the prescribed boundary tensor Q_0. f_B is the volumetric free-energy density due to bulk contributions, and encodes the phase transition behavior of the material [56],[30]. Note that in (2.16), ∇Q is a third order tensor such that $(\nabla Q)_{ijk} = \partial Q_{ij}/\partial x_k$. Written out explicitly these terms become:

$$f_E(Q) = \frac{1}{2}L_1 Q_{\alpha\beta,\gamma} Q_{\alpha\beta,\gamma} + \frac{1}{2}L_2 Q_{\alpha\beta,\beta} Q_{\alpha\gamma,\gamma} + \frac{1}{2}L_3 Q_{\alpha\beta,\gamma} Q_{\alpha\gamma,\beta}, \tag{2.17}$$

$$f_B(Q) = \frac{A}{2}\text{tr }(Q^2) - \frac{B}{3}\text{tr }(Q^3) + \frac{C}{4}\text{tr }(Q^2)^2 + D(A,B,C), \tag{2.18}$$

$$f_S(Q) = \frac{W}{2}\left|Q\big|_\Gamma - Q_0\right|^2, \tag{2.19}$$

where $L_1, L_2, L_3 > 0$, Q is the symmetric, traceless, second order tensor described in Section 2.8 above, $Q\big|_\Gamma$ is Q restricted to a surface in the domain, and $D(A,B,B)$ is chosen so that $f_B(Q) \geq 0$. We let $D(A,B,C) = \min\ f_b(Q)$ where the minimum is taken over all symmetric, traceless Q, which is guaranteed to exist by Proposition 16 of [55]. Before studying the minimization of the entire Landau-de Gennes energy, we address the issue of orientability which is a relevant feature of the model.

2.10 Orientability

We now introduce an important issue concerning the relationship between the tensor Q and the director described by the vector field $\boldsymbol{n}$. From (2.10), it is clear that Q respects the head-to-tail symmetry of the liquid crystal molecules because of its invariance under the transformations $\boldsymbol{n} \to -\boldsymbol{n}$ and $\boldsymbol{m} \to -\boldsymbol{m}$. When Q is uniaxial as described by (2.14), this invariance indicates that a line field associated with the tensor Q, rather than the vector field $\boldsymbol{n}$, is the appropriate variable to describe molecular alignment. On the other hand, if there is a unit vector field, $\boldsymbol{n}$, that can be associated with a line field, Q, such that no discontinuities form, they will give equivalent molecular configurations. Defining such a continuous vector field from a line field is oftentimes not possible and this issue, referred to

as orientability, must be studied further. For the fixed non-zero constant $s \in [-1/2, 1]$, let

$$\mathcal{Q} := \{Q \in \mathcal{M}^{3\times 3} : Q = s(\boldsymbol{n} \otimes \boldsymbol{n} - (1/3)I) \text{ for some } \boldsymbol{n} \in \mathbb{S}^2\}$$

Also, define the projection operator $P : \mathbb{S}^2 \to \mathcal{Q}$ by:

$$P(\boldsymbol{n}) := s(\boldsymbol{n} \otimes \boldsymbol{n} - (1/3)I)$$

Ball and Zarnescu give a precise definition of the orientability of Q:

Definition 2.10.1. ([57], orientability): *Let Ω be a domain. We say that $Q \in W^{1,p}(\Omega, \mathcal{Q})$ is orientable if there exists an $\boldsymbol{n} \in W^{1,p}(\Omega, \mathbb{S}^2)$ such that $P(\boldsymbol{n}) = Q$ a.e. Otherwise we call Q non-orientably.*

Note that the energy expression (2.16) is finite for $Q \in H^1(\Omega)$. Additionally, Q must be uniaxial everywhere in the domain Ω and cannot contain any line defects in order for its associated line fields to be orientable. Ball and Zarnescu discuss orientability further in the following theorem:

Theorem 2.10.1. ([57]): *For simply connected domains, line fields belonging to $W^{1,p}$ for some $p \geq 2$ are orientable.*

Ball and Zarnescu explain that understanding the behavior on the boundary provides insight into the orientability of Q. To better illustrate this issue, consider simply connected domains out of which one cuts a finite number of 'holes,' which are also simply connected. As an example, consider Figure 2.5, which is based on an image from [57]. An orientable boundary condition is prescribed on the outer boundary and no boundary conditions are prescribed on the interior boundaries. These boundary conditions can be satisfied by both orientable and non-orientable line configurations, but the oriented boundary condition results in a higher energy since a gradient must develop.

We do not claim that the line field is the minimizer for the figure above, but instead, that it will have a lower energy than if we try to impose an orientation. This necessarily implies that the oriented configuration can have a higher energy than the non-oriented system. From this simple example, it is clear that for domains which are not simply connected, the Landau-de Gennes may allow for a configuration with less energy. If the domain under consideration is simply connected, there are simple assumptions under which the two models are exactly equal as we will show in the following section.

Figure 2.5: Orientability in a Stadium

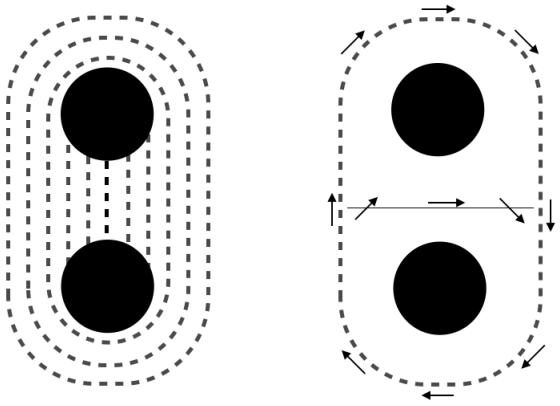

Assume that the distance between the two black circles is nonzero. On the left, a non-orientable line field is imposed. Along any line that intersects the stadium between the two circles, $|\nabla Q|$ will be zero in the non-oriented configuration. On the right, consider prescribing an orientation. Matching the oriented boundary conditions prescribed on the exterior boundary causes a gradient to develop along this line.

2.11 Landau-de Gennes in Terms of Oseen-Frank

If the line field describing the molecular orientation is orientable, there are conditions under which the one-constant approximations of the Oseen-Frank model and the Landau-de Gennes model are equivalent. These results are summarized into the following proposition:

Proposition 2.11.1. *Assume that Ω is a simply connected domain, s is constant, and $Q \in H^1(\Omega)$ is uniaxial. Then the first order approximation of the Oseen-Frank energy is equal to the first order approximation of the Landau-de Gennes energy with $K = Ls^2$.*

Proof. Consider the first order approximation of the Landau-de Gennes model:

$$E^*_{LDG}(Q) = \int_\Omega \frac{L}{2}|\nabla Q|^2 \, d\boldsymbol{x}. \tag{2.20}$$

Since Q assumed uniaxial, $|\nabla Q|^2$ can be expanded in the following way:

$$\begin{aligned}
|\nabla Q|^2 &= \frac{\partial Q_{ij}}{\partial x_k}\frac{\partial Q_{ij}}{\partial x_k} \\
&= \left[\nabla s_k(\boldsymbol{n}\otimes\boldsymbol{n} - \frac{1}{3}I)_{ij} + s(\nabla n_{jk} n_i + \nabla n_{ik} n_j)\right] \\
&\qquad \left[\nabla s_k(\boldsymbol{n}\otimes\boldsymbol{n} - \frac{1}{3}I)_{ij} + s(\nabla n_{jk} n_i + \nabla n_{ik} n_j)\right] \\
&= \nabla s_k \nabla s_k (\boldsymbol{n}\otimes\boldsymbol{n} - \frac{1}{3}I)_{ij}(\boldsymbol{n}\otimes\boldsymbol{n} - \frac{1}{3}I)_{ij}
\end{aligned}$$

$$+ 2s\nabla s_k(\boldsymbol{n}\otimes\boldsymbol{n} - \frac{1}{3}I)_{ij}(\nabla n_{jk}n_i + \nabla n_{ik}n_j)$$
$$+ s^2(\nabla n_{jk}n_i + \nabla n_{ik}n_j)(\nabla n_{jk}n_i + \nabla n_{ik}n_j).$$

This expression is simplified using the fact that $|\boldsymbol{n}|^2 = 1$. Let us consider each term separately:

$$\begin{aligned}\nabla s_k\nabla s_k(\boldsymbol{n}\otimes\boldsymbol{n} - \frac{1}{3}I)_{ij}(\boldsymbol{n}\otimes\boldsymbol{n} - \frac{1}{3}I)_{ij} &= \nabla s_k\nabla s_k(n_in_jn_in_j - \frac{2}{3}n_in_j\delta_{ij} + \frac{1}{9}I_{ij}I_{ij})\\ &= \nabla s_k\nabla s_k(n_in_jn_jn_i - \frac{2}{3}n_in_i + \frac{1}{3})\\ &= \nabla s_k\nabla s_k(1 - \frac{2}{3} + \frac{1}{3}) = \frac{2}{3}|\nabla s|^2\end{aligned} \tag{2.21}$$

$$\begin{aligned}2s\nabla s_k(\boldsymbol{n}\otimes\boldsymbol{n} - \frac{1}{3}I)_{ij}(\nabla n_{jk}n_i + \nabla n_{ik}n_j) &= 2s\nabla s_k(n_in_j\frac{\partial n_j}{\partial x_k}n_i + n_in_j\frac{\partial n_i}{\partial x_k}n_j\\ &\quad - \frac{1}{3}\delta_{ij}\frac{\partial n_j}{\partial x_k}n_i - \frac{1}{3}\delta_{ij}\frac{\partial n_i}{\partial x_k}n_j)\\ &= 2s\nabla s_k(n_j\frac{\partial n_j}{\partial x_k} + n_i\frac{\partial n_i}{\partial x_k} - \frac{2}{3}\frac{\partial n_i}{\partial x_k}n_i)\\ &= 2s\nabla s_k(\frac{4}{3}n_i\frac{\partial n_i}{\partial x_k}) = \frac{4}{3}s\nabla s_k\frac{\partial|\boldsymbol{n}|^2}{\partial x_k} = 0\end{aligned} \tag{2.22}$$

$$\begin{aligned}s^2(\nabla n_{jk}n_i + \nabla n_{ik}n_j)(\nabla n_{jk}n_i + \nabla n_{ik}n_j) &= s^2(\frac{\partial n_j}{\partial x_k}n_i\frac{\partial n_j}{\partial x_k}n_i + 2\frac{\partial n_j}{\partial x_k}n_i\frac{\partial n_i}{\partial n_k}n_j\\ &\quad + \frac{\partial n_i}{\partial x_k}n_j\frac{\partial n_i}{\partial x_k}n_j)\\ &= s^2(2\frac{\partial n_i}{\partial x_k}\frac{\partial n_i}{\partial x_k} + 2\left(\frac{\partial}{\partial x_k}\frac{|\boldsymbol{n}|^2}{2}\right)\left(\frac{\partial}{\partial x_k}\frac{|\boldsymbol{n}|^2}{2}\right))\\ &= 2s^2|\nabla\boldsymbol{n}|^2\end{aligned} \tag{2.23}$$

Adding (2.21), (2.23) and (2.23), (2.14) becomes:

$$\frac{L}{2}|\nabla Q|^2 = L(\frac{1}{3}|\nabla s|^2 + s^2|\nabla\boldsymbol{n}|^2) \tag{2.24}$$

Since s is constant and $K = s^2L$ by assumption, we have

$$E^*_{LDG}(Q) = \int_\Omega \frac{L}{2}|\nabla Q|^2\ d\boldsymbol{x} = \int_\Omega K|\nabla\boldsymbol{n}|^2\ d\boldsymbol{x} = E^*_{OF}(\boldsymbol{n})$$

Futhermore, since $Q \in H^1(\Omega)$, Q and $\boldsymbol{n}$ will describe the same molecular orientation as a result of Theorem 2.10.1. □

Note that (2.24) is known as the Ericksen's model for liquid crystal energy with variable degree of orientation, which was briefly mentioned in Section 2.3. This model is dependent on the order parameter s, and director $\boldsymbol{n}$ [2]. There is a slight change in convention where

the order parameter s is the negative of the s defined for the tensor Q. In other words, now $s \in (-1/2, 1)$, and $s = 0$ continues to correspond to the isotropic state. According to this model, point defects and disclinations will have finite energy. In fact, even if $\nabla \boldsymbol{n} \to \infty$ in the neighborhood of a defect, we can have $s \to 0$ in such a way that $s^2|\nabla \boldsymbol{n}|^2$ is bounded [58]. Existence, local uniqueness, and regularity of minimizers for this energy expression was proved by Lin in [28]. While this model, provides a more robust description since line defects no longer have infinity energy, it does not allow for biaxial regions which we are interested in computing.

Proposition 2.11.1 has a further extension to domains in which $Q \notin H^1(\Omega)$. For simply connected domains, Majumdar and Zarnescu in [55] show that the predictions in Oseen-Frank theory agree with Landau-de Gennes theory away from singularites. While these results are important, we will be considering domains which are not simply connected and therefore the issue of orientability will allow for more minimizers in the Q tensor description than the vector field description, which further motivates our use of the Landau-de Gennes energy expression. Although our numerical studies will concern the Landau-de Gennes model, the comparison of that model with Oseen-Frank brings out subtle aspects of liquid crystal behavior, some found for the first time. We next establish an existence result in the following section before presenting our numerical work.

2.12 Existence of a Minimizer for Landau-de Gennes

We use the direct methods of calculus of variations to show existence and follow similar arguments as outlined in Chapter 8 of [59]. Let us recall that the total energy is given by

$$E(Q) = \int_\Omega (f_E(\nabla Q) + f_B(Q)) + \int_\Gamma (f_S(Q)), \tag{2.25}$$

where f_E, f_B, and f_S are defined in (2.17), (2.18), and (2.19) respectively, Ω is the liquid crystal domain, and $\Gamma \subseteq \partial\Omega$ is the surface on which weak anchoring is enforced. We begin with the following definition:

Definition 2.12.1. *We say that $I[\cdot]$ is (sequentially) weakly lower semicontinuous on $W^{1,q}(\Omega)$, provided*

$$I[Q] \leq \liminf_{k\to\infty} I[Q_k]$$

whenever

$$Q_k \rightharpoonup Q \text{ weakly in } W^{1,q}(\Omega).$$

In the main Theorem of this Section, we will not prove weak lower semi-continuity directly, but instead use the following result.

Theorem 2.12.1. ([59], Weak lower semicontinuity): *Assume that L is smooth, bounded below, and in addition*

$$\text{the mapping } \mathcal{B} \mapsto L(\mathcal{B}, P, \boldsymbol{x}) \text{ is convex,}$$

for each $P \in \mathbb{M}^{3\times 3}$, $\boldsymbol{z} \in \mathbb{R}^m$. Then

$$I[\cdot] \text{ is weakly lower semicontinuous on } W^{1,q}(\Omega)$$

We now establish existence for a general functional dependent on a symmetric, traceless tensor Q.

Theorem 2.12.2. (Existence for tensor dependence): *Let $I[Q] = \int_\Omega L(\nabla Q(\boldsymbol{x}), Q(\boldsymbol{x}), \boldsymbol{x})\, d\boldsymbol{x}$ and assume that L satisfies the coercivity inequality:*

$$L(\mathcal{B}, P, \boldsymbol{x}) \geq \alpha|\mathcal{B}|^2 - \beta, \ (\mathcal{B} \in \mathbb{M}^{3\times 3\times 3}, \ P \in \mathbb{M}^{3\times 3}, \ \boldsymbol{x} \in \mathbb{R}^m) \tag{2.26}$$

for constants $\alpha > 0$, $\beta \geq 0$. Also, suppose L is convex in the variable $\mathcal{B}$ and the admissible set,

$$\mathcal{A} = \{Q \in H^1(\Omega; \mathbb{R}^m) | \text{tr } Q = 0 \text{ and } Q = Q_0 \text{ on } \partial U/\Gamma \text{ in the trace sense}\}, \tag{2.27}$$

where $Q_0 : \partial U/\Gamma \to \mathbb{R}$ given, is nonempty. Then there exists at least one function $R \in \mathcal{A}$ such that $I[R] = \min_{Q\in\mathcal{A}} I[Q]$.

Proof. Begin by setting $m = \inf_{R\in\mathcal{A}} I[R]$ and assume that m is finite. Choose a minimizing sequence Q^k so that $I[Q^k] \to m$ as $k \to \infty$. For simplification, take $\beta = 0$ in (2.26), since one can always consider $\tilde{L} = L + \beta$ and the same arguments would apply. This inequality then implies

$$I[Q] \geq \alpha \int_\Omega |\nabla Q|^2 \, d\boldsymbol{x}. \tag{2.28}$$

Since m finite,

$$\sup_k ||\nabla Q^k||_{L^2(\Omega)} < \infty \tag{2.29}$$

Consider any function $R \in \mathcal{A}$. Since Q^k and R both equal Q_0 on $\partial\Omega/\Gamma$ in the trace sense, $Q^k - R \in H_0^1(\Omega)$. Poincare's inequality and (2.29) then imply

$$||Q^k||_{L^2(\Omega)} \leq ||Q^k - R||_{L^2(\Omega)} + ||R||_{L^2(\Omega)} \leq C||\nabla Q^k - \nabla R||_{L^2(\Omega)} + C \leq C \tag{2.30}$$

and so $\sup ||Q^k||_{L^2(\Omega)} < \infty$. Together with (2.29), this implies $Q^k \in H^1(\Omega)$. Therefore, there exists a subsequence $\{Q^{k_j}\}_{j=1}^{\infty} \subset \{Q^k\}$ and a $Q^* \in H^1(\Omega)$ such that

$$Q^{k_j} \rightharpoonup Q^* \text{ weakly in } H^1(\Omega) \tag{2.31}$$

Q^* is a candidate for our minimizer, but we must verify that $Q^* \in \mathcal{A}$. By the Rellich-Kondrachov Theorem, $H^1(\Omega) \subset\subset L^2(\Omega)$. Since Q^{k_j} is a uniformly bounded sequence in $H^1(\Omega)$, it will converge strongly in $L^2(\Omega)$ which further implies $Q^{k_j}(\boldsymbol{x}) \to Q^*(\boldsymbol{x})$ for a.e. $\boldsymbol{x} \in \Omega$. Since the matrix trace is continuous, tr $Q^{k_j} \to$ tr Q^* and tr $Q^* = 0$. Strong convergence in L^2 further implies that

$$Q_0 = Q^{k_j}\Big|_{\Gamma} \to Q^*\Big|_{\Gamma} = Q_0 \tag{2.32}$$

giving us that $Q^* \in \mathcal{A}$. By Theorem 2.12.1

$$I[Q] \leq \liminf_{j\to\infty} I[Q^{k_j}] = m \tag{2.33}$$

but since $Q \in \mathcal{A}$, it follows that

$$I[Q] = m = \min_{R\in\mathcal{A}} I[R]$$

□

When proving the existence of a minimizer for the Landau-de Gennes energy the Extension Theorem is used to show that the admissible set is nonempty and we include it below for completeness.

Theorem 2.12.3. ([59], Extension): *Assume Ω is bounded and $\partial\Omega$ is C^1. Select a bounded open set V such that $\Omega \subset\subset V$. Then there exists a bounded linear operator $E : W^{1,p}(\Omega) \to W^{1,p}(\mathbb{R}^n)$ such that for each $Q \in W^{1,p}(\Omega)$:*

(1) $EQ = Q$ a.e.

(2) EQ has support within V

(3) $||EQ||_{W^{1,p}(\mathbb{R}^n)} \leq C||Q||_{W^{1,p}(\Omega)}$ where C depends only on p, Ω and V

We can now use Theorem 2.12.2 to show the existence of a minimizer for the Landau-de Gennes energy model.

Theorem 2.12.4. (Existence of a Minimizer for Landau-de Gennes): *Assume that $L_i \geq 0$, $i = 1, 2, 3$ and $\frac{1}{2}L_1 - 2L_2 - 2L_3 > 0$. Then there exists a $\bar{Q}$ such that*

$$E(\bar{Q}) = \inf_{Q\in\mathcal{A}} E(Q) \tag{2.34}$$

where E and $\mathcal{A}$ are given by (2.25) and (2.27) respectively.

Proof. Using Theorem 2.12.3, extend $Q_0 \in H^1(\Omega)$, which is prescribed on Γ, to all of $\mathbb{R}^n$. Then the restriction to Ω is in the admissible set. Notice that $f_B(Q)$ and $f_S(Q)$ do not depend on the derivatives of Q, and so we only need to show that $f_E(\nabla Q)$ is convex. This is straightforward using the linearity of the derivative:

$$\begin{aligned}
f_E(\lambda\partial Q + (1-\lambda)\partial P) &= f_E(\partial(\lambda Q + (1-\lambda)P)) \\
&= \frac{1}{2}L_1(\lambda Q + (1-\lambda)P)_{\alpha\beta,\gamma}(\lambda Q + (1-\lambda)P)_{\alpha\beta,\gamma} + \\
&\quad + \frac{1}{2}L_2(\lambda Q + (1-\lambda)P)_{\alpha\beta,\beta}(\lambda Q + (1-\lambda)P)_{\alpha\gamma,\gamma} + \\
&\quad + \frac{1}{2}L_3(\lambda Q + (1-\lambda)P)_{\alpha\beta,\gamma}(\lambda Q + (1-\lambda)P)_{\alpha\gamma,\beta} \\
&= \lambda(\frac{1}{2}L_1 Q_{\alpha\beta,\gamma}Q_{\alpha\beta,\gamma} + \frac{1}{2}L_2 Q_{\alpha\beta,\beta}Q_{\alpha\gamma,\gamma} + \frac{1}{2}L_3 Q_{\alpha\beta,\gamma}Q_{\alpha\gamma,\beta}) \\
&\quad + (1-\lambda)(\frac{1}{2}L_1 P_{\alpha\beta,\gamma}P_{\alpha\beta,\gamma} + \frac{1}{2}L_2 P_{\alpha\beta,\beta}P_{\alpha\gamma,\gamma} + \frac{1}{2}L_3 P_{\alpha\beta,\gamma}P_{\alpha\gamma,\beta}) \\
&= \lambda f_E(\partial Q) + (1-\lambda) f_E(\partial P)
\end{aligned}$$

Next, we show that f_E is coercive. Notice that the first term of f_E can be written as $\frac{1}{2}L_1 Q_{\alpha\beta,\gamma}Q_{\alpha\beta,\gamma} = \frac{1}{2}L_1|\nabla Q|^2$. Using this, and the triangle inequality, we can show that the entire term is bounded below by a constant times $|\nabla Q|^2$

$$\begin{aligned}
f_E(\partial Q) &= \frac{1}{2}L_1 Q_{\alpha\beta,\gamma}Q_{\alpha\beta,\gamma} + \frac{1}{2}L_2 Q_{\alpha\beta,\beta}Q_{\alpha\gamma,\gamma} + \frac{1}{2}L_3 Q_{\alpha\beta,\gamma}Q_{\alpha\gamma,\beta} \\
&\geq \frac{1}{2}L_1|\nabla Q|^2 + L_2(-Q_{\alpha\beta,\beta}Q_{\alpha\beta,\beta} - Q_{\alpha\gamma,\gamma}Q_{\alpha\gamma,\gamma}) + \\
&\qquad + L_3(-Q_{\alpha\beta,\gamma}Q_{\alpha\beta,\gamma} - Q_{\alpha\gamma,\beta}Q_{\alpha\gamma,\beta}) \\
&= \frac{1}{2}L_1|\nabla Q|^2 - L_2(2|\nabla Q|^2) - L_3(2|\nabla Q|^2) \\
&= (\frac{1}{2}L_1 - 2L_2 - 2L_3)|\nabla Q|^2
\end{aligned}$$

By definition, $f_S(Q) \geq 0$. Also, recall $f_B(Q) \geq 0$ by the choice of $D(A,B,C) > 0$ as the minimum of $f_B(Q)$ which is guaranteed to exist by [55]. The assumptions on L_1, L_2, L_3 then ensure coercivity and Theorem 2.12.2 guarantees that the minimizer exists for (2.25). □

2.13 Non-Dimensionalization of the Landau-de Gennes Model

In the chapters that follow, the focus will be on numerical computing with the Landau-de Gennes energy integral. The one-constant approximation of the elastic energy, where $L_1 = L$ and $L_2 = 0 = L_3$, will be used. Additionally, the bulk terms without the constant

$D(A,B,C)$ will be considered, and the use of Dirchlet boundary conditions results in the elimination of the surface integral. The energy now has the following form:

$$\int_\Omega L|\nabla Q|^2 + f(Q)\ d\boldsymbol{x} \tag{2.35}$$

where $f(Q) = f_B(Q) - D(A,B,C)$, with $f_B(Q)$ is defined as in (2.18), and Q is the symmetric, traceless, second-order tensor described in Section 2.8.

We will now use parameter values for the compound 5CB, a standard liquid crystal. The bulk and elastic constants are given by $A = -.172 \times 10^6 N/m^2, B = -2.12 \times 10^6 N/m^2, C = 1.73 \times 10^6 N/m^2$, and $L = 4 \times 10^{-11} N$ [60]. Since the bulk constants are approximatedly 10^{17} times larger than the elastic constants in these units, this suggests that we may have a very singularly perturbed problem. To study this further, the energy expression is non-dimensionalized. Let

$$\hat{\boldsymbol{x}} = \boldsymbol{x}/L_0 \text{ and } \hat{\Omega} = (\Omega/L_0), \tag{2.36}$$

where $\hat{\Omega}$ is the non-dimensionalized domain and L_0 is a characteristic length scale. The one-constant approximation for the elastic energy can be rewritten in the following way:

$$E(Q) = \int_\Omega \frac{L}{2}|\nabla Q|^2 + f(Q)\ d\boldsymbol{x} = \int_{\hat{\Omega} L_0} \left[\frac{L}{2L_0^2}|\hat{\nabla}\hat{Q}|^2 + |A|\hat{f}(\hat{Q})\right]\ L_0^3\ d\hat{\boldsymbol{x}},$$

where $Q(\boldsymbol{x}) = \hat{Q}(\hat{\boldsymbol{x}})$ and $\hat{f}(\hat{Q}) = (1/|A|)f(Q)$. Let us define the dimensionless energy to be $\hat{E}(\hat{Q}) = (1/LL_0)E(Q)$:

$$\begin{aligned}\hat{E}(\hat{Q}) &= \int_{\hat{\Omega}} \frac{1}{2}|\hat{\nabla}\hat{Q}|^2 + \frac{|A|L_0^2}{L}\left[\frac{-1}{2}\text{tr}\ \hat{Q}^2 + \frac{1}{3}\frac{B}{|A|}\text{tr}\ Q^3 + \frac{1}{4}\frac{C}{|A|}(\text{tr}\ \hat{Q}^2)^2\right]\ d\hat{\boldsymbol{x}} \\ &= \int_{\hat{\Omega}} \frac{1}{2}|\hat{\nabla}\hat{Q}|^2 + \mathcal{A}\left[\frac{-1}{2}\text{tr}\ \hat{Q}^2 + \frac{1}{3}\mathcal{B}\text{tr}\ \hat{Q}^3 + \frac{1}{4}\mathcal{C}(\text{tr}\ \hat{Q}^2)^2\right]\ d\hat{\boldsymbol{x}}\end{aligned} \tag{2.37}$$

where

$$\mathcal{C} = C/|A|, \mathcal{B} = B/|A|, \text{ and } \mathcal{A} = (|A|L_0^2)/L. \tag{2.38}$$

$\mathcal{C}$ and $\mathcal{B}$ are constants depending on the material parameters of the liquid crystal. L_0 is chosen to be the *coherence length* scale so that $\mathcal{A} = 1$, i.e.,

$$L_0 = \sqrt{L/|A|} \approx 1.52 \times 10^{-8}\text{m}$$

Notice that bulk and elastic constants are now of the same order of magnitude and, when an appropriate domain is chosen, the problem is not singularly perturbed. For the remainder of this thesis, the dimensionless energy will be used, but the hat will be dropped for simplicity:

$$E(Q) = \int_\Omega \frac{1}{2}|\nabla Q|^2 - \frac{1}{2}\text{tr}\ Q^2 + \frac{\mathcal{B}}{3}\text{tr}\ Q^3 + \frac{\mathcal{C}}{4}(\text{tr}\ Q^2)^2\ d\boldsymbol{x} \tag{2.39}$$

In the Chapters that follow, we use this energy expression to examine computational and theoretical liquid crystal configurations for a variety of domains. In some cases, we reproduce previous numerical results and compare the minimizing configurations to theoretical and experimental evidence. In other domains, the energy minimizing configurations produced were not previously predicted in the literature, but better align with liquid crystal behavior seen in experiments.

Chapter 3

Numerical Simulations in Two Dimensions

In this Chapter, we consider two-dimensional domains and a reduced two-dimensional version of the Landau-de Gennes energy. While these assumptions are not physically meaningful, they help us understand the behavior of the liquid crystal in three dimensions and allow us to compare with previous numerical results in such geometries. The restriction to a two-dimensional energy expression will necessarily enforce that Q be uniaxial everywhere and lie in the plane. This fact will be exploited for visualization purposes since the line field will be well-defined everywhere. This also allows for interesting comparision with previous numerical works done using Oseen-Frank.

A variety of domains and boundary conditions will be considered and energy minimizing configurations will be found using FEniCS, a computing platform which uses finite elements to solve PDEs. For some of the domains, our computations will be in agreement with previous theoretical and numerical work, as in the case of domains with particles embedded. On the other hand, for the annulus, the inability of the director to relax out of the plane suppresses some of the observed behavior [7]. For the droplet, we find that the split core defect seen in previous numerical studies may actually be an artifact of improper mesh refinement. All of these issues will be discussed in further detail in the sections that follow.

3.1 The Weak Energy Expression

In order to compute the minimizing configurations using FEniCS, the Landau-de Gennes energy must be expressed in weak form. Since we are considering a restriction to two

dimensions, our symmetric, traceless tensor Q has the following form:

$$Q = \begin{bmatrix} q_0 & q_1 \\ q_1 & -q_0 \end{bmatrix}. \tag{3.1}$$

The energy expression used for the numerical computing will be the non-dimensionalized version of Landau-de Gennes defined in Chapter 2. For Q as defined in (3.1), tr $Q^3 = 0$ and the dimensionless energy expression becomes:

$$E(Q) = \int_\Omega \frac{1}{2}|\nabla Q|^2 - \frac{1}{2}\text{tr } Q^2 + \frac{\mathcal{C}}{4}(\text{tr } Q^2)^2 \; d\boldsymbol{x} \tag{3.2}$$

In order to compute the minimizer of this integral, the elastic and bulk terms of the energy are expressed in terms of the components of Q:

$$E(q_0, q_1) = \int_\Omega (\frac{\partial q_0}{\partial x_0})^2 + (\frac{\partial q_0}{\partial x_1})^2 + (\frac{\partial q_1}{\partial x_0})^2 + (\frac{\partial q_1}{\partial x_1})^2 - (q_0^2 + q_1^2) + \mathcal{C}(q_0^2 + q_1^2)^2 \; d\boldsymbol{x}$$

Let $\boldsymbol{q} = (q_0, q_1)$ and $\boldsymbol{q} \in \tilde{W}^{1,2}(\Omega) = \{\boldsymbol{p} \in H^1(\Omega) |\ \boldsymbol{p} = \boldsymbol{g} \text{ on } \partial\Omega\}$, where $\boldsymbol{g} \in W^{1/2,2}(\Omega)$ is prescribed on the boundary of Ω, $\partial\Omega$. We now set the problem in variational formulation and calculate the weak Euler-Lagrange equations. For the test function $\boldsymbol{\nu} = (\nu_0, \nu_1) \in W_0^{1,2}(\Omega) = \{\boldsymbol{p} \in H^1(\Omega) |\ \boldsymbol{p} = \boldsymbol{0} \text{ on } \partial\Omega\}$ the first variation is calculated,

$$\begin{aligned}
\frac{d}{de}E(q_0 + ev_0, q_1)\Big|_{e=0} &= \frac{d}{de}\int_\Omega \left[(\frac{\partial q_0}{\partial x_0} + e\frac{\partial v_0}{\partial x_0})^2 + (\frac{\partial q_0}{\partial x_1} + e\frac{\partial v_0}{\partial x_1})^2 + (\frac{\partial q_1}{\partial x_0})^2 + (\frac{\partial q_1}{\partial x_1})^2\right] \\
&\qquad - \left[(q_0 + ev_0)^2 + q_1^2\right] + \mathcal{C}\left[(q_0 + ev_0)^2 + q_1^2\right]^2 \; d\boldsymbol{x}\Big|_{e=0} \\
&= \int_\Omega 2\frac{\partial q_0}{\partial x_0}\frac{\partial v_0}{\partial x_0} + \frac{\partial q_0}{\partial x_1}\frac{\partial v_0}{\partial x_1} - 2q_0v_0 + 4\mathcal{C}(q_0^2 + q_1^2)q_0v_0 \; d\boldsymbol{x} \\
&= \int_\Omega 2\nabla q_0 \cdot \nabla v_0 + (-2q_0 + 4\mathcal{C}(q_0^2 + q_1^2)q_0)v_0 \; d\boldsymbol{x} = 0,
\end{aligned}$$

and

$$\frac{d}{de}E(q_0, q_1 + ev_1)\Big|_{e=0} = \int_\Omega 2L\nabla q_1 \cdot \nabla v_1 + (-2q_1 + 4\mathcal{C}(q_0^2 + q_1^2)q_1)v_1 \; d\boldsymbol{x} = 0.$$

Both expressions can be combined into

$$\int_\Omega 2L\nabla \boldsymbol{q} : \nabla \boldsymbol{v} + (-2 + 4\mathcal{C}(q_0^2 + q_1^2))\boldsymbol{q} \cdot \boldsymbol{v} \; d\boldsymbol{x} = \boldsymbol{0}, \tag{3.3}$$

where $A : B$ denotes the Frobenius inner product. Note that the above integral expression is the weak form of a semi-linear elliptic equation.

3.2 Visualization of the Solution

A finite element method based on piecewise polynomials over triangles, is used to solve (3.3). First, a mesh which consists of a finite number of disjoint triangles is generated using *mshr*, the mesh generation component of FEniCS. If the domain contains curved surfaces, they are approximated using polygons. After each mesh refinement, I ensure that the vertices which lie on the polygonal boundary are snapped out to the circular boundary which is being approximated. This results in the approximating polygon having an increased number of sides with each iteration. This process will be referred to as *snapping the boundary* and is done because it reduces the introduction of error due to boundary approximation. The approximate solution, $\boldsymbol{q}_h = (q_{0,h}, q_{1,h})$, is then computed over this mesh by calling 'NonlinearVariationalSolve,' a class which implements a solver for nonlinear problems using Newton's method.

In order to visualize the computed minimizer, I calculate the line field and the uniaxial order parameter s. Using relation (3.1), Q_h is defined in terms of $(q_{0,h}, q_{1,h})$. Since Q_h is uniaxial and restricted to two dimensions, $Q_h = s_h(\boldsymbol{n}_h \otimes \boldsymbol{n}_h - (1/2)I)$. In Section 2.8, we showed that $\boldsymbol{n}_h$ is the eigenvector associated to λ_h and $s_h = 2\lambda_h$, where λ_h is the dominant eigenvalue of Q_h. Once s_h and $\boldsymbol{n}_h$ are calculated over the mesh, I exported the data to a *pvd* file and processed it in Paraview, an application for interactive, scientific visualization. This program allows us to plot the line field and s_h over the domain. The figures in this thesis which show the domain, mesh, line field, and s_h have been generated in Paraview.

3.3 Specifying Boundary Conditions

Through the use of a surfactant, liquid crystal molecules can be forced to attach on domain boundaries in a rigid way. This inflexible attachment is referred to as strong anchoring and will be enforced with the use of a Dirichlet boundary condition. These boundary conditions must be described in terms of the components of Q, with $s = 1$. For radial alignment, the associated vector field is $\boldsymbol{n}_r = \boldsymbol{x}/|\boldsymbol{x}|$. The boundary conditions are described in terms of the components of Q using relation (3.1):

$$Q = \begin{vmatrix} (x_0^2)/|\boldsymbol{x}|^2 - 1/2 & (x_0x_1)/|\boldsymbol{x}|^2 \\ (x_0x_1)/|\boldsymbol{x}|^2 & (x_1^2)/|\boldsymbol{x}|^2 - 1/2 \end{vmatrix} = \begin{vmatrix} q_0 & q_1 \\ q_1 & -q_0 \end{vmatrix}.$$

This implies

$$q_0 = x_0^2/|\boldsymbol{x}|^2 - 1/2, q_1 = (x_0x_1)/|\boldsymbol{x}|^2. \tag{3.4}$$

Everywhere vertical Dirichlet boundary conditions are also prescribed in simulations. In this case, $\boldsymbol{n}_v = (0, 1)$ which implies

$$q_0 = -s/2, q_1 = 0. \tag{3.5}$$

These describe the only two boundary conditions used in the simulations presented in this Chapter.

3.4 Manufactured Solution for an Annulus

The method of manufactured solutions provides a procedure for generating solutions for code accuracy verification. The idea is to include in the code a source term and use it to generate a nontrivial but known solution structure, without being concerned with whether it is physically realistic [61]. For this solution, we choose a minimizing configuration predicted by the Oseen-Frank model for an annular region. This solution is then used to define the Dirchlet boundary conditions and plugged into the strong form of the Euler-Lagrange equations to calculate the source term used in the minimization.

Consider the domain composed of an annulus with the liquid crystal 5CB filling the region between the two bounding circles. We prescribe normal Dirichlet boundary conditions on both boundaries using relation (3.4). For the manufactured solution, a configuration which is a reasonable energy minimizer for this domain is chosen. Bethuel, Brezis, Coleman, and Hélein use the Oseen-Frank energy expression to prove that for a liquid crystal domain bounded by two concentric circles, the unique energy minimizer will be radial for $\rho \geq e^{-\pi} \approx .0432$, where ρ is the ratio of the inner to the outer radius [20]. Bearing this in mind, the outer radius is chosen to be L_0 and the inner radius is chosen to be $.5L_0$, for L_0 being the characteristic length defined in Section 2.13. The annular domain satisfies the condition $\rho > e^{-\pi}$. Note that, we do not claim that the Oseen-Frank energy expression will have the same minimizer as the Landau-de Gennes energy, but instead that the radial solution is a reasonable choice when producing a manufactured solution. We begin by calculating the forcing term, $\boldsymbol{f}$, according to:

$$-2\Delta \boldsymbol{q} + [-2 + 4\mathcal{C}(q_0^2 + q_1^2)]\boldsymbol{q} = \boldsymbol{f} \tag{3.6}$$

where the left-hand side of is the strong form of the left-hand side of (3.3). The manufactured solution is given by $\boldsymbol{q}_m = (x_0^2/(x_0^2 + x_1^2) - 1/2, (x_0 x_1)/(x_0^2 + x_1^2))$ where $\boldsymbol{n}_r = (x_0/\sqrt{x_0^2 + x_1^2}, x_1/\sqrt{x_0^2 + x_1^2})$ corresponds to the radial line field. Inputting this into the

left-hand side of (3.4) allows us to calculate $\boldsymbol{f}$:

$$\begin{aligned} f_0 &= -2\Delta q_0 + (-2 + 4\mathcal{C}(q_0^2 + q_0^2))q_0 \\ &= \frac{4(x_0^2 - x_1^2)}{(x_0^2 + x_1^2)^2} + \left(-2 + 4\mathcal{C}\left[\left(\frac{x_0^2}{|\boldsymbol{x}|^2} - \frac{1}{2}\right)^2 + \left(\frac{x_0 x_1}{|\boldsymbol{x}|^2}\right)^2\right]\right)\left(\frac{x_0^2}{|\boldsymbol{x}|^2} - \frac{1}{2}\right) \\ f_1 &= -2\Delta q_1 + (-2 + 4\mathcal{C}(q_0^2 + q_0^2))q_1 \\ &= \frac{8x_0 x_1}{(x_0^2 + x_1^2)^2} + \left(-2 + 4\mathcal{C}\left[\left(\frac{x_0^2}{|\boldsymbol{x}|^2} - \frac{1}{2}\right)^2 + \left(\frac{x_0 x_1}{|\boldsymbol{x}|^2}\right)^2\right]\right)\left(\frac{x_0 x_1}{|\boldsymbol{x}|^2}\right) \end{aligned}$$

We find the approximate solution, $\boldsymbol{q}_h$, of (3.4) using FEniCS on the initial mesh pictured in Figure 3.1. This mesh is refined several times and the approximate solution, $\boldsymbol{q}_h$, is calculated in every iteration. The maximum, minimum and average cell diameter, h, for the initial and final meshes are calculated and organized into Table 3.1.

Table 3.1: Mesh Details for Annulus with $\rho = .5$

Mesh	Max h	Min h	Average h	Number of Triangles
Initial Mesh	$2.33e-01$	$1.13e-01$	$1.78e-01$	$2.18e+02$
Final Mesh	$2.66e-03$	$8.80e-04$	$1.64e-03$	$3.57e+06$

Figure 3.1: Initial Mesh for Annular Domain with $\rho = .5$

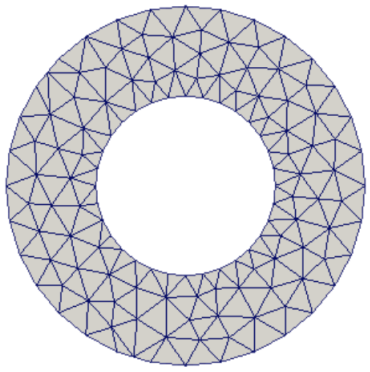

The initial mesh for the annular region with $\rho = .5$ on which the Landau-de Gennes energy will be minimized is shown.

We interpolate the manufactured solution, $\boldsymbol{q}_m$, onto each mesh and the error between this and $\boldsymbol{q}_h$ is found, where $\boldsymbol{q}_h$ is calculated using degree one and two Lagrange elements.

The largest cell diameter for each mesh is used to calculate the orders of convergence. The results are summarized into Tables 3.2 and 3.3.

Table 3.2: Convergence with Degree 1 Elements on Annular Domain with $\rho = .5$

Max h	Max Error	Max Order	L^2 Error	L^2 Order	H^1 Error	H^1 Order
$2.33e-01$	$9.85e-03$		$3.92e-03$		$4.07e-02$	
$1.71e-01$	$5.28e-03$	2.00	$2.13e-03$	1.96	$8.19e-02$	-2.25
$8.53e-02$	$1.56e-03$	1.76	$5.54e-04$	1.94	$4.39e-02$	0.90
$4.26e-02$	$4.39e-04$	1.82	$1.40e-04$	1.99	$2.27e-02$	0.95
$2.13e-02$	$1.22e-04$	1.85	$3.50e-05$	2.00	$1.16e-02$	0.97
$1.07e-02$	$3.36e-05$	1.86	$8.77e-06$	2.00	$5.83e-03$	0.99
$5.33e-03$	$9.19e-06$	1.87	$2.20e-06$	2.00	$2.93e-03$	0.99
$2.66e-03$	$2.49e-06$	1.88	$5.49e-07$	2.00	$1.47e-03$	1.00

Table 3.3: Convergence with Degree 2 Elements on Annular Domain with $\rho = .5$

Max h	Max Error	Max Order	L^2 Error	L^2 Order	H^1 Error	H^1 Order
$2.33e-01$	$5.92e-04$		$1.44e-04$		$4.40e-03$	
$1.71e-01$	$1.79e-04$	3.85	$6.12e-05$	2.75	$4.88e-03$	-0.34
$8.53e-02$	$2.65e-05$	2.75	$8.19e-06$	2.90	$1.22e-03$	2.00
$4.26e-02$	$3.84e-06$	2.79	$1.05e-06$	2.96	$3.00e-04$	2.02
$2.13e-02$	$5.24e-07$	2.87	$1.34e-07$	2.98	$7.41e-05$	2.02
$1.07e-02$	$6.88e-08$	2.93	$1.68e-08$	2.99	$1.84e-05$	2.01
$5.33e-03$	$8.84e-09$	2.96	$2.11e-09$	2.99	$4.58e-06$	2.01

Using degree one elements the maximum and L^2 rates are converging to two and the H^1 order is approaching one, giving the optimal rates predicted by the theory. Using degree two elements, we also see solid convergence results since the orders of the maximum norm and the L^2 norm are approaching three, while the order of the H^1 norm is approaching a value of two. This reassures us that the subsequent computations do not contain errors.

3.5 Various Annular Domains

In the following chapters, we focus on the minimizing configurations of concentric cylinder domains with planar radial Dirichlet boundary conditions on the lateral boundaries. One of the most influential papers concerning minimizers in this domain, by Bethuel et al. was

briefly mentioned in the previous section [20]. They use the one-constant approximation of the Oseen-Frank energy to prove that a liquid crystal confined between concentric cylinders have two possible energy minimizing configurations which depend on the parameter ρ, the ratio of the inner cylinder radius to the outer cylinder radius. For completeness, their results are summarized here. Their first theorem states that minimizers of the three-dimensional system will also be minimizers over the two-dimensional cross sections. Let Ω be a smooth bounded domain in $\mathbb{R}^2$, $D = \Omega \times [0,1]$, and ϕ be a smooth map from $\partial\Omega$ to S^2. Define

$$\mathcal{F} = \{u \in H^1(D, S^2); u(x,y,z) = \phi(x,y) \ for \ (x,y,z) \in \partial\Omega \times [0,1]\} \tag{3.7}$$

and

$$\mathcal{E} = \{u \in H^1(D, S^2); u(x,y) = \phi(x,y) \ for \ (x,y,z) \in \partial\Omega\}. \tag{3.8}$$

Theorem 3.5.1. ([20], Theorem 0): *If u is a minimizer for*

$$\min_{u\in\mathcal{F}} \int_D |\nabla u|^2 \ dx \ dy \ dz, \tag{3.9}$$

then u is independent of z and is a minimizer for

$$\min_{u\in\mathcal{E}} \int_D |\nabla u|^2 \ dx \ dy = \min_{u\in\mathcal{E}} \ E^*_{OF}. \tag{3.10}$$

Now, let $\Omega = B_1/B_\rho$, and let

$$\mathcal{E} = \left\{u \in H^1(\Omega, S^2); u_0(x,y) = \left(\frac{x}{r}, \frac{y}{r}, 0\right) \ on \ \partial\Omega\right\} \tag{3.11}$$

where $r = \sqrt{x^2+y^2}$. Let $\mathcal{E}_0$ be the set of functions in $\mathcal{E}$ which are radially symmetric, i.e. of the form

$$u(x,y) = c(r)u_0(x,y) + t(r)(0,0,1) \tag{3.12}$$

with $c^2 + t^2 = 1$. Notice this set contains the *escape solutions* characterized by t nonzero away from the boundaries. Which of these solutions is the minimizing configuration is addressed by the following theorem

Theorem 3.5.2. ([20], Theorem 1): *(1) If $\rho \geq e^{-\pi}$, then u_0 is a minimizer of E^*_{OF} on $\mathcal{E}$; if $\rho > e^{-\pi}$, u_0 is the unique minimizer in $\mathcal{E}$ (2) If $\rho < e^{-\pi}$, then u_0 is not a minimizer of E^*_{OF} on $\mathcal{E}$, but there is a minimizer on $\mathcal{E}$ that belongs to $\mathcal{E}_0$ and has $t(r) > 0$ for every $r \in (\rho, 1)$; this minimzer is unique in $\mathcal{E}_0$ to within replacement of $t(r)$ by $-t(r)$.*

Let us consider a wide range of ratios, $\rho = .8, .5, .3, .2, .15, .1, .05, .02, 0$. In each case, the initial mesh is generated using mshr, the mesh generation component of FEniCS, and the

approximating boundary is snapped to the circles they are approximating. For every ρ, the mesh is refined five times and the number of cells in the final mesh will be approximately 1.5 million in every case. As a illustrative example, consider $\rho = .15$. The initial mesh is shown in Figure 3.2 and the mesh details for the initial and final meshes are organized into the Table 3.4.

Figure 3.2: Initial Mesh for Annulus with $\rho = .15$

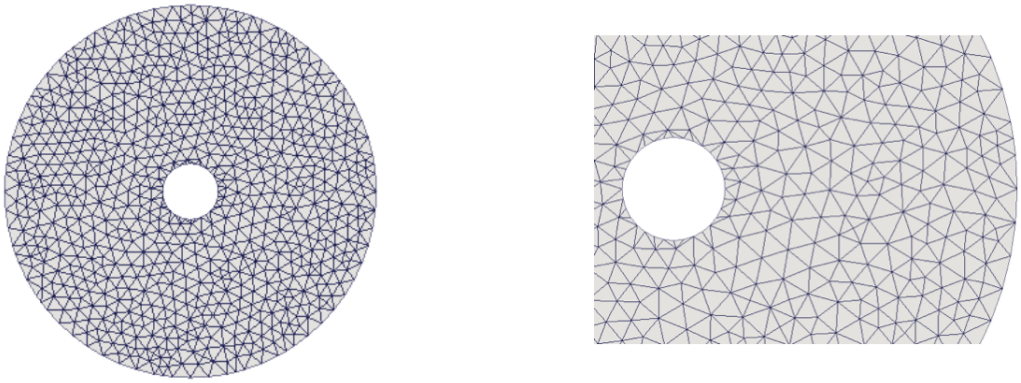

For $\rho = .15$, the initial mesh is shown on the left. On the right a zoomed in portion of the mesh is pictured so that the mesh details can be seen more easily.

Table 3.4: Mesh Details for Annulus with $\rho = .15$

Mesh	Max h	Min h	Average h	Number of Triangles
Initial Mesh	$1.09e-01$	$2.94e-02$	$7.75e-02$	$1.50e+03$
Final Mesh	$5.17e-03$	$9.20e-04$	$2.86e-03$	$1.54e+06$

We find that for all values of ρ, the domains have comparable initial and final meshes. The approximate energy minimizer, $\boldsymbol{q}_h$, is found on each annular domain using FEniCS. From this approximate solution, the order tensor Q_h is defined as in relation (3.1) and its maximal eigenvalue is calculated from which we find s_h. In Figure 3.3, s_h is plotted over the final mesh on each domain. The line field plots are not included for two reasons. The first being that they will not be well-defined for the three-dimensional concentric cylinder domains and therefore cannot be a point of comparison. Secondly, the line fields are the planar radial line fields for every ρ, an issue which will be expanded on in what follows.

We now discuss the results shown in Figure 3.3. First, notice that our Dirichlet boundary conditions force $s = 1$ on both boundaries for every ρ. Additionally, in every domain, s_h decreases away from the boundaries. As ρ decreases, the minimal value of s_h also decreases

Figure 3.3: s_h for Various Annular Domains

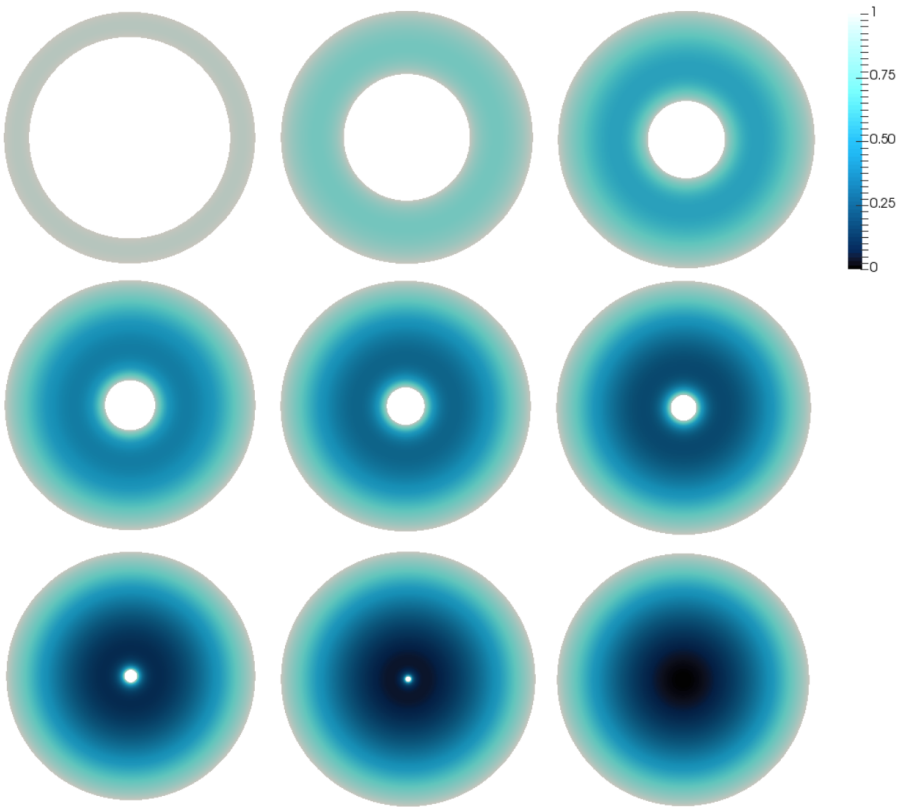

The first row from left to right shows plots of s_h over the annuli with $\rho = .8, .5, .3$. In the middle row, $\rho = .2, .15, .1$ from left to right respectively. In the final row, the plots for s_h and $\rho = .05, .02, 0$ are shown.

and approaches zero for ρ small enough, namely less that .05. Bethuel et al. predict that the escape solution should be present for these small values of ρ, but this is not reflected in our results using two-by-two Landau-de Gennes tensor. Instead, the line field becomes isotropic.

For $\rho = 0$, there is a defect located at the center of the disc as also predicted by the Oseen-Frank model. In the section that follows, the outer radius will be allowed to vary and the liquid crystal behavior of this defect is studied in further detail.

We once again consider $\rho = .15$ and study the convergence of the approximated solution to the planar radial configuration. On each mesh refinement, the planar radial configuration is interpolated onto the mesh and compared to q_h, where q_h is approximated using degree one Lagrange elements. The errors are computed and organized in to Table 3.5.

Table 3.5: Convergence with Degree 1 Elements for $\rho = .15$

Max h	Max Error	Max Order	L^2 Error	L^2 Order	H^1 Error	H^1 Order
$1.09e-01$	$2.39e-02$		$5.97e-03$		$1.28e-01$	
$8.15e-02$	$1.25e-02$	2.20	$2.21e-03$	3.37	$1.16e-01$	0.35
$4.09e-02$	$3.59e-03$	1.81	$5.64e-04$	1.98	$5.90e-02$	0.98
$2.06e-02$	$1.03e-03$	1.81	$1.41e-04$	2.02	$2.99e-02$	0.99
$1.03e-02$	$3.12e-04$	1.74	$3.50e-05$	2.02	$1.51e-02$	0.99
$5.17e-03$	$8.38e-05$	1.90	$8.72e-06$	2.01	$7.59e-03$	0.99

Clearly, the minimizing configuration is converging to the planar radial configuration. We performed the same analysis for every ρ considered above and $\boldsymbol{q}_h$ converged to the planar radial solution in every case. This implies that when minimizing the two-dimensional Landau-de Gennes energy over annular regions, the radial configuration is the only possible result. This is not unexpected under our assumptions, but these results are not in agreement with experimental evidence nor the numerical computations presented in the following chapters. This illustrates that our restrictions are too limiting to give intuition into the liquid crystal behavior in these domains.

3.6 The Radial Hedgehog in a Disc

The radial hedgehog configuration, characterized by an order +1 defect as shown in (a) of Figure 2.3, is unique because it is an explicit solution to the Landau-de Gennes Euler-Lagrange equations. Let the tensor associated with the radial hedgehog be denoted by $Q_r = h(r)(\boldsymbol{n}_r \otimes \boldsymbol{n}_r - (1/2)I)$, where $\boldsymbol{n}_r$ is the radial vector and h is a function, dependent on the radial distance r, which is the global minimizer of the following functional:

$$I[h] = \pi \int_0^R r \left[\frac{h'^2}{2} - \frac{h}{r}h' + (\frac{2}{r^2} - \frac{1}{2})h^2 + \mathcal{C}\frac{h^4}{8} \right] dr \tag{3.13}$$

This expression is the result of rewriting the two-dimensional Landau-de Gennes energy in terms of h and a detailed description of the process can be found in Section A.1 of the Appendix for the interested reader. Majumdar proves that a global minimizer of (3.13) exists and that Q_r is a solution to the Landau-de Gennes Euler-Lagrange equations:

Proposition 3.6.1. ([62], Proposition 2.1): *(a) There exists a global minimizer $h^* \in \mathcal{A}_h$ for (3.13), where $\mathcal{A}_h = \{h \in H^1([0,R],\mathbb{R}) : h(R) = 1, h(0) = 0\}$, and h^* is analytic for all $r \geq 0$.*

(b) Define the radial hedgehog solution $Q_r^*(r) = h^*(r)(\boldsymbol{n} \otimes \boldsymbol{n} - (1/2)I)$*, where* $h^*(r)$ *is the global minimizer of* (3.13)*, in the admissible space* $\mathcal{A}_h$*. Then* Q^* *is a stationary point of the Landau-de Gennes energy functional.*

Additionally, it is shown in [62] that the solution to (3.13) is uniquie.

Previous numerical results showed that the radial hedgehog is the minimizing configuration for liquid crystal droplets with homeotropic strong anchoring for radii up to a certain threshold radius r_c, after which a new minimizing configuration forms [17], [18]. In [17] and [18], the authors use the full Landau-de Gennes energy over a cross section of capillaries, i.e. discs, of varying sizes and find at least two distinct defect structures. One which corresponds to the radial hedgehog and a second which contains two $-1/2$ defects, called the *split core* solution. Mkaddem and Gartland, in [17], use two elastic terms for their calculations, while Sonnet, Killian, and Hess, in [18], use a single elastic term as in our calculations.

We are interested in comparing the minimizer found using FEniCS for radii which are both larger and smaller than r_c. Using the simplified two-dimensional version of the energy expression, it first appears that our results are consistent with these finding, but further refinement of the domain illustrates that the radial hedgehog continues to be the minimizer. This implies that as the droplet radius becomes larger, a finer mesh is needed so that the elements continue to be small enough to resolve the proper defect structure.

We now consider circular droplet domains with radii $r = L_0, 6L_0, 11L_0$, respectively. All droplets have prescribed homeotropic Dirichlet boundary conditions. For each droplet domain, the minimizer, h_h, of expression (3.13) is found using FEniCS and then interpolated onto the mesh defined over our circular region. We also interpolate the radial vector field $\boldsymbol{n}_r$ onto the droplet domain and compute $\boldsymbol{q}_r$, which is the vector associated to Q_r through relation (3.1). This exact solution is then compared to the approximate solution, $\boldsymbol{q}_h$, found from minimizing the Landau-de Gennes energy. This is first done for a course mesh. The mesh is then refined six times, snapping the boundary each time, the process is repeated, and the orders of convergence are calculated. We begin with $r = L_0$. The norms of the exact radial solution are computed and organized into Table 3.6 so that they can be compared to the computed errors.

Table 3.6: Norms for Exact Radial Hedgehog over Disc of Radius L_0

Max Norm	L^2 Norm	H^1 Norm
$5.00e-01$	$5.02e-01$	$1.84e+00$

The errors and orders using degree one Lagrange elements are calculated for $r = L_0$

and the results are summarized into the Table 3.7. Based on the orders of convergence, we find that the minimizer, $\boldsymbol{q}_h$, converges to $\boldsymbol{q}_r$. The behavior of the line field and the uniaxial order parameter, s_h, are plotted in Figure 3.4 for three mesh refinements, i.e. when the mesh has 2912 cells.

Table 3.7: Convergence with Degree 1 Elements and Radius = L_0

Max h	Max Error	Max Order	L^2 Error	L^2 Order	H^1 Error	H^1 Order
$2.67e-01$	$2.88e-03$		$1.42e-03$		$1.93e-02$	
$2.04e-01$	$2.32e-03$	0.81	$1.20e-03$	0.62	$4.19e-02$	-2.90
$1.02e-01$	$9.29e-04$	1.32	$2.99e-04$	2.01	$2.32e-02$	0.86
$5.11e-02$	$2.58e-04$	1.85	$7.45e-05$	2.01	$1.22e-02$	0.93
$2.56e-02$	$7.08e-05$	1.86	$1.85e-05$	2.01	$6.24e-03$	0.97
$1.28e-02$	$1.98e-05$	1.84	$4.63e-06$	2.00	$3.16e-03$	0.98
$6.39e-03$	$5.16e-06$	1.94	$1.16e-06$	2.00	$1.59e-03$	0.99
$3.19e-03$	$1.31e-06$	1.98	$2.92e-07$	1.99	$7.97e-04$	1.00

Figure 3.4: Line Field for Disc of Radius L_0

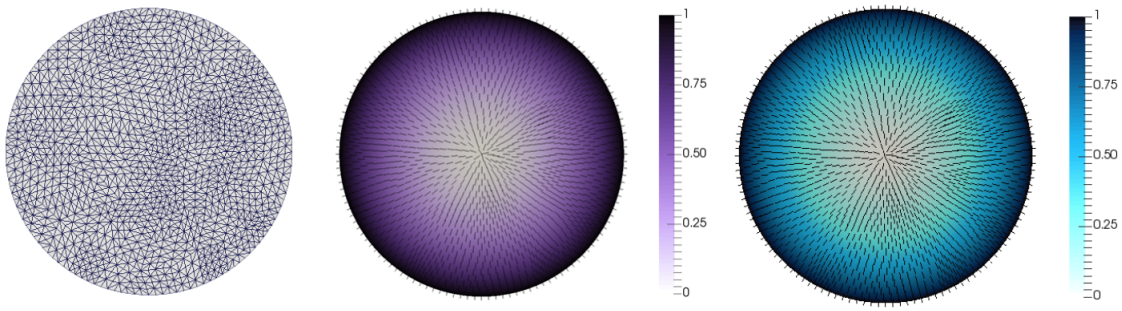

For the two-dimensional droplet of radius L_0, two mesh refinements are done so that the mesh has 2912 cells. The image on the left shows the mesh. The middle image shows the line field for the exact radial hedgehog solution with the corresponding uniaxial order parameter s_h superimposed on the domain. The image on the right contains the line field and parameter s_h for the Landau-de Gennes minimizer found using FEniCS.

Notice in Figure 3.4 that at the center, where there is a defect in the line field, s_h takes a value of zero which implies that the liquid crystal becomes isotropic at the origin. Visually, the approximate and radial solutions are indistinguishable, which is consistent with the results in Table 3.7.

Now, the radius of the droplet is increased by $5L_0$ to a value of $6L_0$. The same process as described above is repeated: $\boldsymbol{q}_h$ is found on each mesh and compared to the interpolation of $\boldsymbol{q}_r$ onto the same mesh. The norms for the exact radial hedgehog solution are calculated and organized into Table 3.8. Errors and orders of convergence using degree one Lagrange elements are organized into Table 3.9.

Table 3.8: Norms for Exact Radial Hedgehog for Disc with Radius $= 6L_0$

Max Norm	L^2 Norm	H^1 Norm
$5.00e-01$	$2.61e+00$	$3.36e+00$

Table 3.9: Convergence with Degree 1 Elements for Disc with Radius $= 6L_0$

Max h	Max Error	Max Order	L^2 Error	L^2 Order	H^1 Error	H^1 Order
$1.82e+00$	$4.77e-02$		$1.76e-01$		$2.92e-01$	
$1.45e+00$	$2.56e-02$	2.70	$5.07e-02$	5.38	$1.96e-01$	1.73
$7.24e-01$	$1.11e-02$	1.21	$1.41e-02$	1.85	$1.31e-01$	0.58
$3.62e-01$	$3.52e-03$	1.66	$3.67e-03$	1.94	$7.73e-02$	0.77
$1.81e-01$	$1.13e-03$	1.64	$9.32e-04$	1.98	$4.17e-02$	0.89
$9.05e-02$	$3.27e-04$	1.79	$2.35e-04$	1.99	$2.16e-02$	0.95
$4.52e-02$	$8.83e-05$	1.89	$5.89e-05$	2.00	$1.10e-02$	0.98
$2.26e-02$	$2.30e-05$	1.94	$1.48e-05$	2.00	$5.53e-03$	0.99

The results organized in Table 3.9 show that the minimizer continues to converge to the radial hedgehog configuration. For completeness, plots of the line field and s_h are shown in Figure 3.5 and analogous behavior to the $r = L_0$ case is evident.

Figure 3.5: Line Field for Disc of Radius $6L_0$

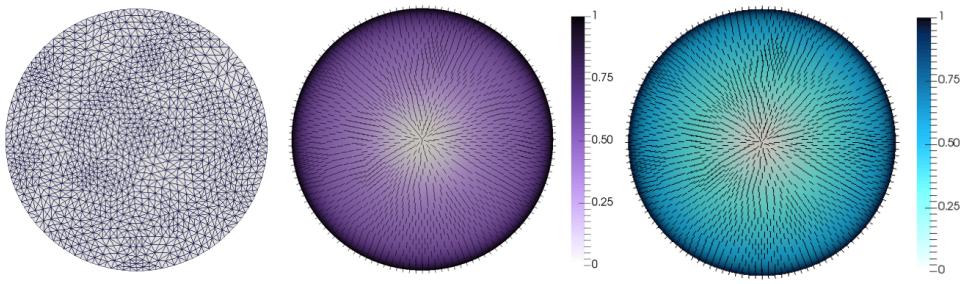

The two-dimensional droplet radius is now increased to $6L_0$. *The results for two mesh*

refinements are pictured above, i.e. mesh contains 3040 cells. On the left, the mesh is pictured. In the middle, the result of interpolating the exact radial hedgehog onto the mesh and plotting the line field with the s_h parameter superimposed over the domain is shown. The image on the right corresponds to the computed minimizing configuration.

The radius is once again increased by $5L_0$, to a value of $11L_0$. The line field associated with the approximated solution is plotted after two mesh refinements and it shows that the minimizer of the Landau-de Gennes energy no longer converges to the radial hedgehog solution, but instead to a new energy minimizing configuration where two $-1/2$ order defects occur, as seen in the right-most image in Figure 3.6. This is consistent with the numerical results in [17] and [18], even though a simplified energy expression was considered here. Sonnet et al. use the three-dimensional Landau-de Gennes energy expression with a single elastic constant over a two-dimensional domain and an iterative algorithm to find the minimizing configurations. They predict the split core will occur for a radii larger than approximately $5L_0$ [18]. Mkaddem and Gartland consider the three-dimensional Landau-de Gennes model with two elastic terms restricted to the plane and use symmetry to minimize over a quarter circle domain. Using a finite element package, they also predict that for a radius of $11L_0$ the minimizing configuration should be given by the split core [17].

Figure 3.6: Line Field for Disc of Radius $11L_0$: Course Mesh

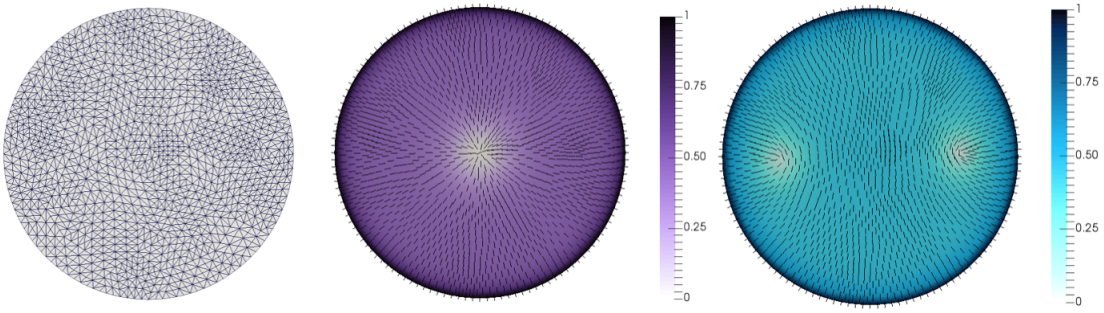

The two-dimensional droplet radius is now increased to $11L_0$. The results for two mesh refinements are pictured above, meaning the mesh contains 3040 cells. On the left, the mesh is pictured. In the middle, the result of interpolating the exact radial hedgehog onto the mesh and plotting the line field with the s_h parameter superimposed over the domain is shown. The image on the right shows the line field with s_h superimposed for the computed minimizing configuration. Notice that this right-most image is not physically realistic and further mesh refinement will prove that this configuration is not the actual minimizer.

While our calculated minimizing configuration is consistent with their numerical results, the question is to whether this result is physically realistic. When this domain is considered to be the cross section of a cylindrical capillary, such a configuration is not reported in the experimental literature. We note that, unlike our work, in previous numerical studies there is no convergence analysis included. From our order of convergence calculations, we find that with further refinement of the mesh, the split configuration is no longer present. This fact, together with the lack of experimental evidence, leads us to conclude that the split core is in fact a numerical artifact.

Consider the convergence results summarized into Table 3.10. After the fifth mesh refinement, the calculated minimizer begins to converge to the radial hedgehog solution. Note that because of the large nature of the domain, the value of maximal cell diameter is relatively large in the first few lines of this table. It is not until this diameter approaches values closer to those seen for the smaller radii that the computed minimizer begins to converge. Sonnet et al. do not provide details of the mesh they used, but Mkaddem and Gartland describe some details of their mesh. They used $4,096$ triangles in each mesh with smaller mesh elements near the origin. Since they use symmetry to minimize over a quarter of a circle, their elements were $\sim 10^{-2}L_0$ in diameter. Comparing with the maximal values of h in Table 3.10, it is reasonable to conclude that the mesh they were using may not have been fine enough.

Table 3.10: Convergence with Degree 1 Elements for a Disc of Radius $11L_0$

Max h	Max Error	Max Order	L^2 Error	L^2 Order	H^1 Error	H^1 Order
$3.14e+00$	$2.17e-01$		$3.89e+00$		$4.16e+00$	
$2.35e+00$	$2.16e-01$	0.01	$2.95e+00$	0.96	$3.19e+00$	0.92
$1.17e+00$	$2.22e-01$	-0.04	$2.81e+00$	0.07	$3.05e+00$	0.07
$5.87e-01$	$2.09e-01$	0.08	$2.80e+00$	0.01	$3.02e+00$	0.01
$2.94e-01$	$2.21e-01$	-0.08	$2.80e+00$	0.00	$3.01e+00$	0.00
$1.47e-01$	$1.48e-03$	7.23	$1.40e-03$	10.96	$6.92e-02$	5.45
$7.34e-02$	$4.28e-04$	1.79	$3.52e-04$	1.99	$3.54e-02$	0.97
$3.67e-02$	$1.15e-04$	1.89	$8.81e-05$	2.00	$1.79e-02$	0.99

Table 3.11: Norms for Exact Radial Hedgehog over a Disc of Radius $11L_0$

Max Norm	L^2 Norm	H^1 norm
$5.00e-01$	$4.68e+00$	$5.39e+00$

For $r = 11L_0$, the energy per unit area on each mesh is also computed and organized into

Table 3.12. Interestingly, the exact radial hedgehog has more energy on the very course mesh, but as the mesh is refined it reduces to nearly a third of the original value and converges to the same energy value as the numerically computed solution.

Table 3.12: Energy Values per Unit Area for a Disc of Radius $= 11L_0$

NumCells	Calculated Energy Minimizer	Energy for Radial Hedgehog
190	$1.93e-02$	$2.61e-02$
760	$1.34e-02$	$1.60e-02$
3040	$9.63e-03$	$1.15e-02$
12160	$8.21e-03$	$9.84e-03$
48640	$7.79e-03$	$9.31e-03$
194560	$9.15e-03$	$9.18e-03$
778240	$9.13e-03$	$9.13e-03$
3112960	$9.13e-03$	$9.13e-03$

We plot the line field and s_h parameter for the final mesh refinement. Note that some simplification must be done since the mesh is very dense and the details of the line field could not be seen if all elements were shown. Figure 3.7 shows the exact radial hedgehog solution and the approximate solution corresponding to only $7,000$ elements.

Figure 3.7: Line Field for Disc of Radius $11L_0$: Fine Mesh

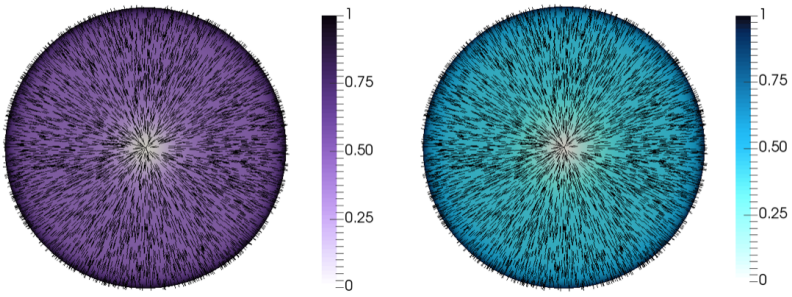

Using degree one elements and a mesh with 3112960 cells, the line fields with the s_h parameter superimposed are plotted for a two-dimensional droplet of radius $11L_0$. For visualization purposes, the number of line elements shown is reduced to 7,000. The image on the left is the result of interpolating the exact radial hedgehog solution onto the mesh. The image on the right corresponds to the approximate solution.

Clearly, the exact radial hedgehog solution is also the energy minimizing configuration for $r = 11L_0$. Of course, it is not possible to test every droplet radius, but we found

that doubling the radius of the droplet resulted in similar behavior. Although, it initially appeared that the split core solution was the minimizer, further mesh refinements resulted in convergence to the radial hedgehog solution. This is evidence that there is a strong correlation between the size of the domain considered and the mesh refinement necessary for the elements of the mesh to be small enough to resolve the correct minimizing configuration. Before concluding that a numerically predicted phenomenon, not reported in experimental literature, is indeed new, further refining of the mesh to increase numerical accuracy should be performed.

3.7 Single Particle in a Square Box

A main goal of this work is to study liquid crystal configurations of a cylinder enclosing a particle, as presented in Chapter 4. Everywhere vertical boundary conditions are imposed on the boundary of the cylinder and homeotropic boundary conditions are prescribed on the particle surface. Experimental evidence suggests that in such a confining geometry, a Saturn ring defect will form around the particle [31],[33]. In this chapter, we are interested in whether using the simplified two-dimensional Landau-de Gennes energy expression over a two-dimensional domain results in a consistent minimizer, that is with two $-1/2$ defects aligned with the equator of the particle. To explore this issue, consider a square box of sidelengths $4L_0$ with a circular particle domain of radius $.5L_0$ removed from its center. On the particle, normal Dirichlet boundary conditions are prescribed, as described by (3.4). On the square boundary, everywhere vertical boundary conditions are imposed as in (3.5). We compute the energy minimizing configuration, $\boldsymbol{q}_h$, over the mesh shown in Figure 3.8, and show the result, in terms of the line field and the uniaxial order parameter s_h, over this domain in the image on the right.

By a comparison with Figure 2.3 and the definition of the degree of the defect, we conclude that the line field in Figure 3.8 has two $-1/2$ defects aligned with the equator of the particle. We also find that, s_h approaches a value of zero, which further confirms the presence of these defects. If this domain is viewed as the cross section of a spherical particle suspended in a cylinder, this configuration is consistent with the existence of a Saturn ring in a three-dimensional domains studied in Chapter 4. It is important to note that this agreement is purely qualitative since in reality the defect cores are not isotropic regions, as suggested by the behavior of s_h here, but instead biaxial regions.

Our computed energy minimizer agrees with previous numerical results. Tasinkevych, Silvestre, Patrício, and Telo Da Gama use the two-dimensional Landau-de Gennes energy

Figure 3.8: Line Field for a Square with Disc Removed

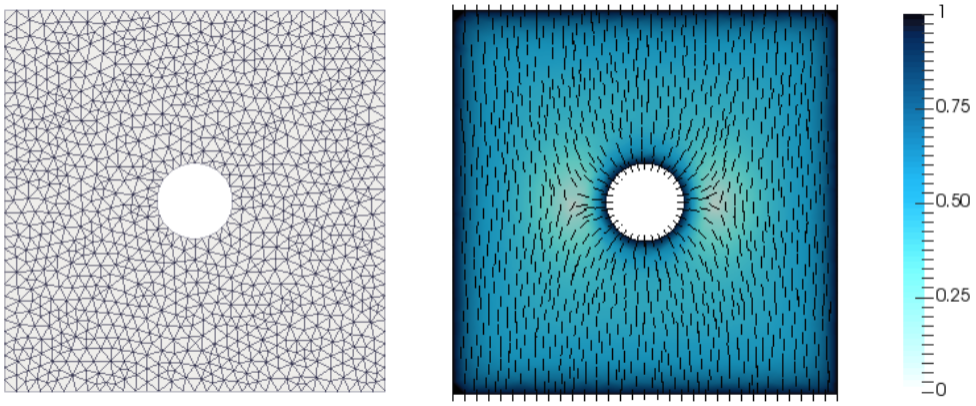

The mesh for a single particle suspended in a liquid crystal filled box is shown on the left. The right image is the result of numerically computing the minimizing configuration and plotting the associated line field with the uniaxial order parameter s_h superimposed.

expression considered here and finite elements to find analogous energy minimizing configuration as seen in Figure 3.8 [50]. In [44], Fukuda and Yokoyama use an adaptive grid and an explicit scheme to show that the configuration resulting from our numerical results is the only possible minimizer for a single particle in two dimensions. In their article, a variety of parameter values are considered all of which result in the Saturn ring defect structure. Even when an initial condition in which a point defect configuration, characterized by a single -1 order defect, is chosen, the resulting configuration is still characterized by two $-1/2$ defects along the equator of the particle.

3.8 Two Particles in a Box

In three dimensions, two spherical particles in a cylindrical domain will also be studied. This is not a rotationally symmetric domain, but studying the minimizer on a cross section can give some qualitative understanding of the behavior and allows us to compare our results with work done previously.

Consider a square of sidelengths $4L_0$ with two circles of radius $.3L_0$ removed along the x-axis. The outer boundary will have everywhere vertical Dirichlet boundary conditions, given by (3.5), and the particle surfaces will both have homeotropic Dirichlet boundary conditions as defined by (3.4). The energy will be computed and compared as the distance between

the two particles decreases, similar to the work done by Tasinkevych et al. in [50]. They also consider a two-dimensional domain and their results show that as the distance between the two particles decreases, the energy of the system decreases. It has been experimentally verified that for two colloidal particles with Saturn ring defects, the force between them is initially attractive, but once they have reached an equilibrium configuration, they will lie at a nonzero distance from one another. If forced closer together, there is a repulsive force between the two particles [32]. We consider particle separations in both the repulsive and the attractive regimes, respectively.

From experimental evidence, we know that defect regions will form relatively close to the particles. Because of this, after the initial mesh is defined, we take a circle which encompasses both particles and refine the mesh further in this region ensuring to snap the boundary elements. For every interparticle distance, the domain will have $15,850 \pm 100$ cells in the mesh. In Figure 3.9, an example is presented for $d = 2.4L_0$, where d is the distance between the particle centers. In this case, the maximal cell diameter is $1.52e^{-01}L_0$, the minimal cell diameter is $5.82e^{-02}L_0$, and the average is $1.08e^{-01}L_0$. The mesh contains $15,866$ cells.

Figure 3.9: Mesh for a Square with Two Discs Removed

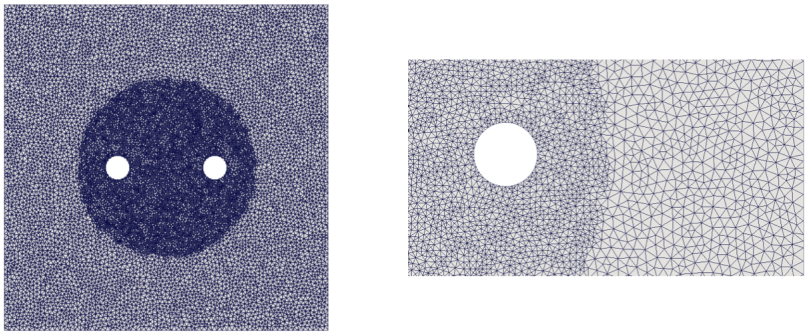

For $d = 2.4L_0$, the distance between the particle centers, the mesh is displayed on the left. A zoomed in portion of the mesh is shown on the right in order to show the mesh details more clearly.

We vary d and calculate the energy values. These energy values can be found in a table seen in Figure 3.10. Further mesh refinements give the same energy values and we are confident that the energy values converge to those seen in this table.

Figure 3.10: Energy for Various Disc Separations

d	Energy
4.0	9.82
3.2	9.77
2.4	9.71
1.6	9.63
1.4	9.60
1.2	9.58
1.0	9.56
.80	9.64
.75	9.72
.7	9.90

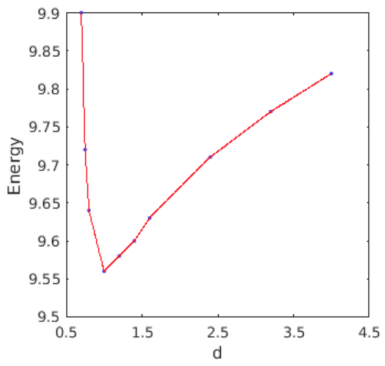

The table on the left, summarizes the dimensionless energy values for interparticle distances, d, in units of L_0. The right shows a plot of the results.

Figure 3.11: s_h Plots for Various Disc Separations

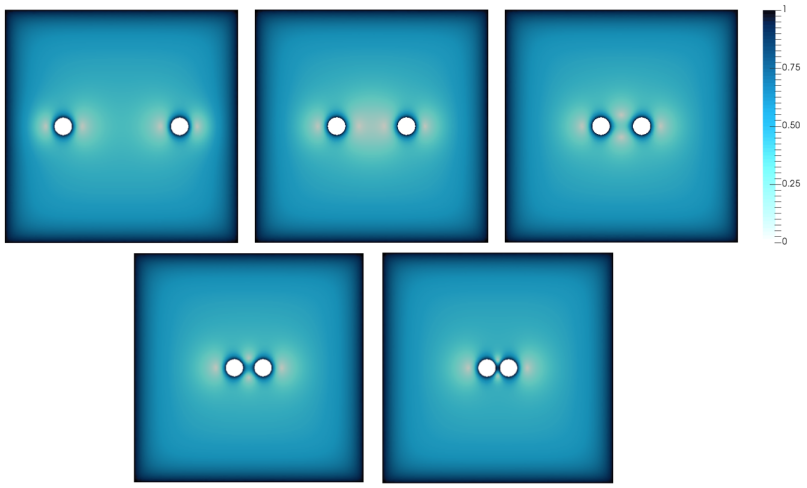

From left to right in the top row, the s_h parameter is plotted for $d = 4, 2.4, 1.4$, in units of L_0, and on the second row $d = 1, .75L_0$ respectively.

Starting from the value $d = 4$, as d decreases, the energy also decreases suggesting the presence of an attractive force. Once d reaches a value of $.8L_0$, decreasing d results in an increase in the energy value over the domain, which is consistent with a repulsive force between the two particles. For $d = 4, 2.4, 1.4, 1, .75$, in units of L_0, the s_h parameter is plotted in Figure 3.11. Comparing these results with those is Figure 3.10, the energy of the

system is decreasing when the defect region between the two particles merges. The minimal energy occurs for $d = L_0$. In this case, the defect region between the two particles now has a central region in which $s = 1$. This is consistent with the equilibrium configurations seen in experiments with two particles [33]. In these experiments, a third Saturn ring forms between the two particles normal to the Saturn rings around each particle, which is referred to as the *entangled hyperbolic defect*.

It is important to note, that for all the simulations considered in this Chapter, the reduction of dimension in domain and energy expression allows for illustration of some of the qualitative behavior of the system, but these are not physically realistic simplifications. Two-dimensional liquid crystal domains cannot occur. In many instances, defect regions are regions in which the liquid crystal becomes biaxial, but the restriction of our energy expression to two dimensions does not allow for such behavior. Otherwise complex defect regions have been simplified to isotropic as the uniaxial order parameter takes the value $s = 0$. In the chapters that follow, a three-dimensional Landau-de Gennes energy expression will be used and allow us to resolve more robust and accurate results in a variety of domains.

Chapter 4

Numerical Simulations in Three Dimensions

In this Chapter, FEniCS will be used to find energy minimizing configurations in three-dimensional geometries. A variety of domains will be considered. For the concentric cylinder domains, significantly different results from the predictions of the Oseen-Frank model have been uncovered. Previous studies using Oseen-Frank resolved two possible minimizing configurations, both of which are uniaxial. In our computations, we find three configurations which transition continuously to one another. These domains show some degree of biaxial behavior, which is impossible to resolve with the Oseen-Frank model. In the case of the droplet, our results confirm theoretical predictions that the center of the droplet will have a biaxial region and the resulting configuration will have lower energy than the radial hedgehog defect. For the single particle domain, the conclusions of Schpohl and Sluckin, which claim that at the center of the Saturn ring is a region where the parameter s becomes negative [19], are numerically confirmed for the first time. The final domain considered consists of a two particle system in a cylinder where the defect region is consistent with previous experimental and numerical results.

4.1 Three Dimensional Weak Energy Expression

We employ a finite element method over tetrahedra to find the minimizing configurations in three-dimensional liquid crystal domains. We begin with the dimensionless energy (2.39) given by:

$$E(Q) = \int_\Omega \frac{1}{2}|\nabla Q|^2 - \frac{1}{2}\text{tr } Q^2 + \frac{\mathcal{B}}{3}\text{tr } Q^3 + \frac{\mathcal{C}}{4}(\text{tr } Q^2)^2 \, d\boldsymbol{x} \tag{4.1}$$

We express the energy in terms of the components of our symmetric traceless tensor Q where:

$$Q = \begin{bmatrix} q_0 & q_2 & q_3 \\ q_2 & q_1 & q_4 \\ q_3 & q_4 & -(q_0+q_1) \end{bmatrix}. \tag{4.2}$$

We rewrite the bulk terms as follows:

$$\begin{aligned}
\text{tr } (Q^2) &= (q_0+q_1)^2 + q_0^2 + q_1^2 + 2q_2^2 + 2q_3^2 + 2q_4^2 \\
(\text{tr } (Q^2))^2 &= ((q_0+q_1)^2 + q_0^2 + q_1^2 + 2q_2^2 + 2q_3^2 + 2q_4^2)^2 \\
\text{tr } (Q^3) &= 2q_3(q_2q_4 - q_1q_3) + 2q_4(q_2q_3 - q_0q_4) + q_0(q_0^2 + q_2^2 + q_3^2) \\
&\quad + q_1(q_1^2 + q_2^2 + q_4^2) + 2q_2(q_0q_2 + q_1q_2 + q_3q_4) - (q_0+q_1)((q_0+q_1)^2 + q_3^2 + q_4^2)
\end{aligned}$$

The elastic energy is now expanded in terms of the components of Q leading to the following expression:

$$\begin{aligned}
E(\boldsymbol{q}) = \int_\Omega (&\frac{\partial q_0}{\partial x}^2 + \frac{\partial q_0}{\partial y}^2 + \frac{\partial q_0}{\partial z}^2 + \frac{\partial q_1}{\partial x}^2 + \frac{\partial q_1}{\partial y}^2 + \frac{\partial q_1}{\partial z}^2 \\
&+ \frac{\partial q_2}{\partial x}^2 + \frac{\partial q_2}{\partial y}^2 + \frac{\partial q_2}{\partial z}^2 + \frac{\partial q_3}{\partial x}^2 + \frac{\partial q_3}{\partial y}^2 + \frac{\partial q_3}{\partial z}^2 \\
&+ \frac{\partial q_4}{\partial x}^2 + \frac{\partial q_4}{\partial y}^2 + \frac{\partial q_4}{\partial z}^2 + \frac{\partial q_0}{\partial x}\frac{\partial q_1}{\partial x} + \frac{\partial q_0}{\partial y}\frac{\partial q_1}{\partial y} + \frac{\partial q_0}{\partial z}\frac{\partial q_1}{\partial z}) \\
&- \frac{1}{2}[(q_0+q_1)^2 + q_0^2 + q_1^2 + 2q_2^2 + 2q_3^2 + 2q_4^2] \\
&+ \frac{1}{3}\mathcal{B}[2q_3(q_2q_4 - q_1q_3) + 2q_4(q_2q_3 - q_0q_4) \\
&\quad + q_0(q_0^2 + q_2^2 + q_3^2) + q_1(q_1^2 + q_2^2 + q_4^2) \\
&\quad + 2q_2(q_0q_2 + q_1q_2 + q_3q_4) - (q_0+q_1)((q_0+q_1)^2 + q_3^2 + q_4^2)] \\
&+ \frac{1}{4}\mathcal{C}[(q_0+q_1)^2 + q_0^2 + q_1^2 + 2q_2^2 + 2q_3^2 + 2q_4^2]^2 \; d\boldsymbol{x}
\end{aligned} \tag{4.3}$$

Let $\boldsymbol{q} = (q_0, q_1, q_2, q_3, q_4)$ and $\boldsymbol{q} \in \tilde{W}^{1,2}(\Omega) = \{\boldsymbol{p} \in H^1(\Omega) | \boldsymbol{p} = \boldsymbol{g} \text{ on } \partial\Omega\}$ where $\boldsymbol{g}$ is prescribed on the domain boundary $\partial\Omega$. For $\boldsymbol{\nu} = (\nu_0, \nu_1, \nu_2, \nu_3, \nu_4) \in W_0^{1,2}(\Omega) = \{\boldsymbol{p} \in H^1(\Omega) |\ \boldsymbol{p} = \boldsymbol{0} \text{ on } \partial\Omega\}$, the first variation of (4.3) results in the following five expressions:

$$\begin{aligned}
For\ q_0 : &\int_\Omega (2\nabla q_0 + \nabla q_1)\cdot\nabla\nu_0 + [-(2q_0+q_1) + \mathcal{B}(-q_4^2 + q_0^2 + q_2^2 - (q_0+q_1)^2) \\
&+ \mathcal{C}((q_0+q_1)^2 + q_0^2 + q_1^2 + 2q_2^2 + 2q_3^2 + 2q_4^2)(2q_0+q_1)]\nu_0 \; d\boldsymbol{x} \\
For\ q_1 : &\int_\Omega (2\nabla q_1 + \nabla q_0)\cdot\nabla\nu_1 + [-(q_0+2q_1) + \mathcal{B}(-q_3^2 + q_1^2 + q_2^2 - (q_0+q_1)^2) \\
&+ \mathcal{C}((q_0+q_1)^2 + q_0^2 + q_1^2 + 2q_2^2 + 2q_3^2 + 2q_4^2)(q_0+2q_1)]\nu_1 \; d\boldsymbol{x}
\end{aligned}$$

$$
\begin{aligned}
For\ q_2 : &\int_\Omega 2\nabla q_2 \cdot \nabla \nu_2 + [-(2q_2) + \mathcal{B}(2q_3q_4 + 2q_0q_2 + 2q_1q_2) \\
&+ \mathcal{C}((q_0+q_1)^2 + q_0^2 + q_1^2 + 2q_2^2 + 2q_3^2 + 2q_4^2)(2q_2)]\nu_2 \ d\boldsymbol{x} \\
For\ q_3 : &\int_\Omega 2\nabla q_3 \cdot \nabla \nu_3 + [-(2q_3) + \mathcal{B}(-2q_1q_3 + 2q_2q_4) \\
&+ \mathcal{C}((q_0+q_1)^2 + q_0^2 + q_1^2 + 2q_2^2 + 2q_3^2 + 2q_4^2)(2q_3)]\nu_3 \ d\boldsymbol{x} \\
For\ q_4 : &\int_\Omega 2\nabla q_4 \cdot \nabla \nu_4 + [-(2q_4) + \mathcal{B}(2q_2q_3 - 2q_0q_4) \\
&+ \mathcal{C}((q_0+q_1)^2 + q_0^2 + q_1^2 + 2q_2^2 + 2q_3^2 + 2q_4^2)(2q_4)]\nu_4 \ d\boldsymbol{x}
\end{aligned}
$$

Combining the above, the weak Euler-Lagrange equations are given by:

$$
\begin{aligned}
I(\boldsymbol{q}) = \int_\Omega &(2\nabla \boldsymbol{q} : \nabla \boldsymbol{\nu} + \nabla q_1 \cdot \nabla \nu_0 + \nabla q_0 \cdot \nabla \nu_1) - (2\boldsymbol{q} \cdot \boldsymbol{\nu} + q_1\nu_0 + q_0\nu_1) \\
&+ \mathcal{B}[(-q_4^2 + q_0^2 + q_2^2 - (q_0+q_1)^2)\nu_0 + (-q_3^2 + q_1^2 + q_2^2 - (q_0+q_1)^2)\nu_1 \\
&\quad + (2q_3q_4 + 2q_0q_2 + 2q_1q_2)\nu_2 + (-2q_1q_3 + 2q_2q_4)\nu_3 + (2q_2q_3 - 2q_0q_4)\nu_4] \\
&+ \mathcal{C}((q_0+q_1)^2 + q_0^2 + q_1^2 + 2q_2^2 + 2q_3^2 + 2q_4^2)(2\boldsymbol{q} \cdot \boldsymbol{\nu} + q_1\nu_0 + q_0\nu_1) \ d\boldsymbol{x} = \boldsymbol{0}
\end{aligned}
\tag{4.4}
$$

where $A : B$ denotes the Frobenius inner product.

4.2 Visualization of the Minimum Energy Configuration

Visualization of three-dimensional results has added complications, one reason being the nature of the domain itself. When plotting data over the entire domain, the details in the interior cannot be seen clearly. Furthermore, the presence of biaxiality does not allow for a clear representation of the line field since there is no single direction of alignment. Therefore the line field is only illustrative in domains with highly concentrated defect regions. In the case where these biaxial regions are not highly concentrated, plotting the biaxiality parameter seems to be the best way to visualize the minimizing configuration.

In order to assemble the piecewise polynomials over tetrahedron to solve (4.4), we proceed as follows: First, a mesh composed of disjoint tetrahedron is defined over the domain using *mshr*, the mesh generation component of FEniCS. By invoking the 'NonlinearVariationalSolver' class, Newton's method is used to find an approximate solution, $\boldsymbol{q}_h$. We then find the tensor Q_h with the use of relation (4.2). From Section 2.8 in Chapter 2, we know $\boldsymbol{n}$ is the eigenvector associated with the dominant eigenvalue of Q and the parameters s and r are defined in terms of the eigenvalues of Q. Using these facts, we calculate $\boldsymbol{n}_h$, s_h, and r_h from Q_h, write the results to a *pvd* file, and process them in Paraview, an application

for interactive, scientific visualization. These quantities are plotted over the entire domain. Depending on the domain considered, either a cross section of the data is shown or we remove an appropriate portion of the domain and show the remaining partial domain, which will be referred to as a *clip*.

The biaxiality parameter, β, as described in Section 2.8 of Chapter 2 is also used to visualize the resulting energy minimizing configuration. We calculate the approximate value β_h from Q_h using (2.15), export it to a *pvd* file, and then visualize it in Paraview. Cross sections and clips are used to see the behavior of β_h in the interior of the domain. In domains with particle interaction, an *isovolume* for $\beta \in (.7, 1)$ will also be plotted, which allows us to visualize the entire defect region. Let us recall that an isovolume of β is the part of the domain where β takes values in a certain interval.

4.3 Boundary Conditions for Three Dimensional Domains

Either by rubbing or by the use of a surfactant, rigid attachment of the liquid crystal molecules can be prescribed. This is referred to as strong anchoring and is mathematically realized by defining a Dirichlet boundary condition. Since the alignment is assumed to be perfect on the boundary, Q will be uniaxial with $s = 1$, which implies $Q = \boldsymbol{n} \otimes \boldsymbol{n} - (1/3)I$. Radial, planar radial, and everywhere vertical boundary conditions will be used in simulations. For radial boundary conditions, $\boldsymbol{n}_r = (x_0/|\boldsymbol{x}|, x_1/|\boldsymbol{x}|, x_2/|\boldsymbol{x}|)$, where $|\boldsymbol{x}| = \sqrt{x_0^2 + x_1^2 + x_2^2}$. Relation (4.2) allows us to express the boundary conditions in terms of the components of Q. Since

$$Q = \begin{vmatrix} x_0^2/|\boldsymbol{x}|^2 - 1/3 & (x_0x_1)/|\boldsymbol{x}|^2 & (x_0x_2)/|\boldsymbol{x}|^2 \\ (x_0x_1)/|\boldsymbol{x}|^2 & x_1^2/|\boldsymbol{x}|^2 - 1/3 & x_1x_2/|\boldsymbol{x}|^2 \\ x_0x_2/|\boldsymbol{x}|^2 & x_1x_2/|\boldsymbol{x}|^2 & x_2^2/|\boldsymbol{x}|^2 - 1/3 \end{vmatrix} = \begin{vmatrix} q_0 & q_2 & q_3 \\ q_2 & q_1 & q_4 \\ q_3 & q_4 & -(q_0 + q_1) \end{vmatrix},$$

this implies:

$$\begin{aligned} q_0 &= \frac{x_0^2}{|\boldsymbol{x}|^2} - \frac{1}{3}, q_1 = \frac{x_1^2}{|\boldsymbol{x}|^2} - \frac{1}{3}, q_2 = \frac{x_0x_1}{|\boldsymbol{x}|^2} \\ q_3 &= \frac{x_0x_2}{|\boldsymbol{x}|^2}, q_4 = \frac{x_1x_2}{|\boldsymbol{x}|^2}. \end{aligned} \tag{4.5}$$

For everywhere vertical boundary conditions, $\boldsymbol{n}_v = (0, 0, 1)$ and the components of Q have the following values:

$$q_0 = \frac{-1}{3}, q_1 = \frac{-1}{3}, q_2 = 0 = q_3 = q_4 \tag{4.6}$$

When planar radial boundary conditions are assumed, $\boldsymbol{n}_{pr} = (x_0/|\boldsymbol{x}|, x_1/|\boldsymbol{x}|, 0)$, where $|\boldsymbol{x}| = \sqrt{x_0^2 + x_1^2}$. Such a Dirichlet boundary condition can be expressed in terms of the components of Q using relations (4.2):

$$\begin{aligned} &q_0 = \frac{x_0^2}{|\boldsymbol{x}|^2} - \frac{1}{3}, q_1 = \frac{x_1^2}{|\boldsymbol{x}|^2} - \frac{1}{3}, q_2 = \frac{x_0 x_1}{|\boldsymbol{x}|^2} \\ &q_3 = q_4 = 0. \end{aligned} \tag{4.7}$$

4.4 Manufactured Solution for Concentric Cylinders

We begin our three-dimensional simulations in a similar fashion as Chapter 3 and consider a manufactured solution. In this case, the liquid crystal domain will be the region bounded by two concentric cylinders with inner radius $.5L_0$, outer radius of L_0, and height $2L_0$. We define Dirichlet boundary so that the director is planar radial on the lateral sides of the cylinders as well as the top and bottom surfaces. Once again, we choose the manufactured solution based on the minimizing solutions found by Bethuel et al. [20]. Recall that $e^{-\pi}$ is the threshold value between the planar radial and escape solution. We choose as our manufactured solution the planar radial configuration, since this is the minimizer predicted for our domain parameters. Note, since we are considering the Landau-de Gennes energy, we do not claim that this is indeed the minimizer for our energy expression. Instead, this provides an appropriate manufactured solution.

We first need to calculate the forcing term, $\boldsymbol{f}$, associated to the manufactured solution. Note that relation (4.7) gives the manufactured solution $\boldsymbol{q}_m = (x_0^2/(x_0^2+x_1^2) - 1/3, x_1^2/(x_0^2+x_1^2) - 1/3, (x_0x_1)/(x_0^2+x_1^2), 0, 0)$. Each component of $\boldsymbol{f}$ is then equal to:

$$\begin{aligned} f_0 &= -\nabla^2(2q_0 + q_1) - (2q_0 + q_1) + \mathcal{B}(-q_1^2 + q_2^2 - q_4^2 - 2q_0q_1) + \\ &\quad + \mathcal{C}(2q_0 + q_1)(2q_0^2 + 2q_1^2 + 2q_0q_1 + 2q_2^2 + 2q_3^2 + 2q_4^2) \\ &= 2\frac{(x_0^2 - x_1^2)}{(x_0^2 + x_1^2)^2} - \left(\frac{2x_0^2 + x_1^2}{x_0^2 + x_1^2} - 1\right) \\ &\quad + \mathcal{B}\left[-\left(\frac{x_1^2}{x_0^2 + x_1^2} - \frac{1}{3}\right)^2 + \left(\frac{x_0x_1}{x_0^2 + x_1^2}\right)^2 - 2\left(\frac{x_0^2}{x_0^2 + x_1^2} - \frac{1}{3}\right)\left(\frac{x_1^2}{x_0^2 + x_1^2} - \frac{1}{3}\right)\right] \\ &\quad + \mathcal{C}\left(\frac{2x_0^2 + x_1^2}{x_0^2 + x_1^2} - 1\right)(2/3) \\ f_1 &= -\nabla^2(q_0 + 2q_1) - (q_0 + 2q_1) + \mathcal{B}(-q_0^2 + q_2^2 - q_3^2 - 2q_0q_1) + \\ &\quad + \mathcal{C}(q_0 + 2q_1)(2q_0^2 + 2q_1^2 + 2q_0q_1 + 2q_2^2 + 2q_3^2 + 2q_4^2) \\ &= -2\frac{(x_0^2 - x_1^2)}{(x_0^2 + x_1^2)^2} - \left(\frac{x_0^2 + 2x_1^2}{x_0^2 + x_1^2} - 1\right) \end{aligned}$$

$$
\begin{aligned}
&+\mathcal{B}\left[-\left(\frac{x_0^2}{x_0^2+x_1^2}-\frac{1}{3}\right)^2+\left(\frac{x_0x_1}{x_0^2+x_1^2}\right)^2-2\left(\frac{x_0^2}{x_0^2+x_1^2}-\frac{1}{3}\right)\left(\frac{x_1^2}{x_0^2+x_1^2}-\frac{1}{3}\right)\right]\\
&+\mathcal{C}\left(\frac{x_0^2+2x_1^2}{x_0^2+x_1^2}-1\right)(2/3)\\
f_2 &= -2\nabla^2(q_2)-(2q_2)+\mathcal{B}(2q_0q_2+2q_1q_2+2q_3q_4)+\\
&\quad+\mathcal{C}(2q_2)(2q_0^2+2q_1^2+2q_0q_1+2q_2^2+2q_3^2+2q_4^2)\\
&= \frac{8x_0x_1}{(x_0^2+x_1^2)^2}-2\frac{x_0x_1}{x_0^2+x_1^2}\\
&\quad+\mathcal{B}\left[2\left(\frac{x_0^2}{x_0^2+x_1^2}-\frac{1}{3}\right)\left(\frac{x_0x_1}{x_0^2+x_1^2}\right)+2\left(\frac{x_1^2}{x_0^2+x_1^2}-\frac{1}{3}\right)\left(\frac{x_0x_1}{x_0^2+x_1^2}\right)\right]\\
&\quad+\mathcal{C}\left(2\frac{x_0x_1}{x_0^2+x_1^2}\right)(2/3)\\
f_3 &= -2\nabla^2(q_3)-(2q_3)+\mathcal{B}(-2q_1q_3+2q_2q_4)+\\
&\quad+\mathcal{C}(2q_3)(2q_0^2+2q_1^2+2q_0q_1+2q_2^2+2q_3^2+2q_4^2)\\
&= 0\\
f_4 &= -2L\nabla^2(q_4)+A(2q_4)+B(-2q_0q_4+2q_2q_3)+\\
&\quad+C(2q_4)(2q_0^2+2q_1^2+2q_0q_1+2q_2^2+2q_3^2+2q_4^2)\\
&= 0
\end{aligned}
$$

The left-hand side of the weak Euler Lagrange equations (4.4) is then set equal to the weak form of the forcing term:

$$I(\boldsymbol{q}) = \int_\Omega \boldsymbol{f}\cdot\boldsymbol{\nu}\, d\Omega \tag{4.8}$$

The approximated solution, $\boldsymbol{q}_h$, to (4.8) is first calculated over the initial mesh shown in Figure 4.1. We then interpolate the manufactured solution, $\boldsymbol{q}_m$, onto this mesh and compare it to $\boldsymbol{q}_h$. The mesh is refined several times and this process is repeated on each mesh. The details of the initial and final mesh are summarized in Table 4.1, where h is the cell diameter.

Table 4.1: Mesh Details for Concentric Cylinders with $\rho = .5$

Mesh	Max h	Min h	Average h	Number of Triangles
Initial Mesh	$5.90e-01$	$2.85e-01$	$4.57e-01$	$8.53e+02$
Final Mesh	$1.33e-01$	$3.40e-02$	$6.59e-02$	$4.07e+05$

We find the errors between the manufactured solution and the approximate solution on each mesh. The maximal cell diameter is used to compute the orders of convergence for

Figure 4.1: Initial Mesh for Concentric Cylinders

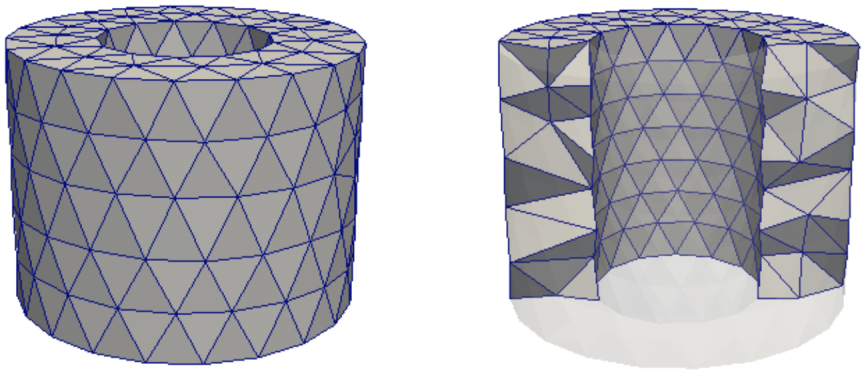

The image on the left shows the initial mesh over the entire domain. On the right, half of the meshed domain is removed in order to better see the mesh details in the interior of the domain.

the minimization done with both degree one and two Lagrange elements and the results are summarized in the Tables 4.2 and 4.3.

Table 4.2: Convergence using Degree 1 Elements in Concentric Cylinder Domain

Max h	Max Error	Max Order	L^2 Error	L^2 Order	H^1 Error	H^1 Order
$5.90e-01$	$2.95e-02$		$1.11e-02$		$1.28e-01$	
$3.81e-01$	$1.60e-02$	1.41	$7.64e-03$	0.85	$1.87e-01$	-0.87
$2.51e-01$	$8.80e-03$	1.43	$3.18e-03$	2.11	$1.44e-01$	0.63
$1.33e-01$	$2.89e-03$	1.75	$8.90e-04$	2.00	$8.15e-02$	0.90

Table 4.3: Convergence using Degree 2 Elements in Concentric Cylinder Domain

Max h	Max Error	Max Order	L^2 Error	L^2 Order	H^1 Error	H^1 Order
5.90e-01	7.38e-03		5.16e-03		6.77e-02	
3.81e-01	2.25e-03	2.73	7.36e-04	4.47	3.27e-02	1.67
2.51e-01	6.99e-04	2.80	1.30e-04	4.16	1.09e-02	2.62
1.33e-01	1.06e-04	2.97	1.69e-05	3.19	2.90e-03	2.08

The values in the tables above show that the approximated solution, $\boldsymbol{q}_h$, is indeed converging to the manufactured solution, $\boldsymbol{q}_m$. This allows us to continue our numerical computing with confidence. The concentric cylinder domain will be further studied in the following section to allow for further comparison with the results obtained from the Oseen-Frank energy expression discussed in [20].

4.5 Concentric Cylinders

The behavior of liquid crystals in concentric cylinder domains, with planar radial strong anchoring on the lateral boundaries, has been studied by various of authors. As mentioned in Chapter 3, Bethuel et al. use the Oseen-Frank energy expression to show that energy minimizing configurations are dependent on ρ, the ratio of the inner radius to the outer radius. The relevant theorems of this paper were summarized in Section 3.5. If $\rho \geq e^{-\pi} = .0432$, the planar radial solution is the minimizing configuration and if $\rho < e^{-\pi}$ the minimizer is given by the escape solution, where this solution is characterized by uniaxial behavior everywhere and a nonzero z-component which increases as we move away from the bounding surfaces [20]. These analytical results were later verified numerically by Alouges and Coleman in [63]. The use of Oseen-Frank in these two articles restricts the possible minimizing configurations to those which are unaxial everywhere. In [21], Biscari and Virga consider using the Landau-de Gennes energy over this domain. They find that when the bulk energy is neglected, the energy minimizer is biaxial everywhere for all ρ, except at the boundaries where boundary conditions are defined. For $\rho = 0$, i.e. a solid cylinder, they show that the minimizer must be the escape solution with uniaxial behavior along the cylinders axis.

In this Section, the Landau-de Gennes energy is used to show that three configurations, which depend continuously on ρ, occur for liquid crystal bounded between two cylinders. For all domains, the outer cylinder will have radius and height L_0, and inner radius ρL_0. Planar radial Dirichlet boundary conditions will be defined on the lateral sides of both cylinders. Under these assumptions, every domain shows some biaxial behavior, but it will not occur everywhere away from the boundaries as hypothesized by Biscari and Virga. Note that since no boundary conditions are explicitly defined on the top and bottom boundaries, this implies that the our strong form of the energy now has a homogeneous Neumann boundary condition. FEniCS has the advantage that natural boundary conditions can be treated without a need to change the code.

In order to illustrate the transitions between the minimizing configurations, we consider nine values of ρ and plot β_h over each domain. Before delving into the results, the mesh details are presented for the domain with inner radius $\rho = .2$ in Figure 4.2 and Table 4.4. This is taken as a representative example of the mesh used for each ρ.

Using FEniCS, we compute $\boldsymbol{q}_h$ on each mesh and subsequently calculate β_h. In Figure 4.3, β_h is plotted over the entire domain and a clip is shown for $\rho = .8, .5, .3$ in order to illustrate how the biaxial region develops away from the lateral boundaries. For ρ large,

Table 4.4: Mesh Details for Concentric Cylinders with $\rho = .2$

Max h	Min h	Average h	Number of Triangles
$4.92e-02$	$1.39e-02$	$3.09e-02$	$3.31e+06$

Figure 4.2: Example Mesh for Concentric Cylinders

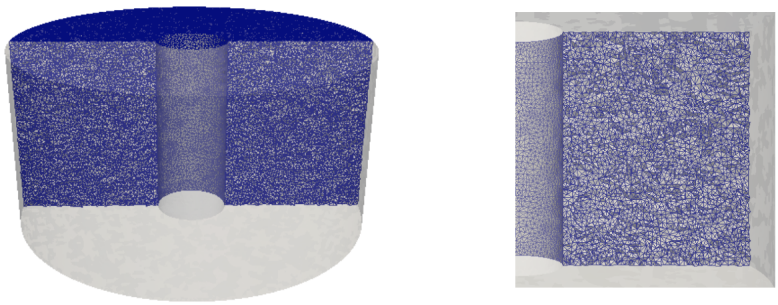

A clip of the mesh for $\rho = .2$ is shown in the image on the left. On the right, a zoomed in portion of the mesh illustrates some of the finer details.

a fully uniaxial configuration appears to be present, but when studied more carefully, the biaxiality parameter is never zero in the entire domain. Although their plots will not be shown here, values of ρ as large as .95 were considered and no fully uniaxial domain was found. As the radius of the inner cylinder decreases, the biaxial region between the two cylinders becomes more prominant.

Figure 4.3: β_h for Concentric Cylinders with Large ρ

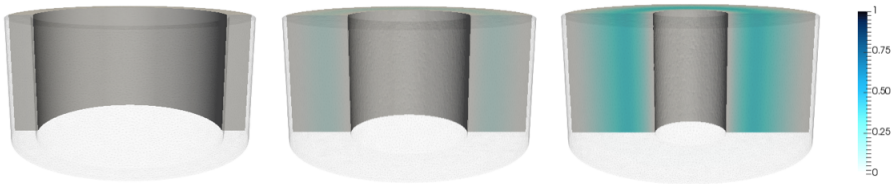

A clip of the biaxiality parameter β_h is shown for $\rho = .8, .5, .3$ moving from left to right.

In Figure 4.4, β_h is plotted over the concentric cylinder domains with $\rho = .2, .15, .1$. As ρ decreases, the size of the biaxial region continues to increase and its value starts to approach its maximal value of one. As ρ is decreased even further, this maximally biaxial region splits and a region with a lower biaxiality begins to form in its interior.

Figure 4.4: β_h for Concentric Cylinders with Mid-Range ρ

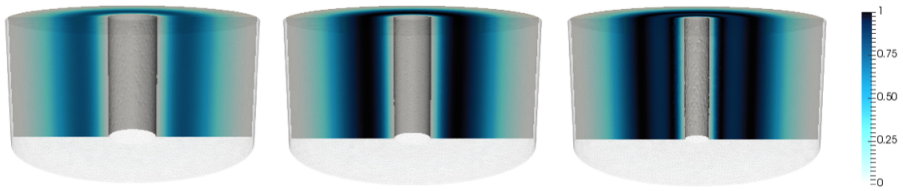

A clip of the biaxiality parameter β_h is shown for $\rho = .2, .15, .1$ moving from left to right.

Figure 4.5 shows the plots of β_h for $\rho = .05, .02, 0$. The region in which the biaxiality parameter is not maximal, but located in the interior of a maximally biaxial region, continues to take smaller values as ρ is decreased. For an inner radius of $.02L_0$, a value of zero will be reached by the biaxiality parameter, meaning the liquid crystal has once again become uniaxial. This final transition corresponds to the escape solution.

Figure 4.5: β_h for Concentric Cylinders with Small ρ

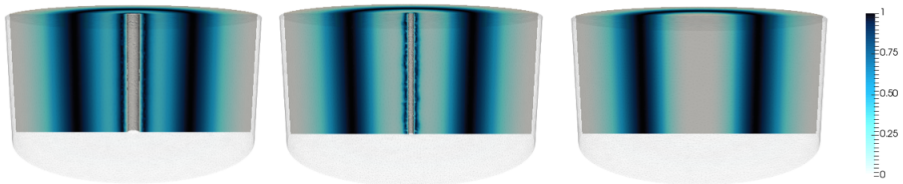

A clip of the biaxiality parameter β_h is shown for $\rho = .05, .02, 0$ moving from left to right.

Careful analysis of the β parameter gives us a good understanding of the liquid crystal alignment. Consider the plot for $\rho = .02$ in Figure 4.5. On the lateral cylindrical boundaries, the biaxiality parameter is equal to zero. This is due to the fact that on these boundaries, Dirichlet boundary conditions were defined and the behavior was therefore assumed uniaxial. Moving away from both the inner and outer lateral boundaries, the liquid crystal transitions into a highly biaxial behavior and the line field no longer has one preferred direction of alignment. This transition occurs quickly away from the inner boundary and gradually away from the outer boundary. Between these two cylindrical regions, which are maximally biaxial, there is again a uniaxial region. Here, the uniaxial alignment is no longer planar, but instead has a nonzero z-component, which implies that the configuration is the escape solution. Using the Oseen-Frank energy expression, Bethuel et al. predicted that

the transition to the escape solution occurs at $\rho = e^{-\pi} \approx .0432$. Although $\rho = .03$ is not shown above, we found from our simulations that the full escape solution occurs between $\rho = .02 - .03$, which is in close agreement with the threshold they predicted.

While this aspect of our results has qualitative agreement with the work in Bethuel et al. there are many marked difference between their results and our numerical computations. Above the threshold $\rho = e^{-\pi}$, they predict a purely uniaxial planar radial solution which we never find. Also, unlike their results, we find that the transition between different minimizing configurations is a continuous one. Additionally, the escape solution described in [20] is a configuration which is uniaxial everywhere and whose z-component increases from a value of zero on the boundaries to a value of one in the interior of the domain, while our escape solution has large biaxial regions.

When the inner radius is equal to zero, the escape region occurs along the central axis. If the radius of the solid cylinder is allowed to vary, this escape solution is always present which is consistent with the results presented by Biscari and Virga when the bulk term is ignored [21]. There are a number of theoretical works which predict that as the radius of the cylinder approaches zero, the purely planar radial solution should be the minimizer. In experiments testing this hypothesis, the planar radial solution was never found and they conclude that the curvature of the confining walls creates a high elastic energy that competes with the anchoring energy and results in the directors tilting away from their prefered anchoring direction preventing the transition to the planar radial configuration [64]. In [7], Cladis and Kleman show, using Oseen-Frank, that when molecules are allowed to relax out of the plane, the energy is always lower then the purely radial solution except when the radius is on the order of molecular lengths in which case the continuum theory breaks down.

4.6 Spherical Droplet

As discussed in the previous Chapter, the radial hedgehog is a rare example of an explicit solution of the Landau-de Gennes Euler-Lagrange equations. Such a configuration is hypothesized to exist for droplets with radial anchoring on the surface. For this reason, two spherical liquid crystal droplet domains with homeotropic Dirichlet boundary conditions are considered. The energy value over the domain of the computed minimizing configuration is compared with the energy given by the radial hedgehog. It will be evident that the biaxial region which forms in the center of the droplet of the approximate solution causes a departure from this explicit solution.

The radial hedgehog is given by $Q_r = h(r)(\boldsymbol{n}_r \otimes \boldsymbol{n}_r - (1/3)I)$ where $\boldsymbol{n}_r$ is the radial vector and $h(r)$ is the minimizer of the following energy expression:

$$I[h] = \int_0^R 4\pi \left[\frac{1}{3}h'^2 - \frac{1}{3\rho}hh' + (\frac{2}{\rho^2} - \frac{2}{3})h^2 + \frac{2\mathcal{B}}{27}h^3 + \frac{\mathcal{C}}{9}h^4\right] \rho^2 \, d\rho \tag{4.9}$$

This expression develops from the formulation of the Landau-de Gennes energy in terms of h and the derivation can be found in Section A.2 of the Appendix. The results developed by Majumdar, as discussed in Section 3.6, extend to the radial hedgehog in three dimensions. Therefore, we know that a unique global minimizer, h^*, of (4.9) exists and is unique and, furthermore, the radial hedgehog solution $Q_r^*(r) = h^*(r)(\boldsymbol{n}_r \otimes \boldsymbol{n}_r - (1/3)I)$ is a stationary point of the Landau-de Gennes energy functional.

The radial hedgehog is, therefore, a reasonable candidate for the energy minimizer and we are interested in how it compares to the configuration found by minimizing that Landau-de Gennes energy. As stated, two liquid crystal droplet domains with strong homeotropic surface anchoring and with radii L_0 and $3L_0$ will be considered. First consider a droplet with radius L_0. After an initial mesh is defined for the domain, further refinement is done in the center of the droplet, in order to resolve the defect region more clearly. In Figure 4.6 the mesh used for the numerical computations is shown. In Table 4.5 infomation about the cell diameters, h, is summarized.

Table 4.5: Mesh Details for Droplet of Radius L_0

Max h	Min h	Average h	Number of Cells
$1.46e-01$	$1.34e-02$	$7.70e-02$	$2.09e+05$

In most of the domain, except for a very small region at the center of the droplet, β_h equals 0. This implies that the liquid cystal is uniaxial nearly everywhere and the line field is an informative way to visualize the behavior of the liquid cystal. In Figure 4.7, a plot of the line field and the values of β_h are shown for the droplet of radius L_0.

The line field associated with the approximate solution, $\boldsymbol{q}_h$, appears to be that of the exact radial hedgehog, but the plot of the biaxiality parameter illustrates that this is not the case. In the radial hedgehog configuration, the line field is uniaxial everywhere and the defect is represented by the behavior $s = 0$. Isotropic melt is not energetically favorable, since we are considering a parameter regime for the deep nematic, and therefore the formation of a biaxial region at the center of the droplet is reasonable. Additionally, an isotropic defect core is not physically realistic. When comparing the energy of the computed minmizer for Landau-de Gennes energy expression and the radial hedeghog, their values are

Figure 4.6: Mesh for Droplet with Radius L_0

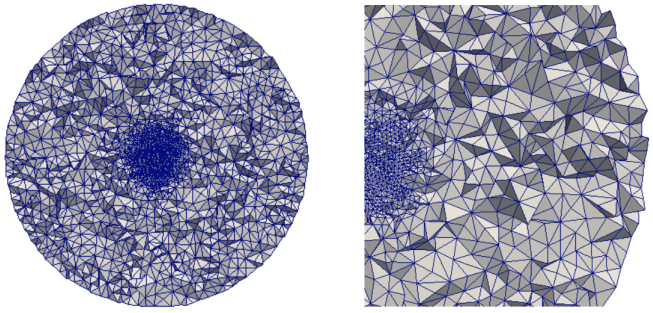

A clip of the mesh for a droplet of radius one is shown on the left. On the right, a zoomed in portion of the mesh shows the refinement in the center of the droplet.

Figure 4.7: Line Field and β_h Plots for Droplet with Radius L_0

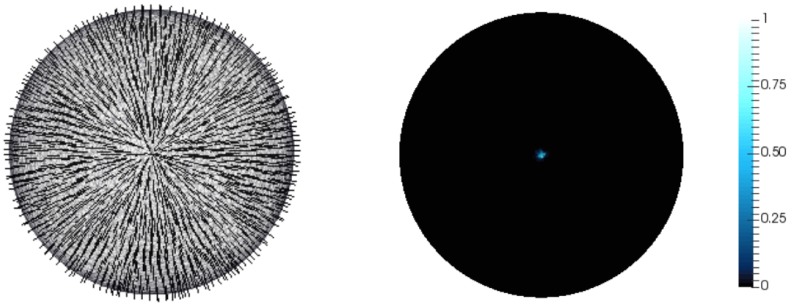

A cross section of the line field and biaxiality parameter for a liquid crystal droplet of radius L_0 are plotted on the left and right, respectively.

nearly identical for a droplet of this size as can be seen in Table 4.6. This is due to the fact that the biaxial region is extremely small, and so the effect of the energy increase at the defect is marginal in comparison to the energy over the whole domain

Table 4.6: Energies for a Droplet of Radius L_0

Number of Cells	Computed Minimizer	Radial Hedgehog
1247	7.72	7.78
12032	7.71	7.73
94822	7.76	7.77
748986	7.77	7.77

As the radius of the particle is increased, the line field and β_h parameter plots look identical to the smaller droplet, but the energy of the approximate solution of the Landau-de Gennes energy functional will have markedly smaller energy. To illustrate this, now consider a droplet with radius $3L_0$. As in the case of the smaller droplet, after an initial mesh is defined, further refinement is done in the center where experimental evidence suggests a biaxial region forms. The mesh looks similar to that of radius L_0, and the details of this mesh are summarized in Table 4.7

Table 4.7: Mesh Details for Droplet of Radius $3L_0$

Max h	Min h	Average h	Number of Cells
$4.46e-01$	$3.92e-02$	$2.18e-01$	$2.26e+05$

Once again, the biaxial region is highly concentrated in the center of the droplet and the line field is clearly represented away from this region. A cross section of the β_h parameter and the line field are shown in Figure 4.8.

Figure 4.8: Line Field and β_h Plots for Droplet with Radius $3L_0$

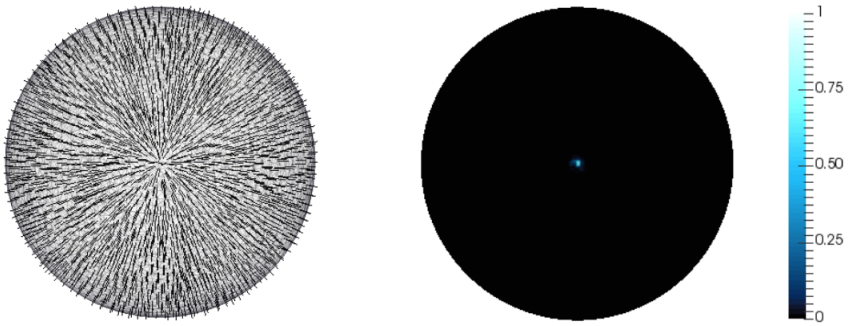

A cross section of the line field and β_h for a liquid crystal droplet of radius $3L_0$ are plotted on the left and right respectively.

This line field and biaxiality parameter plot are strikingly similar to that of the droplet with radius L_0, but the effects of increasing the radius are evident when comparing the energy values of the computed minimizer with those of the radial hedgehog. As we see in Table 4.8, the minimizer found for the Landau-de Gennes energy expression, $\boldsymbol{q}_h$, has a lower energy value.

Table 4.8: Energies for a Droplet of Radius $3L_0$

Number of Cells	Computed Minimizer	Radial Hedgehog
1230	7.59	8.95
11222	7.60	9.35
91107	7.53	9.35
725106	7.50	9.34

These results are not unexpected. In [65], Penzenstadler and Trebin use analytic arguments and the Landau-de Gennes energy expression to conclude that a radial configuration with a biaxial core has a lower energy and is therefore more stable than a totally uniaxial configuration. Furthermore, Schopohl and Sluckin conclude that the defect cores are always biaxial [19], which supports the behavior we find for both liquid crystal droplets considered.

4.7 Single Particle

We now consider a spherical colloidal particle of radius $.5L_0$ suspended in a cylinder of radius $2L_0$ and height $4L_0$ filled with 5CB. On the surface of the particle, homeotropic Dirichlet boundary conditions are prescribed. On the cylinder surface, we enforced everywhere vertical Dirichlet boundary conditions. Minimizing the Landau-de Gennes energy, the behavior of the line field and the biaxiality parameter allow us to conclude that a Saturn ring defect forms around the equator of the particle, which is consistent with the behavior of liquid crystal colloids in confined domains.

The minimization is done on a mesh in which smaller elements are used near the particle surface, since the defect region is known to occur in this region. Moving away from the particle, larger elements are used due to the fact that theoretical and experimental evidence suggests that the liquid crystal is uniaxial away from these concentrated defect regions. The details of the mesh are organized into Table 4.9 and the mesh is shown in Figure 4.9.

Table 4.9: Mesh Details for Single Particle

Max h	Min h	Average h	Number of Cells
$4.29e-01$	$5.67e-03$	$2.48e-02$	$8.73e+06$

Since the defect region is highly concentrated, there is a single preferred direction of alignment in a majority of the domain and the line field has a good representation. Because of the three-dimensional nature of the domain, a cross section of the line field is needed in

Figure 4.9: Mesh for Single Particle in Cylinder

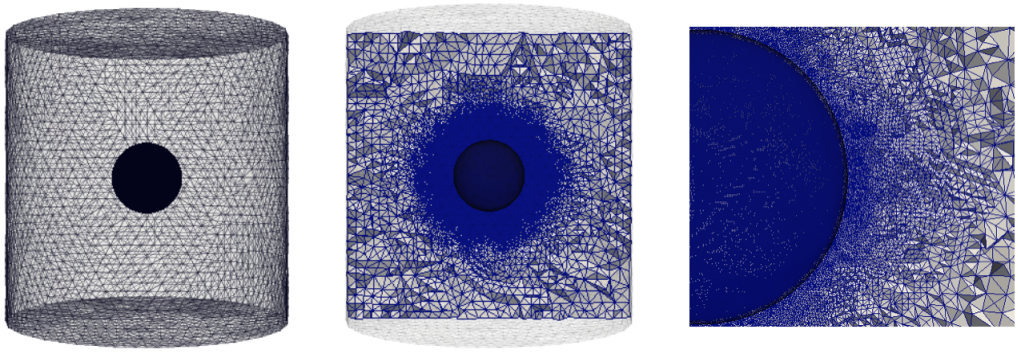

On the far left, the entire meshed domain is shown. In the center, a crinkle clip along the yz-plane shows the relative size of the mesh elements. The high concentration of small elements near the particle surface make it difficult to see the details around the particle surface, so the right-most image shows a zoomed in portion around the particle.

order to see the details in the interior. This cross section is taken along the yz-plane and shown on the left in Figure 4.10. On the right of this Figure, the zoomed in portion of the line field clearly shows two $-1/2$ defects as described in Figure 2.3 of Chapter 2.

Figure 4.10: Line Field for a Single Particle in Cylinder

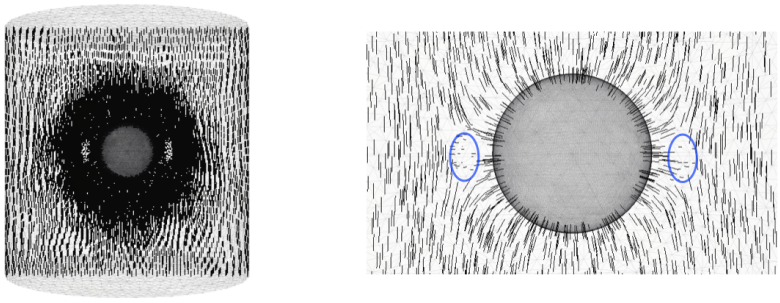

The left image shows a cross section along the yz-plane of the line field over the entire domain. On the right, a zoomed in portion of this cross section is shown. The two ellipses aligned with the equator of the particle denote the defect regions. From the behavior of the surrounding line field, it is clear that these defects both have order $-1/2$.

The presence of these two $-1/2$ defects is further confirmed by the behavior of the biaxiality parameter. β_h is plotted over the entire domain and a cross section is taken along

the yz-plane and shown in the image on the right in Figure 4.11. The entire Saturn ring defect can be seen by plotting the isovolume for $\beta \in (.7, 1)$ and as shown on the left in Figure 4.11.

Figure 4.11: β_h Plot for Single Particle in Cylinder

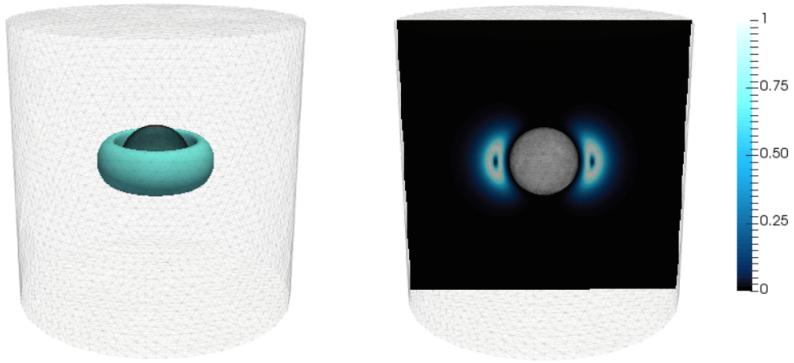

The image on the left shows the isovolume for $\beta \in (.7, 1)$. A cross section of the biaxiality parameter is shown on the right.

As seen in the cross section of the β_h, the Saturn ring defect has a uniaxial core. As mentioned in the Chapter 2, Schopohl and Sluckin study the core of $-1/2$ disclinations in the plane using Landau-de Gennes and explain that while the tensor attains a uniaxial structure at the core of the defect, the order parameter becomes negative which results in the director field restricted to the plane perpendicular to the dominant eigenvalue direction [19]. Based on Figure 4.10, we hypothesize that the core of the Saturn ring defect also has negative scalar order parameter. To confirm this is indeed the case, the parameters s_h and r_h are plotted over the domain. In Figure 4.12, a cross section of the plots for the parameters r_h and s_h are shown in the second row. The cross section of the biaxiality parameter is shown again in the first row in order to provide a side-by-side comparison. It is clear that the region which appears to be uniaxial, when considering the biaxiality parameter, is indeed a region in which $s_h = r_h = -s_0$, where s_0 is the uniaxial scalar order parameter as decribed in (2.14). This is the first time that the defect core has numerically been shown to reflect the analytic conclusions developed by Schopohl and Sluckin [19].

Defect cores were originally believed to be regions where isotropic melt occurred. This hypothesis can be partially attributed to use of vector field dependent models in which this was the only way that defect regions could be described. Later, experimentalist suggested that defect cores were actually regions of biaxiality. Schopohl and Sluckin use an analytic

Figure 4.12: β_h, s_h, and r_h Plots for Single Particle in Cylinder

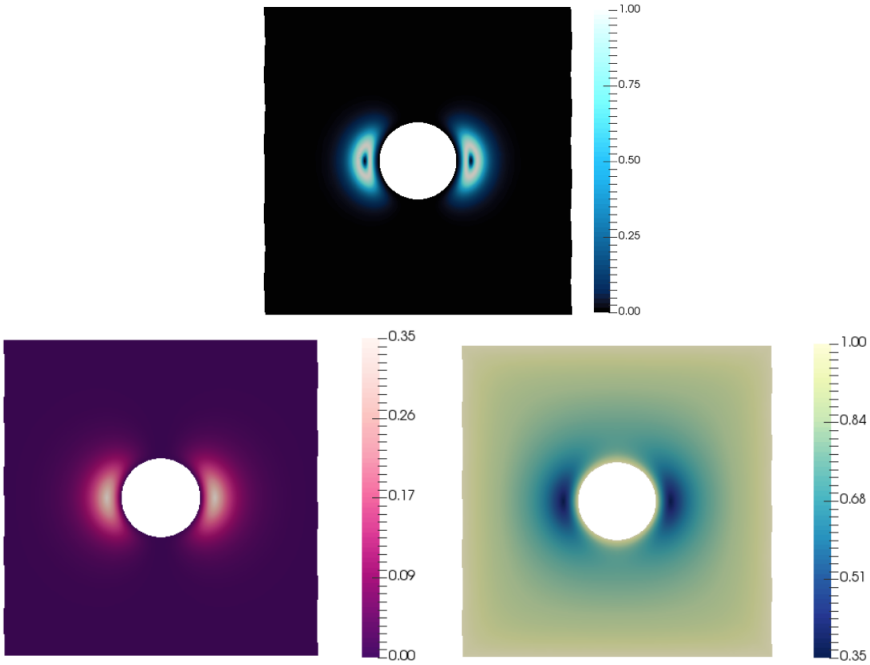

Cross sections of the plots for β_h, r_h and s_h for a single particle with normal Dirichlet boundary conditions are shown. The top-most image shows a cross section of the biaxiality parameter. In the second row, cross sections of the r_h and s_h parameter are shown on the left and right, respectively.

argument to argue that the defect cores are not purely biaxial, but instead, transition from a biaxial region to a uniaxial region with negative order parameter at the center. We note, that this is not inconsistent with purely biaxial defects believed to be seen in experiments. When Q is uniaxial with scalar order parameter, the alignment of the molecules is confined to the plane normal to the dominant eigenvector, but the ordering in the plane is completely random which can give the appearance of isotropic or biaxial orientation when studied under cross polarizers.

Some additional numerical work was done for single particle domains, but we do not include a detailed description and instead summarize the results briefly. We studied various domains with the particle radius fixed at a value L_0 and varied the outer radius. The goal of these computations is to show that a relatively large particle would result in a point defect as discussed in [66], [67], [68], and experimentally verified in [69]. However, a point defect was never resolved for the domains we considered, but this is not in contradiction to previous

results. First note that earlier numerical works considered unbounded domains, while our calculations were all done in bounded domains [67] [68]. Also, experiments where hedgehog defects were present were done in relatively large containers, where the bounding domain was approximately 100 times larger than the particle radius. Later experiments suggested that defect formation is strongly dependent on the size of the confining domain. Gu and Abbot in [31], perform experiments with particles of diameter $40\mu m$ and $100\mu m$ in a cell of diameter $120\mu m$ and conclude that in a bounded domain the preferred defect will be the Saturn ring. This was further confirmed experimentally in [33]. In this case, Musevic et al. consider many particles in a cell. In thinner parts of the cell, the colloidal particles were surrounded by Saturn rings, while in thicker regions, the accompanying defects were hedgehogs. The effects of confinement using the Oseen-Frank model gave similar conclusions. Stark in [37], using the Oseen-Frank energy expression, shows that in the presense of a magnetic field the resulting defect will always be a Saturn ring and in [70] concludes that magnetic fields generate a similar behavior as confinement. In other words, a confining geometry also results in a Saturn ring defect when the energy minimization is done using a vector-field dependent model.

Note the difference in the results of this section with those using a two-dimensional energy expression. In Chapter 3, the line field also reflected the presence of two $-1/2$ defects along the equator of the particle, but in that case the defect region was much smaller. Additionally, the s parameter had a completely different behavior. In two-dimensions, it approached a value of zero in the defect core, implying isotropic melt. In the case considered in this section, the core has a zero-valued outer region and it becomes negative at the center. Clearly, the simplication of the tensor Q can only give a qualitative understanding in this domain and only under the assumption that the defects will be understood as regions where $s = 0$, when in fact they are biaxial.

4.8 Two Particles

When multiple particles with Saturn ring defects are allowed to move freely in a liquid crystal medium, the defects join to form chain-like systems [33], [60]. To better understand these large systems, the mechanism of defect joining must be studied for a smaller number of particles. We consider a domain in which two colloidal particles are suspended in a cylinder filled with nematic liquid crystal. Let the cylinder have height $4L_0$ and radius $2L_0$ with everywhere vertical Dirichlet boundary conditions defined on the lateral surfaces as well and on the top and bottom. The particles have radius $.3L_0$ and are placed along the y-axis

equidistant from the central axis of the cylinder. On both particles, homeotropic Dirichlet boundary conditions are defined. We find that when the distance between the two particles is large enough, two independent Saturn ring defects form around each particle. As they are brought closer to one another, the defect region that lies between them connects. As they continue to move closer together, the connected region opens up to form a third ring which is perpendicular to the two rings surrounding each particle, and referred to as the entangled hyperbolic defect [33].

From experiments, it is known that this defect region occurs relatively close to the particles. Therefore, we define a mesh with smaller elements around the particles so that the defect structures are well represented. We analyze many different particle separations and compute the energy of the system. First, a representative mesh is considered. Let the distance between the center of the particles be $1.2L_0$. The mesh is shown in Figure 4.13 and its details are summarized in Table 4.10.

Table 4.10: Mesh Details for Two Particles in a Cylinder

Max h	Min h	Average h	Number of Triangles
$3.17e-01$	$9.22e-03$	$4.87e-02$	$4.05e+06$

Figure 4.13: Example Mesh for Two Particles in Cylinder

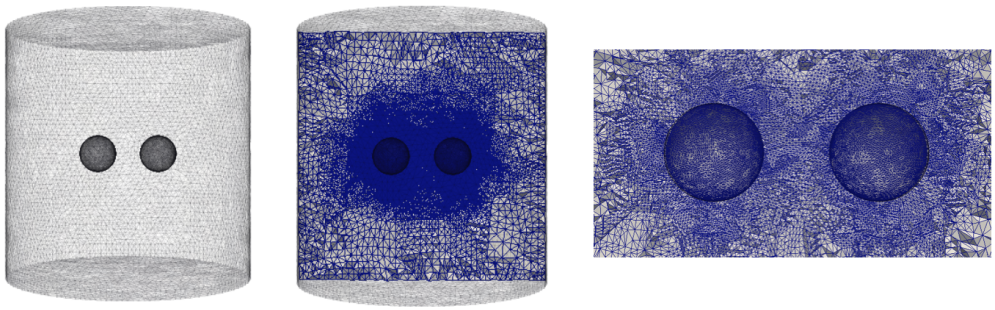

The mesh for a particle separation of $1.2L_0$ *is shown. The middle image shows a clip in order to see the mesh in the interior of the domain. The right-most image is a zoomed in portion around the two particles.*

To illustrate the formation of the entangled hyperbolic defect structure, we plot the biaxiality parameter for various particle separations. Let d denote the distance between the centers of the particles and consider $d = 1.6, 1.2, 1, .8, .7, .625$ in units of L_0. We calculate β_h over the entire domain and show a cross section in Figure 4.14. In Figure 4.15, the

isovolumes for $\beta \in (.7, 1)$ are plotted for all values of d. In these plots, the domains are shown from a top down view of the cylinders in order to better see the details of the defect regions.

Figure 4.14: β_h for Various Particle Separations

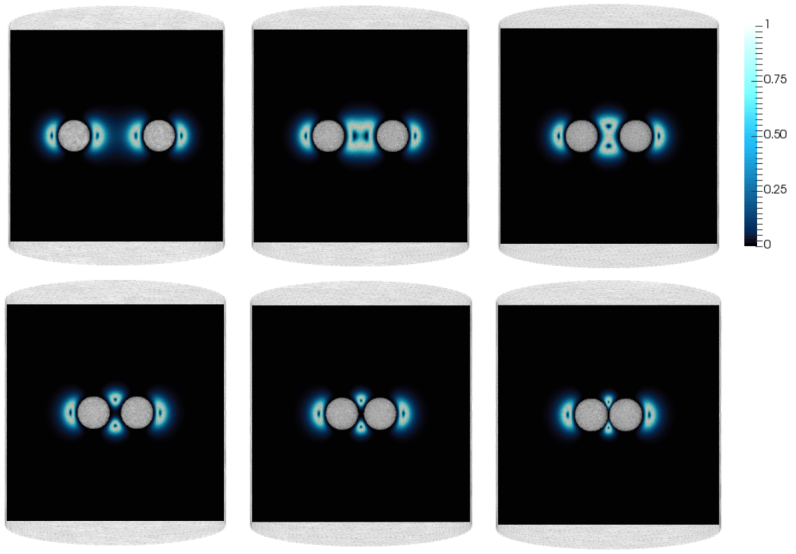

In the first row, the cross section for β_h for $d = 1.6, 1.2, 1$, in units L_0, are shown. In the second row, the cross sections correspond to $d = .8, .7, .625$ from left to right.

At an initial separation of $1.6L_0$, the particles have two completely separate Saturn ring defects. For $d = 1.2L_0$, we see that the defect region which lies between the two particles has now joined. Figure 4.14 shows that the interior defect region opens into a ring to form the entangled hyperbolic defect for d between $.8L_0$ and L_0. In [48], Guzman, Kim, Grollau, Abbott, and de Pablo claim that this transition occurs when d is less than $.9L_0$, which is consistent with our results. Later in [49], they predict that this transition occurs at a value of $d = .95L_0$, which continues to be consistent with our results. Note that neither of these articles include a study of the intermediate defect structure as we have shown here.

As previously mentioned in Chapter 3, two particles with Saturn ring defects begin to attract one another at a certain separation and repel each other if the separations becomes too small. For various values of d, the energy of the system was calculated and organized into the table seen if Figure 4.16. The plot on the right of this figure clearly shows that the computed energy minimizers also reflect this attractive and repulsive behavior. In experiments [33] and numerical calculations [49], strong attraction first appears over separations,

Figure 4.15: β_h Isovolumes for Various Particle Separations

The isovolumes for $\beta \in (.7, 1)$ are shown from a top down view of the cylinders. These isovolume correspond to the cross sections in Figure 4.14. In the first row, we have $d = 1.6, 1.2, 1$ from left to right and in the second row $d = .8, .7, .625$ respectively, where d is measured in units of L_0.

measured from particle surfaces, which are two times the diameter of the particle. In terms of d, strong attaction appears for $d = 1.8L_0$ in our simulations and explains why there is an immediate reduction in energy when d is decreased. From Figures 4.14 and 4.15, it is clear that this reduction corresponds to the two Saturn ring defects interacting and then joining in the region between the two particles. In experiments, the system reaches equilibrium at a nonzero separation and the defect structure is that of the entangled hyperbolic defect. This defect structure and energy minimum appear to occur for $d = .7 - .75L_0$ for our computations. Once d becomes less than $.7L_0$, the energy begins to increase as the separation decreases. This is consistent with the presence of a repulsive force between the two particles. In [49], Kim et al. use Monte Carlo simulations and dynamic field theory to study the same system. They find that for a separation less than $.7L_0$, the spheres strongly repel, and the minimum energy will occur for $d = .7$, which is consistent with the results in Figure 4.16. Using local thermal quenching, Ravnik et al. calculate that the equilibrium separation, measured from the particles surfaces, is fifty percent of the particle radius [60]. This corresponds to a value of $d = .75$ and is in close agreement with the energy values in Figure 4.16 as well.

In some experimental systems, the colloids seem to attract not in a linear chain but at

Figure 4.16: Energy Values for Various Particle Separations

d	Energy
1.60	1.08
1.40	1.01
1.20	0.89
1.00	0.74
.800	0.58
.750	0.54
.700	0.54
.650	0.62
.625	0.75

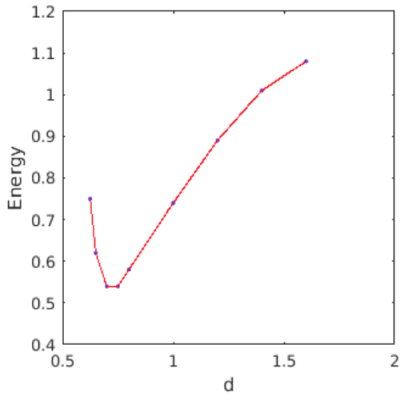

The energy for the two particle system and various values of d is computed and organized into a table. The values are also plotted to better visualize the results.

an angle to one another [33]. As is the case for a single particle, confinement plays a major role in defect structure for two particles. The extent of this confinement needs further study. In experiments done by Musevic et al. they considered a cell which was twice the diameter of the particles and the angle between the particles was nonzero [33]. In [60], Ravnik et al. consider a cell which is only ten percent larger than the cell diameter, and in this case the particles lie on the same axis. This potential confinement interaction was briefly mentioned by Araki and Tanaka [41]. In their numerical work, they consider two particles in a weak external field, which, as discussed in the previous section, is equivalent to relaxing the confining geometry. In this case, their final defect structure is completely different than what was seen previously and acknowlege that confinement may be a determining factor.

Chapter 5

Numerical Simulations using Symmetry

Numerical simulations in three-dimensional domains are computationally intensive and using symmetry to simplify the domains can greatly reduce the computational cost. Whereas two-dimensional domains can accommodate finer meshes, these domains may alter the properties of approximate solutions. For instance, if two distinct uniaxial directions cross in space, their projections onto the plane will intersect, creating a discontinuity.

In this Chapter, we will consider cross sections of some of the domains in Chapter 4 and study when the results are consistent with those found over the full three-dimensional domain. The energy expression used for the minimization is the dimensionless Landau-de Gennes energy described in (4.1). The cross sections for three types of domains are considered. First, the energy is minimized over various annular regions which correspond to the cross sections of the concentric cylinder domains of Chapter 4. In this case, we find the results to be consistent with the fully three-dimensional. Next, the minimizer corresponding to the cross section of a single particle suspended in a cylinder is computed. The behavior of the line field and β is similar to that seen in three dimensions, but the defect regions are larger. Finally, two particles in a box are considered. Since the system is not rotationally symmetric, we will only find qualitative agreement because the details of the defect structure cannot be fully described in two dimensions. Additionally, larger particle separations are needed in order to resolve the transitions of the defect regions seen in the three-dimensional case due to the larger nature of the Saturn ring defect in the cross sections.

5.1 Specifying Boundary Conditions

As in Chapter 4, we are looking for an approximate solution, $\boldsymbol{q}_h$, to the weak Euler-Lagrange equations (4.4). The boundary conditions must once again be expressed in terms of $\boldsymbol{q} = (q_0, q_1, q_2, q_3, q_4)$ where Q and $\boldsymbol{q}$ are related be expression (4.2). Two boundary conditions are used in the numerical simulations: *planar radial* and *planar vertical*. For the planar radial boundary condition, assume that

$$Q = (\boldsymbol{n}_{pr} \otimes \boldsymbol{n}_{pr} - (1/3)I) \text{ where } \boldsymbol{n}_{pr} = (x_0/|\boldsymbol{x}|, x_1/|\boldsymbol{x}|, 0) \tag{5.1}$$

and $|\boldsymbol{x}| = \sqrt{x_0^2 + x_1^2}$. In terms of the components of Q, this implies

$$q_0 = \frac{x_0^2}{|\boldsymbol{x}|^2} - \frac{1}{3}, q_1 = \frac{x_1^2}{|\boldsymbol{x}|^2} - \frac{1}{3}, q_2 = \frac{x_0 x_1}{|\boldsymbol{x}|^2}, q_3 = 0 = q_4. \tag{5.2}$$

For planar vertical boundary conditions,

$$Q = (\boldsymbol{n}_{pv} \otimes \boldsymbol{n}_{pv} - (1/3)I) \text{ where } \boldsymbol{n}_{pv} = (0, 1, 0) \tag{5.3}$$

and so

$$q_0 = -\frac{1}{3}, q_2 = \frac{2}{3}, \text{ and } q_2 = 0 = q_3 = q_4 \tag{5.4}$$

5.2 Annulus as a Cross Section

We begin by considering an annular domains with outer radius L_0 and inner radius ρL_0. On the domain boundaries, homeotropic Dirichlet boundary conditions are defined as in (5.2). Let $\rho = .8, .5, .3, .2, .15, .1, .05, .02, 0$ so that the annular regions are exactly the cross sections of the concentric cylinder domains considered in Chapter 4. Note that even though the domains are two-dimensional, the use of the three-dimensional Landau-de Gennes model, (4.1), allows for biaxiality to develop. Because of this, the cross sections will exactly reflect the behavior seen in the concentric cylinder domains.

As a representative example of the mesh used in each case, we show the mesh for $\rho = .2$ in Figure 5.1 and its details are summarized into Table 5.1.

Table 5.1: Mesh Details for Annulus with $\rho = .2$

Max h	Min h	Average h	Number of Cells
$7.45e-02$	$1.07e-02$	$4.07e-02$	$7.22e+03$

Figure 5.1: Mesh Details for Annulus with $\rho = .2$

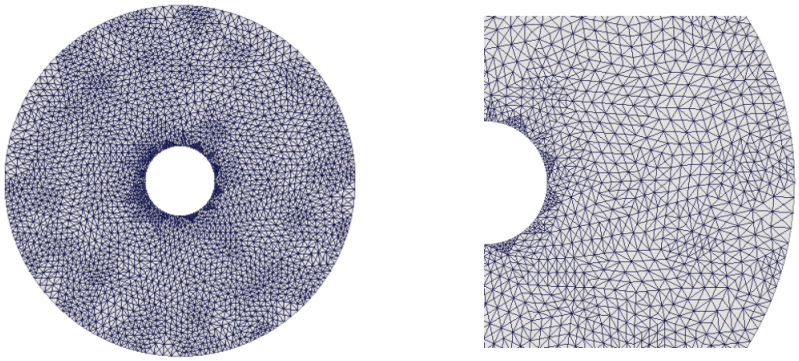

On the left, the mesh for the entire domain is shown. The right shows a zoomed in portion in order to see the mesh details around the inner boundary.

Using FEniCS, degree one Lagrange elements are used to find an approximate solution, $\boldsymbol{q}_h$, of the weak Euler-Lagrange equations (4.4) on each domain. We calculate β_h over the mesh and the results are plotted in Figure 5.2.

The biaxiality parameter β_h over these cross section reflects the exact behavior seen in the three-dimensional concentric cylinder domain. As ρ decreases, the biaxial region increases as does the maximal value of β_h over the domain, until it reaches a maximal value of one. As shown in the second row of Figure 5.2, this biaxial region then develops an interior region in which β_h is no longer maximal. Decreasing ρ further results in this lower β-valued region attaining a value of zero, which corresponds to the presence of the escape solution. Clearly, in this case the liquid crystal behavior in the entire domain can be captured from minimizing the Landau-de Gennes energy over a cross section.

Since there is an exact agreement with the three-dimensional domain and there is less numerical error introduced when interpolating over a two-dimensional domain, it is of interest to compare the results of the Landau-de Gennes minimization with the planar radial line field. The planar radial line field has an associated $Q_r = h(r)(\boldsymbol{n}_r \otimes \boldsymbol{n}_r - (1/3)I$ where $\boldsymbol{n}_r = (x/\sqrt{x^2+y^2}, y/\sqrt{x^2+y^2}, 0)$ and $h(r)$ is the solution to the integral energy expression:

$$I[h] = 2\pi K \int_0^R \left[\frac{1}{3}h'^2 - \frac{hh'}{3r} + (\frac{1}{r^2} - \frac{2}{3})h^2 + \frac{2\mathcal{B}}{27}h^3 + \frac{\mathcal{C}}{9}h^4\right] \; r \; dr \tag{5.5}$$

whose derivation can be found in Section A.3 of the Appendix. For each ρ, the energy value is computed on the mesh for the approximate solution. The radial solution is also interpolated onto this mesh and its energy per unit area is calculated. Mesh refinements are done until the energy repeats in value. The final mesh contains between $10,000 - 525,000$

Figure 5.2: β_h Plots for Various Annular Domains

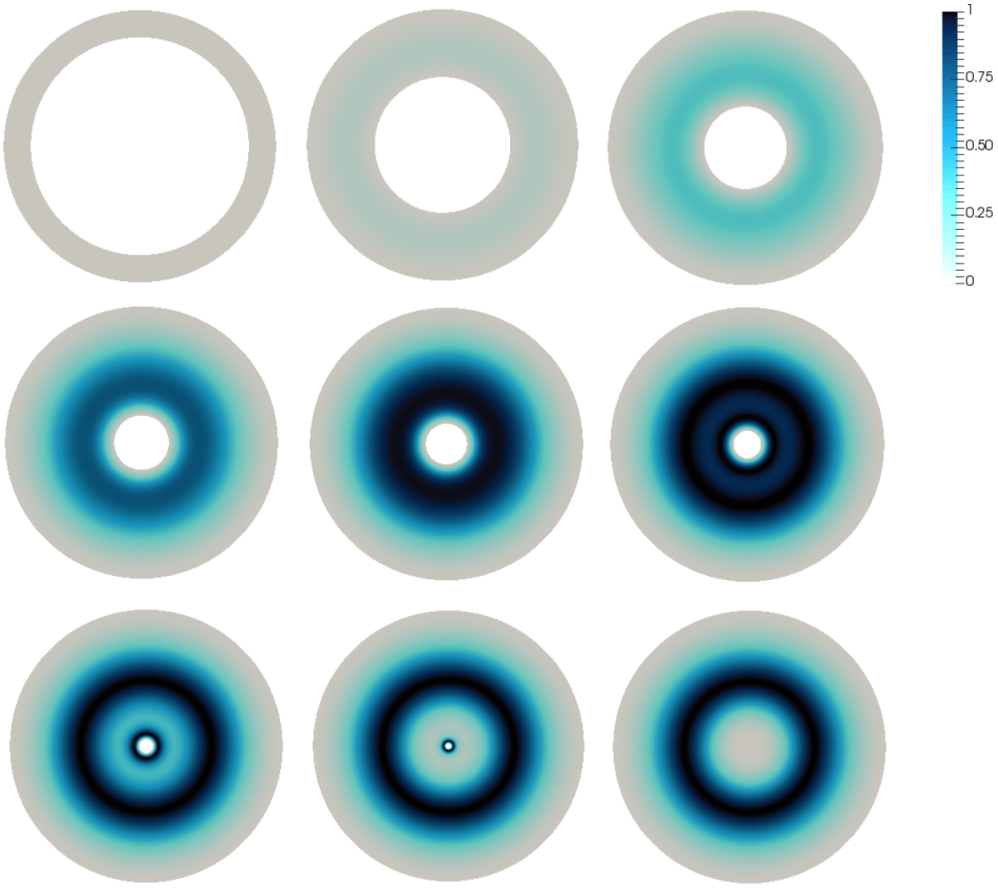

β_h, the biaxiality parameter, is plotted over the annulus for a range of values ρ. On the top row, left to right $\rho = .8, .5, .3$, middle row $\rho = .2, .15, 1$ and bottom row $\rho = .05, .02, 0$

elements depending on the size of the domain. The energy values on the final meshes are organized into Table 5.2.

Notice that for $\rho = .8$, it appears as though the energy values are equal. As stated, every domain, regardless the value of ρ, has some degree of biaxiality. Since the domain is very thin and the boundary conditions are exactly given by the radial line field, β_h remains small. If we consider more decimal places, the energy per unit area of the approximate solution is 1.076 while the energy for the planar radial solutions is 1.082, showing that the approximate solution continues to give a lower energy.

For every ρ, the minimizer of the Landau-de Gennes model has a lower energy than

Table 5.2: Energies per Unit Area for Varying ρ

Number of Cells	Computed Minimizer	Radial Hedgehog
.8	1.08	1.08
.5	1.41	1.46
.3	1.67	1.78
.2	1.79	1.96
.15	1.84	2.04
.1	1.88	2.11
.05	1.90	2.16
.02	1.91	2.18
0	0.91	1.03

the radial hedgehog. Notice that this is inconsistent with the results using the Oseen-Frank energy presented in [20]. As discussed in Chapters 3 and 4, they predict that for $\rho \geq e^{-\pi} \approx .0432$, the minimizing configuration is the planar radial solution. Our energy calculations show that there is no radius in which the planar radial solution will have a lower energy and further proves that the planar radial solution is an artifact of using a vector field dependent model and not a true minimizing configuration in such a domain.

Consider $\rho = 0$, where the domain corresponds to a unit disc. It has been hypothesized for nearly fifty years that the minimizer for this domain is given by a configuration that is allowed to relax out of the plane. Cladis and Kleman find, using the Oseen-Frank energy, that such a configuration occurs for radii larger than a few molecular lengths [7]. We do not include a detailed discussion here, but when the radius of the solid disc is allowed to vary, the escape solution is always found to be the minimizing configuration. In radii where this does not appear to be the case, such as for very small radii, further refinement of the domain, once again, resulted in an escape solution.

5.3 Single Particle

For the three-dimensional cross section, let us consider a box of sidelengths $4L_0$ with a circle of radius $.5L_0$ removed from the center. As done for the three-dimensional case, homeotropic Dirichlet boundary conditions are defined on the surface of the particle and everywhere vertical Dirichlet boundary conditions are defined on the boundary of the box. Using degree one Lagrange elements, the energy is minimized using FEniCS. The number of cells as well as the maximum, minimum, and average cell diameter, h, of this mesh are organized into Table 5.3. As in the three-dimensional domain, the mesh is further refined

around the particle surface so that the defect regions are properly resolved. A plot of the mesh is not included since the mesh is too dense to see the details.

Table 5.3: Mesh Details Single Particle in Two Dimensions

Max h	Min h	Average h	Number of Triangles
$5.26e-02$	$3.28e-03$	$1.61e-02$	$1.63e+05$

Notice that the number of cells used is approximatedly ten times fewer than in the three-dimensional domain. While this does not seem like a vast simplification, we must keep in mind that the mesh is now composed of two-dimensional triangles as opposed to three-dimensional tetrahedron. This results in a considerable reduction in computing time and allows for a much finer mesh everywhere in the domain and ultimately a higher level of accuracy. Since a very fine mesh is used, $3,000$ elements of the line field are plotted in Figure 5.3. Two ellipses denote the defect regions and the behavior of the surrounding line field implies that these two defects are of order $-1/2$.

Figure 5.3: Line Field Plots for Single Particle Cross Section

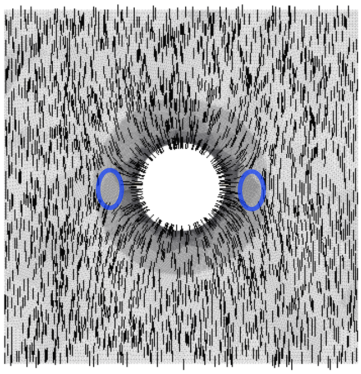

The ellipses along the equator of the particle denote defect regions. Around these defects, the line field clearly implies that the defects are both of order $-1/2$. Note that $3,000$ elements of the line field are shown because of the high density of elements in the mesh.

The location of the defects is further confirmed by the behavior of the biaxiality parameter. For comparison with the results in the previous chapter, β_h as well as r_h and s_h are calculated from the approximate solution. $\boldsymbol{q}_h$, and plotted over the domain in Figure 5.4.

In terms of β_h, r_h, and s_h, the behavior of the defect region is qualitatively equivalent to minimizing this energy expression over the entire three-dimensional domain, but we notice that the value at which $r_h = s_h$ has increase from .35 to a value of .4. Away from the

Figure 5.4: β_h, s_h, and r_h Plots for Single Particle Cross Section

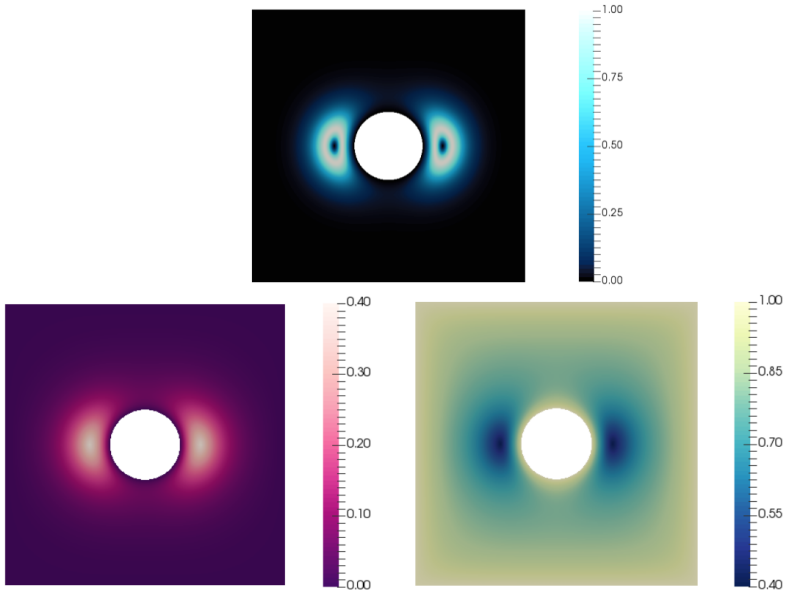

β_h, the biaxiality parameter, is plotted in the first row. In the second row the plot of r_h is on the left and plot of s_h on the right.

defects, the line field, β_h, s_h, and r_h agree with the three-dimensional results. Through careful comparison with the cross sections plotted in Chapter 4, we see that the defect region is larger in this two-dimensional cross-sectional domain. The large defect region is reflected in the line field as well.

It is important to understand why these results diverge slightly from the minimization done in the three-dimensional domain. It is due to the nature of the behavior of semi-rigid elongated molecules in these two types of domains. In three dimension, the molecules do not have to lie completely in a single plane and can relax into different directions while retaining their uniaxial nature. In two dimensions, forcing the molecules to lie on a plane suppressed their ability to come out of the plane and causes the defect regions to be larger.

5.4 Two Particles

For the two particle system considered in Chapter 4, it is clear that a two-dimensional simplification will not illustrate the behavior of the full system, but it can give qualitative agreement. We consider a box of sidelengths $5L_0$ with two particles of radius $.3L_0$ removed. These particles will be aligned along the x-axis and separated by a distance d, measured

from the center of the particles. The particles have hometropic Dirichlet planar boundary conditions as defined by (5.2) and the boundaries of the box have planar vertical Dirichlet boundaries conditions as in (5.4). For several values of d, the energy is minimized using degree one Lagrange element over the domain and the energy values are calculated.

Before presenting the results, we give the mesh details for $d = 1.2L_0$ since all the meshes are generated in a similar fashion. As was done in previous computations over particle domains, the mesh is further refined around the surface of the particles. The maximum, minimum, and average cell diameter, h, as well as the number of cells in the mesh are organized into Table 5.4. An image of the mesh is not included since it is so fine that the mesh details are difficult to see.

Table 5.4: Mesh Details Two Particles in Two Dimensions

Max h	Min h	Average h	Number of Triangles
$4.93e-02$	$6.93e-03$	$1.82e-02$	$2.70e+05$

For five different values of d, the approximated energy minimizer, $\boldsymbol{q}_h$, is computed using FEniCS, from which Q_h is found and β_h is calculated. The plots of β_h over each domain are shown in Figure 5.5.

Similar to the results in Chapters 3 and 4, the particles present separate Saturn ring defects for a large enough separation. In order to resolve to separate Saturn ring defects, a larger initial separation, than that needed in the three-dimensional domain, was needed due to the the larger size of the defect regions. The initial separation considered is $d = 2.4L_0$, which is 1/3 larger than the separation needed in Chapter 4. Analogous to the three-dimensional domain, as the particles are brought closer together, the defect region between them fuzes. Further decreasing d results in the region splitting at the center as shown for $d = .8L_0$ in Figure 5.5. This corresponds to the formation of the third ring seen in the entangled hyperbolic defect. In terms of the biaxiality parameter the agreement is again qualitative, but the restriction to the plane causes larger defect regions and therefore the defect transitions occured at much larger separations. For $d = 1.6L_0, 1.2L_0$, these separations were considered in the previous Chapter as well and the difference in the defect region is clear.

We also study whether energy of the system reflects the fact that there is first an attraction between the two particles and later a repulsion if d becomes too small. For various values of d, the energy is found and organized into a table shown in Figure 5.6.

Figure 5.5: β_h Plots for Various Circle Separations

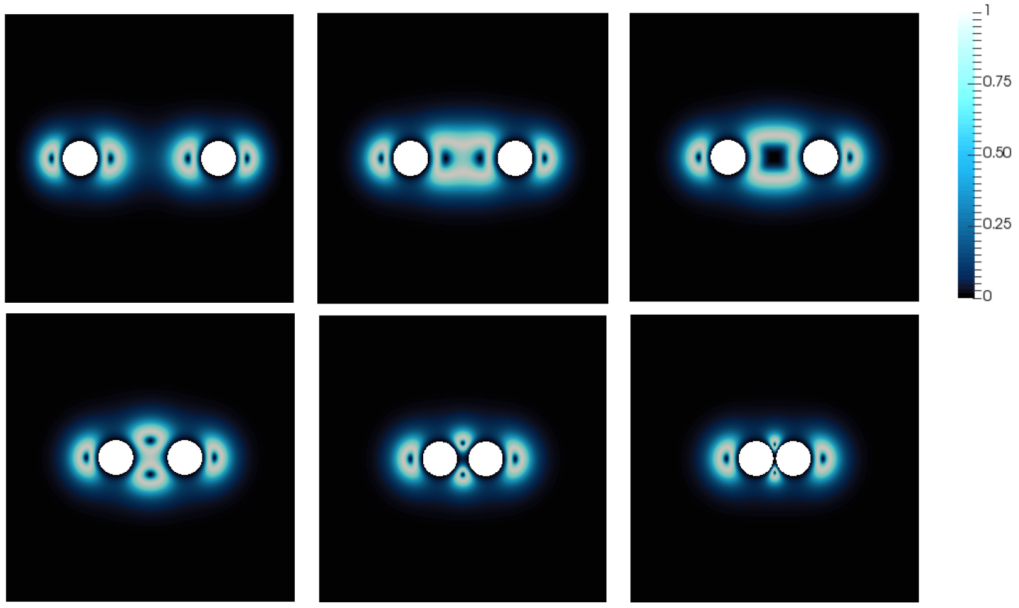

On the first row from left to right, $d = 2.4, 1.8, 1.6$. *Second row left to right* $d = 1.2, .8, .65$, *where* d *is measured in units of* L_0.

Figure 5.6: Energy Values for Various Circle Separations

d	Energy
2.40	3.38
2.00	3.26
1.60	3.08
1.40	2.96
1.20	2.82
1.00	2.68
.80	2.63
.75	2.69
.70	2.84
.65	3.24

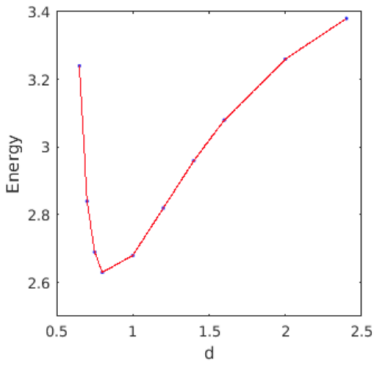

On the left, the energy of the system is found for various values of d. On the right, a plot is shown of these results.

Similar to the results in Chapters 3 and 4, the energy first decreases with decreasing d, and then after $d = .8L_0$, further reductions result in an increase in energy implying a repulsive force between the particles. In the previous Chapter, this minimum occurred

for $d = .7 - .75L_0$, which is in close agreement despite the fact that the defect structure was much larger in this cross-sectional domain and a large initial separation was needed to resolve two separate Saturn ring defects. Of course, the full defect structure will not be captured with this simplification, but there is a clear qualitative agreement in both the behavior of the energy and the defect structure.

When using symmetry to reduce computational cost in a liquid crystal domain, it cannot be assumed that the result is in exact agreement with the full three-dimensional domain. Forcing the liquid crystal molecules to lie in a plane can give rise to larger defect structures, as we have seen in the domains with particle interactions. Therefore, many quantities calculated in the literature such as particle separation or Saturn ring size and radius will not be accurate if done in a cross-sectional domain. However, if one is looking for a qualitative agreement only, minimization over a cross section can be a powerful and less computationally expensive tool.

Chapter 6

Conclusion

In Chapter 2, we introduced the Oseen-Frank model, and used it to present some of the subtle issues that must be addressed when modeling liquid crystal behavior. The inability to describe biaxiality and its infinite energy for +1 ordered line defects illustrated the models deficiency and motivated the introduction of the Landau-de Gennes energy, in which molecular alignment is now described by a symmetric, traceless tensor Q. We proved that under certain assumptions, the two models are equivalent and the issue of orientability was critical. When orientability of the line field is not required, more minimizing configurations can be described using the tensor Q, a fact which further supported our choice of model. We ended the chapter by proving the existence of minimizers for the Landau-de Gennes energy and introduced the dimensionless form of the energy. This dimensionless form was used for all the numerical calculations presented in this thesis.

For simulations done using both the two-by-two and three-by-three forms of Q, the method of manufactured solutions was used to establish a rigorous foundation for the numerical computations that followed. This is an essential part of the work in this thesis and a point of distinction from previous numerical results since it is the first time such methods were used to validate numerical computing involving the Landau-de Gennes energy expression. In Chapter 3, the manufactured solution was assumed to be the planar radial configuration and the domain considered was an annulus. Our convergence study with degree one and two Lagrange elements provided confidence that the remainder of the computations in the chapter were accurate. In Chapter 4, the planar radial configuration was again chosen as the manufactured solution, but its description was three-dimensional in this case and the domain was the region confined between two concentric cylinder of finite height. The minimization was done using degree one and two Lagrange elements and the

orders of convergence once again provided the reader with confidence that our numerical computations were accurate.

In Chapter 3, our results showed both agreement and departure from previous results. The domains with particle interactions had minimizing configurations which were consistent with those found by Tasinkevych et al. in [50]. However, for annular domains, we showed that the restriction of Q to a two-by-two matrix resulted in a single possible solution structure. This was inconsistent with the predicted configurations described by Bethuel et al, but not unexpected since our assumptions forced Q to be uniaxial and lie in the plane.

A consequential contribution was presented for disc domains. For the disc of radius $11L_0$, we proved that the minimizing configuration is the radial hedgehog. This contradicts the minimizers found by Sonnet et al. in 1995, and Mkaddem and Gartland in 2000, which predict a split core defect for this radius. Through convergence studies and comparing the energy of the hedgehog and split core configurations we were able to conclude that the split core defect is an artifact of improper mesh refinement [17], [18]. This result emphasizes the need to compare experimental data with those found through numerical minimization of the energy expression. Before concluding that a new defect structure may have been found, the mesh should be refined further to ensure that the configuration is not instead due to a numerical error.

In Chapter 4, we used a three-by-three Q tensor and minimized the energy over three-dimensional domains in order to find minimizing configurations and defect core structures not previously numerically verified. In the droplet domain with homeotropic alignment, we proved through minimization of the energy and comparison with the uniaxial hedgehog, an exact solution to the Landau-de Gennes Euler-Lagrange equations, that a droplet with biaxial core has a smaller energy. Our numerical results verify the conclusions by Schopohl and Sluckin, and later Penzenstadler and Trebin, that the droplet with such boundary conditions always has a biaxial core [19], [65]. For two particles in a cylindrical domain, we resolved the entangled hyperbolic defect and studied the formation of this defect configuration. The particle separation where this defect structure occurs in our numerical calculations matched the predictions of Guzman et al. and the experimental evidence presented by Musevic et. al. [48], [33].

One of the most important results of this thesis arose in the concentric cylinder domains. We found three minimizing configurations which transform continuously to one another as we vary ρ, the ratio of the inner to the outer radius. Every configuration has some level of biaxiality, which is in contrast to the purely unaxial configuration predicted by Bethuel et al. using the Oseen-Frank energy expression, and more accurately reflects the behavior seen

in experiments [20]. This result illuminates the fact that the restriction of vector-based models to purely uniaxial configurations can cause a deviation from physically realistic configurations. Another significant development involved the single particle domain, our numerical results confirmed for the first time that the core of a Saturn ring defect is uniaxial with negative scalar order parameter, as predicted by Schopohl and Sluckin [19].

In Chapter 5, we used symmetry to show that minimization over a cross section can always guarantee qualitative agreement, but the results deviate slightly when particle interaction is present. For the cross sections of the concentric cylinder domains of Chapter 4, we showed that the minimization gave analogous results. For the domains with particle interactions, the restriction of the liquid crystal to the plane gave larger defect structures than those seen in the three-dimensional domains. These computations illustrate that many previous work in which symmetry is used to simplify the model can only, at best, give a qualitative understanding of the three-dimensional behavior when particle interaction is involved.

From a numerically rigorous perspective, we studied the Landau-de Gennes energy and illustrated some deficiencies with previous numerical and theoretical results in nematic liquid crystal domains. Our hope is that this work will serve as an example for future numerical computations involving the Landau-de Gennes energy expression, and subsequent authors will include proper convergence studies before presenting their resulting energy minimizing configurations.

References

[1] Ian W Hamley. *Introduction to soft matter: synthetic and biological self-assembling materials*. John Wiley & Sons, 2013.

[2] Epifanio G Virga. *Variational theories for liquid crystals*, volume 8. CRC Press, 1995.

[3] Birendra Bahadur. *Liquid crystals: applications and uses*, volume 1. World Scientific, 1990.

[4] Otto Lehmann. *Flüssige Kristalle*. Urban u. Schwarzenberg, 1904.

[5] MG Friedel. *Les Etats Mesamorphes de la matiere*. 1922.

[6] LJ Yu and Alfred Saupe. Observation of a biaxial nematic phase in potassium laurate-1-decanol-water mixtures. *Physical Review Letters*, 45(12):1000, 1980.

[7] PE Cladis and M Kleman. Non-singular disclinations of strength s=+ 1 in nematics. *Journal de Physique*, 33(5-6):591–598, 1972.

[8] CE Williams, PE Cladis, and M Kleman. Screw disclinations in nematic samples with cylindrical symmetry. *Molecular Crystals and Liquid Crystals*, 21(3-4):355–373, 1973.

[9] G Toulouse and M Kléman. Principles of a classification of defects in ordered media. *Journal de Physique Lettres*, 37(6):149–151, 1976.

[10] GE Volovik and VP Mineev. Line and point singularities in superfluid he 3. *JETP Letters*, 24(11), 1976.

[11] W. F. Brinkman and P. E. Cladis. Defects in liquid crystals. *Physics Today*, 35:48–56, May 1982.

[12] Frederick C Frank. Liquid crystals on the theory of liquid crystals. In *Crystals That Flow: Classic Papers from the History of Liquid Crystals*, pages 389–399. CRC Press, 2004.

[13] Wilhelm Maier and Alfred Saupe. Eine einfache molekulare theorie des nematischen kristallinflüssigen zustandes. *Zeitschrift für Naturforschung A*, 13(7):564–566, 1958.

[14] John M Ball and Apala Majumdar. Nematic liquid crystals: from maier-saupe to a continuum theory. *Molecular Crystals and Liquid Crystals*, 525(1):1–11, 2010.

[15] William F Brinkman and Patricia E Cladis. Defects in liquid crystals. *Physics Today*, 35(5):48–54, 1982.

[16] Samo Kralj, Epifanio G Virga, and Slobodan Žumer. Biaxial torus around nematic point defects. *Physical Review E*, 60(2):1858, 1999.

[17] S Mkaddem and EC Gartland Jr. Fine structure of defects in radial nematic droplets. *Physical Review E*, 62(5):6694, 2000.

[18] A Sonnet, A Kilian, and S Hess. Alignment tensor versus director: Description of defects in nematic liquid crystals. *Physical Review E*, 52(1):718, 1995.

[19] N Schopohl and TJ Sluckin. Defect core structure in nematic liquid crystals. *Physical Review Letters*, 59(22):2582, 1987.

[20] F Bethuel, Haim Brezis, BD Coleman, and F Hélein. Bifurcation analysis of minimizing harmonic maps describing the equilibrium of nematic phases between cylinders. *Archive for Rational Mechanics and Analysis*, 118(2):149–168, 1992.

[21] Paolo Biscari and Epifanio G Virga. Local stability of biaxial nematic phases between two cylinders. *International Journal of Non-Linear Mechanics*, 32(2):337–351, 1997.

[22] Oleg Lavrentovich. Liquid crystal between two crossed polarizers. [Online; accessed April, 2016].

[23] Peter J Collings and Michael Hird. *Introduction to liquid crystals: chemistry and physics*. CRC Press, 1997.

[24] Douglas Hugh Everett and DH Everett. *Basic principles of colloid science*, volume 144. Royal Society of Chemistry London, 1988.

[25] CW Oseen. The theory of liquid crystals. *Transactions of the Faraday Society*, 29(140):883–899, 1933.

[26] Robert Hardt, David Kinderlehrer, and Fang-Hua Lin. Existence and partial regularity of static liquid crystal configurations. *Communications in Mathematical Physics*, 105(4):547–570, 1986.

[27] JL Ericksen. Constitutive theory for some constrained elastic crystals. *International Journal of Solids and Structures*, 22(9):951–964, 1986.

[28] Fang Hua Lin. On nematic liquid crystals with variable degree of orientation. *Communications on Pure and Applied Mathematics*, 44(4):453–468, 1991.

[29] Timothy J Sluckin, David A Dunmur, and Horst Stegemeyer. *Crystals that flow: Classic papers from the history of liquid crystals*. Taylor & Francis London, 2004.

[30] Timothy A Davis and Eugene C Gartland Jr. Finite element analysis of the landau–de gennes minimization problem for liquid crystals. *SIAM Journal on Numerical Analysis*, 35(1):336–362, 1998.

[31] Yuedong Gu and Nicholas L Abbott. Observation of saturn-ring defects around solid microspheres in nematic liquid crystals. *Physical Review Letters*, 85(22):4719, 2000.

[32] JC Loudet, Ph Barois, P Auroy, P Keller, H Richard, and P Poulin. Colloidal structures from bulk demixing in liquid crystals. *Langmuir*, 20(26):11336–11347, 2004.

[33] Igor Muševič, Miha Škarabot, Uroš Tkalec, Miha Ravnik, and Slobodan Žumer. Two-dimensional nematic colloidal crystals self-assembled by topological defects. *Science*, 313(5789):954–958, 2006.

[34] Igor Muševič and Miha Škarabot. Self-assembly of nematic colloids. *Soft Matter*, 4(2):195–199, 2008.

[35] U Ognysta, A Nych, V Nazarenko, I Muševič, M Škarabot, M Ravnik, S Žumer, I Poberaj, and D Babič. 2d interactions and binary crystals of dipolar and quadrupolar nematic colloids. *Physical Review Letters*, 100(21):217803, 2008.

[36] Ph Poulin, V Cabuil, and DA Weitz. Direct measurement of colloidal forces in an anisotropic solvent. *Physical Review Letters*, 79(24):4862, 1997.

[37] Holger Stark. Director field configurations around a spherical particle in a nematic liquid crystal. *The European Physical Journal B-Condensed Matter and Complex Systems*, 10(2):311–321, 1999.

[38] Sylvain Grollau, NL Abbott, and JJ de Pablo. Spherical particle immersed in a nematic liquid crystal: Effects of confinement on the director field configurations. *Physical Review E*, 67(1):011702, 2003.

[39] RW Ruhwandl and EM Terentjev. Monte carlo simulation of topological defects in the nematic liquid crystal matrix around a spherical colloid particle. *Physical Review E*, 56(5):5561, 1997.

[40] Denis Andrienko, Guido Germano, and Michael P Allen. Computer simulation of topological defects around a colloidal particle or droplet dispersed in a nematic host. *Physical Review E*, 63(4):041701, 2001.

[41] Takeaki Araki and Hajime Tanaka. Colloidal aggregation in a nematic liquid crystal: topological arrest of particles by a single-stroke disclination line. *Physical Review Letters*, 97(12):127801, 2006.

[42] Iztok Bajc, Frédéric Hecht, and Slobodan Žumer. A mesh adaptivity scheme on the landau–de gennes functional minimization case in 3d, and its driving efficiency. *Journal of Computational Physics*, 321:981–996, 2016.

[43] Jun-ichi Fukuda, Holger Stark, Makoto Yoneya, and Hiroshi Yokoyama. Interaction between two spherical particles in a nematic liquid crystal. *Physical Review E*, 69(4):041706, 2004.

[44] J Fukuda and H Yokoyama. Director configuration and dynamics of a nematic liquid crystal around a two-dimensional spherical particle: Numerical analysis using adaptive grids. *The European Physical Journal E*, 4(3):389–396, 2001.

[45] Jun-ichi Fukuda, Makoto Yoneya, and Hiroshi Yokoyama. Director configuration of a nematic liquid crystal around a spherical particle: Numerical analysis using adaptive mesh refinement. *Molecular Crystals and Liquid Crystals*, 413(1):221–229, 2004.

[46] Sylvain Grollau, Evelina B Kim, Orlando Guzman, Nicholas L Abbott, and Juan José de Pablo. Monte carlo simulations and dynamic field theory for suspended particles in liquid crystalline systems. *The Journal of Chemical Physics*, 119(4):2444–2455, 2003.

[47] BI Lev, SB Chernyshuk, PM Tomchuk, and H Yokoyama. Symmetry breaking and interaction of colloidal particles in nematic liquid crystals. *Physical Review E*, 65(2):021709, 2002.

[48] O Guzmán, EB Kim, S Grollau, NL Abbott, and JJ de Pablo. Defect structure around two colloids in a liquid crystal. *Physical Review Letters*, 91(23):235507, 2003.

[49] Evelina B Kim, Orlando Guzmán, Sylvain Grollau, Nicholas L Abbott, and Juan J de Pablo. Interactions between spherical colloids mediated by a liquid crystal: A molecular simulation and mesoscale study. *The Journal of Chemical Physics*, 121(4):1949–1961, 2004.

[50] M Tasinkevych, NM Silvestre, P Patrício, and MM Telo Da Gama. Colloidal interactions in two-dimensional nematics. *The European Physical Journal E*, 9(4):341–347, 2002.

[51] SV Burylov. Equilibrium configuration of a nematic liquid crystal confined to a cylindrical cavity. *Journal of Experimental and Theoretical Physics*, 85(5):873–886, 1997.

[52] Samo Kralj and Slobodan Žumer. Saddle-splay elasticity of nematic structures confined to a cylindrical capillary. *Physical Review E*, 51(1):366, 1995.

[53] Nigel J Mottram and Chris Newton. Introduction to q-tensor theory. *University of Strathclyde, Department of Mathematics research report*, 2004:10, 2004.

[54] MJ Freiser. Ordered states of a nematic liquid. *Physical Review Letters*, 24(19):1041, 1970.

[55] Apala Majumdar and Arghir Zarnescu. Landau-de gennes theory of nematic liquid crystals: the oseen-frank limit and beyond. *Archive for Rational Mechanics and Analysis*, 196(1):227–280, 2010.

[56] Paolo Biscari, Maria Carme Calderer, and Eugene M Terentjev. Landau–de gennes theory of isotropic-nematic-smectic liquid crystal transitions. *Physical Review E*, 75(5):051707, 2007.

[57] John M Ball and Arghir Zarnescu. Orientability and energy minimization in liquid crystal models. *Archive for Rational Mechanics and Analysis*, 202(2):493–535, 2011.

[58] Jerald L Ericksen. Liquid crystals with variable degree of orientation. *Archive for Rational Mechanics and Analysis*, 113(2):97–120, 1991.

[59] WD Evans. Partial differential equations, 1988.

[60] M Ravnik, M Škarabot, S Žumer, U Tkalec, I Poberaj, D Babič, N Osterman, and I Muševič. Entangled nematic colloidal dimers and wires. *Physical Review Letters*, 99(24):247801, 2007.

[61] Patrick J Roache. Code verification by the method of manufactured solutions. *Transactions-American Society of Mechanical Engineers Journal of Fluids Engineering*, 124(1):4–10, 2002.

[62] Apala Majumdar. The radial-hedgehog solution in landau–de gennes' theory for nematic liquid crystals. *European Journal of Applied Mathematics*, 23(01):61–97, 2012.

[63] Francois Alouges and Bernard D Coleman. Numerical bifurcation of equilibria of nematic crystals between non-co-axial cylinders. *Mathematical Models and Methods in Applied Sciences*, 11(03):459–473, 2001.

[64] GP Crawford, David W Allender, J William Doane, M Vilfan, and I Vilfan. Finite molecular anchoring in the escaped-radial nematic configuration: A nmr 2 study. *Physical Review A*, 44(4):2570, 1991.

[65] E Penzenstadler and H-R Trebin. Fine structure of point defects and soliton decay in nematic liquid crystals. *Journal de Physique*, 50(9):1027–1040, 1989.

[66] Stan Alama, Lia Bronsard, and Bernardo Galvao-Sousa. Weak anchoring for a two-dimensional liquid crystal. *arXiv preprint arXiv:1405.3024*, 2014.

[67] Miha Ravnik and Slobodan Žumer. Landau–de gennes modelling of nematic liquid crystal colloids. *Liquid Crystals*, 36(10-11):1201–1214, 2009.

[68] Jun-ichi Fukuda, Makoto Yoneya, and Hiroshi Yokoyama. Defect structure of a nematic liquid crystal around a spherical particle: Adaptive mesh refinement approach. *Physical Review E*, 65(4):041709, 2002.

[69] C Völtz, Y Maeda, Y Tabe, and H Yokoyama. Director-configurational transitions around microbubbles of hydrostatically regulated size in liquid crystals. *Physical Review Letters*, 97(22):227801, 2006.

[70] Holger Stark. Saturn-ring defects around microspheres suspended in nematic liquid crystals: an analogy between confined geometries and magnetic fields. *Physical Review E*, 66(3):032701, 2002.

Appendix A

Calculations

A.1 Derivation of $h(r)$ in Polar Coordinates

In this case, we assume Q is the two-by-two tensor defined in (3.1) and $Q = h(\boldsymbol{n}_r \otimes \boldsymbol{n}_r - (1/2)I)$ where $\boldsymbol{n}_r = e_r$ is the planar radial basis vector and h is dependent only on r, the radial distance from the origin. We want to express the Landau-de Gennes energy in terms of h, and therefore need to expand $\frac{1}{2}|\nabla Q|^2 - \frac{1}{2}\text{tr } Q^2 + \frac{\mathcal{C}}{4}(\text{tr } Q^2)^2$. We begin by finding ∇Q in terms of $\boldsymbol{n}_r$ and h:

$$\begin{aligned} \nabla Q = \nabla[h(e_r \otimes e_r - \frac{1}{2}I)] &= (e_r \otimes e_r - \frac{1}{2}I) \otimes \nabla h + h\nabla(e_r \otimes e_r) \\ &= e_r \otimes e_r \otimes \nabla h - \frac{1}{2}I \otimes \nabla h + h\nabla(e_r \otimes e_r) \end{aligned} \tag{A.1}$$

Using the fact that the Frobenius inner product is commutative $|\nabla Q|^2$ can be expressed in the following way:

$$\begin{aligned} |\nabla Q|^2 &= \nabla Q : \nabla Q \\ &= (e_r \otimes e_r \otimes \nabla h : e_r \otimes e_r \otimes \nabla h) - (e_r \otimes e_r \otimes \nabla h : I \otimes \nabla h) \\ &+ (2e_r \otimes e_r \otimes \nabla h : h\nabla(e_r \otimes e_r)) + \frac{1}{4}(I \otimes \nabla h : I \otimes \nabla h) \\ &- (I \otimes \nabla h : h\nabla(e_r \otimes e_r)) + (h\nabla(e_r \otimes e_r) : h\nabla(e_r \otimes e_r)) \end{aligned} \tag{A.2}$$

For readability, we will expand each of the six terms separately. Before doing so, it will be useful to rewrite $\nabla(e_r \otimes e_r)$:

$$\begin{aligned} \nabla(e_r \otimes e_r) &= \left(e_r \frac{\partial}{\partial r} + \frac{1}{r} e_\theta \frac{\partial}{\partial \theta}\right) \otimes (e_r \otimes e_r) \\ &= e_r \otimes \left(\frac{\partial}{\partial r} e_r \otimes e_r + e_r \otimes \frac{\partial}{\partial r} e_r\right) + \frac{1}{r} e_\theta \otimes \left(\frac{\partial}{\partial \theta} e_r \otimes e_r + e_r \otimes \frac{\partial}{\partial \theta} e_r\right) \end{aligned}$$

$$= \frac{1}{r}(e_\theta \otimes e_\theta \otimes e_r + e_\theta \otimes e_r \otimes e_\theta)$$

Expanding the six terms of $|\nabla Q|^2$ gives:

$$\begin{aligned} e_r \otimes e_r \otimes \nabla h : e_r \otimes e_r \otimes \nabla h &= |e_r|^2 |e_r|^2 |\nabla h|^2 \\ &= |\nabla h|^2 \end{aligned}$$

$$\begin{aligned} -e_r \otimes e_r \otimes \nabla h : I \otimes \nabla h &= -(e_r)_i (e_r)_j \nabla h_k \delta_{ij} \nabla h_k \\ &= -|\nabla h|^2 \end{aligned}$$

$$\begin{aligned} 2e_r \otimes e_r \otimes \nabla h : h\nabla(e_r \otimes e_r) &= 2e_r \otimes e_r \otimes \nabla h : \frac{h}{r}(e_\theta \otimes e_\theta \otimes e_r + e_\theta \otimes e_r \otimes e_\theta) \\ &= 2\frac{h}{r}[(e_r)_i (e_r)_j \nabla h_k (e_\theta)_i (e_\theta)_j (e_r)_k + (e_r)_i (e_r)_j \nabla h_k (e_\theta)_i (e_r)_j (e_\theta)_k] \\ &= 0 \end{aligned}$$

$$\begin{aligned} \frac{1}{4} I \otimes \nabla h : I \otimes \nabla h &= \frac{1}{4} \delta_{ij} \nabla h_k \delta_{ij} \nabla h_k \\ &= \frac{1}{2} |\nabla h|^2 \end{aligned}$$

$$\begin{aligned} -I \otimes \nabla h : h\nabla(e_r \otimes e_r) &= -I \otimes \nabla h : \frac{h}{r}(e_\theta \otimes e_\theta \otimes e_r + e_\theta \otimes e_r \otimes e_\theta) \\ &= -\frac{h}{r} \delta_{ij} \nabla h_k (e_\theta)_i (e_\theta)_j (e_r)_k - \frac{h}{r} \delta_{ij} \nabla h_k (e_\theta)_i (e_r)_j (e_\theta)_k \\ &= \frac{-h}{r} \nabla h \cdot e_r \end{aligned}$$

$$\begin{aligned} h\nabla(e_r \otimes e_r) : h\nabla(e_r \otimes e_r) &= \frac{h^2}{r^2}(e_\theta \otimes e_\theta \otimes e_r + e_\theta \otimes e_r \otimes e_\theta) : (e_\theta \otimes e_\theta \otimes e_r + e_\theta \otimes e_r \otimes e_\theta) \\ &= \frac{h^2}{r^2}(|e_\theta|^2 |e_\theta|^2 |e_r|^2 + 0 + 0 + |e_\theta|^2 |e_r|^2 |e_\theta|^2) \\ &= \frac{2h^2}{r^2} \end{aligned}$$

Combining the above, (A.2) becomes:

$$\begin{aligned} |\nabla Q|^2 = \nabla Q : \nabla Q &= |\nabla h|^2 - |\nabla h|^2 + \frac{1}{2}|\nabla h|^2 - \frac{h}{r}\nabla h \cdot e_r + \frac{2}{r^2}h^2 \\ &= \frac{1}{2}|\nabla h|^2 - \frac{h}{r}\nabla h \cdot e_r + \frac{2}{r^2}h^2 \\ &= \frac{1}{2}|\nabla h|^2 - (e_r \frac{\partial}{\partial r} + \frac{e_\theta}{r}\frac{\partial}{\partial \theta})h \cdot e_r + \frac{2}{r^2}h^2 \end{aligned} \tag{A.3}$$

Since h is only dependent on r, (A.3) can be simplified further:

$$|\nabla Q|^2 = \frac{h'^2}{2} - \frac{h}{r}h' + \frac{2h^2}{r^2} \tag{A.4}$$

We also rewrite the bulk terms in terms of h and e_r:

$$\begin{aligned}
\text{tr } (Q^2) = |Q|^2 = Q : Q &= h^2(e_r \otimes e_r - \frac{1}{2}I) : (e_r \otimes e_r - \frac{1}{2}I) \\
&= h^2(e_r \otimes e_r : e_r \otimes e_r - e_r \otimes e_r : I + \frac{1}{4}I : I) \\
&= h^2[|e_r|^2|e_r|^2 - (e_r)_i(e_r)_j\delta_{ij} + \frac{1}{4}\delta_{ij}\delta_{ij}] \\
&= h^2(1 - 1 + \frac{1}{2}) = \frac{h^2}{2} \\
\text{tr } (Q^2)^2 = (|Q|^2)^2 &= \frac{h^4}{4}
\end{aligned} \tag{A.5}$$

Combining (A.4) and (A.5), the liquid crystal energy over a disc of radius R is rewritten in the following way:

$$\begin{aligned}
I[h] &= \int_0^{2\pi}\int_0^R \left[\frac{1}{2}(\frac{h'^2}{2} - \frac{h}{r}h' + \frac{2h^2}{r^2}) - \frac{1}{2}\frac{h^2}{2} + \frac{1}{4}\mathcal{C}\frac{h^4}{4}\right] \, r \, dr \, d\theta \\
&= \pi\int_0^R r\left[\frac{h'^2}{2} - \frac{h}{r}h' + (\frac{2}{r^2} - \frac{1}{2})h^2 + \mathcal{C}\frac{h^4}{8}\right] \, dr
\end{aligned}$$

A.2 Derivation of $h(\rho)$ in Spherical Coordinates

Assume that Q is the three-by-three matrix given by (4.2) and take as our energy density $\frac{1}{2}|\nabla Q|^2 - \text{tr } Q^2 + \frac{\mathcal{B}}{3}\text{tr } Q^3 + \frac{\mathcal{C}}{4}(\text{tr } Q^2)^2$. Let $Q = h(\boldsymbol{n}_\rho \otimes \boldsymbol{n}_\rho - (1/3)I)$, where h is a function dependent on ρ and $\boldsymbol{n}_\rho$ is the radial basis vector in spherical coordinates, e_ρ. We want to express the Landau-de Gennes energy in terms of h and we begin by rewriting ∇Q:

$$\nabla Q = \nabla[h(e_\rho \otimes e_\rho - \frac{1}{3}I)] = e_\rho \otimes e_\rho \otimes \nabla h - \frac{1}{3}I \otimes \nabla h + h\nabla(e_\rho \otimes e_\rho) \tag{A.6}$$

Therefore $|\nabla Q|^2 = \nabla Q : \nabla Q$ is:

$$\begin{aligned}
\nabla Q : \nabla Q = &(e_\rho \otimes e_\rho \otimes \nabla h : e_\rho \otimes e_\rho \otimes \nabla h) - (\frac{2}{3}e_\rho \otimes e_\rho \otimes \nabla h : I \otimes \nabla h) \\
&+ (2e_\rho \otimes e_\rho \otimes \nabla h : h\nabla(e_\rho \otimes e_\rho)) + (\frac{1}{9}I \otimes \nabla h : I \otimes \nabla h) \\
&- (\frac{2}{3}h\nabla(e_\rho \otimes e_\rho) : I \otimes \nabla h) + (h\nabla(e_\rho \otimes e_\rho) : h\nabla(e_\rho \otimes e_\rho))
\end{aligned} \tag{A.7}$$

Before expanding each term separately, we expand $\nabla(e_\rho \otimes e_\rho)$ in spherical coordinates:

$$\begin{aligned}
\nabla(e_\rho \otimes e_\rho) &= (e_\rho\frac{\partial}{\partial\rho} + \frac{1}{\rho}e_\phi\frac{\partial}{\partial\phi} + \frac{1}{\rho\sin\phi}e_\theta\frac{\partial}{\partial\theta}) \otimes (e_\rho \otimes e_\rho) \\
&= e_\rho \otimes \frac{\partial}{\partial\rho}(e_\rho \otimes e_\rho) + \frac{1}{\rho}e_\phi \otimes \frac{\partial}{\partial\phi}(e_\rho \otimes e_\rho) + \frac{1}{\rho\sin\phi}e_\theta \otimes \frac{\partial}{\partial\theta}(e_\rho \otimes e_\rho)
\end{aligned}$$

$$= \frac{1}{\rho} e_\phi \otimes (\frac{\partial}{\partial \phi} e_\rho \otimes e_\rho + e_\rho \otimes \frac{\partial}{\partial \phi} e_\rho) + \frac{1}{\rho \sin \phi} e_\theta \otimes (\frac{\partial}{\partial \theta} e_\rho \otimes e_\rho + e_\rho \otimes \frac{\partial}{\partial \theta} e_\rho)$$
$$= \frac{1}{\rho} e_\phi \otimes (e_\phi \otimes e_\rho + e_\rho \otimes e_\phi) + \frac{1}{\rho \sin \phi} e_\theta \otimes (\sin \phi)(e_\theta \otimes e_\rho + e_\rho \otimes e_\theta)$$
$$= \frac{1}{\rho}(e_\phi \otimes e_\phi \otimes e_\rho + e_\phi \otimes e_\rho \otimes e_\phi) + \frac{1}{\rho}(e_\theta \otimes e_\theta \otimes e_\rho + e_\theta \otimes e_\rho \otimes e_\theta)$$
$$= \frac{1}{\rho}(e_\phi \otimes e_\phi \otimes e_\rho + e_\phi \otimes e_\rho \otimes e_\phi + e_\theta \otimes e_\theta \otimes e_\rho + e_\theta \otimes e_\rho \otimes e_\theta)$$

Now, we rewrite the six terms of $\nabla Q : \nabla Q$.

$$e_\rho \otimes e_\rho \otimes \nabla h : e_\rho \otimes e_\rho \otimes \nabla h = |\nabla h|^2$$

$$\frac{-2}{3} e_\rho \otimes e_\rho \otimes \nabla h : I \otimes \nabla h = \frac{-2}{3}(e_\rho)_i (e_\rho)_j \nabla h_k \delta_{ij} \nabla h_k = \frac{-2}{3}|\nabla h|^2$$

$$2e_\rho \otimes e_\rho \otimes \nabla h : h\nabla(e_\rho \otimes e_\rho) = 2h(e_\rho \otimes e_\rho \otimes \nabla h) : [\frac{1}{\rho}(e_\phi \otimes e_\phi \otimes e_\rho + e_\phi \otimes e_\rho \otimes e_\phi + e_\theta \otimes e_\theta \otimes e_\rho + e_\theta \otimes e_\rho \otimes e_\theta)]$$
$$= 2h(e_\rho \otimes e_\rho \otimes \nabla h) : 0 = 0$$

$$\frac{1}{9} I \otimes \nabla h : I \otimes \nabla h = \frac{1}{9} \delta_{ij} \nabla h_k \delta_{ij} \nabla h_k = \frac{1}{3}|\nabla h|^2$$

$$\frac{-2}{3} h\nabla(e_\rho \otimes e_\rho) : I \otimes \nabla h = \frac{-2}{3} hI \otimes \nabla h : \nabla(e_\rho \otimes e_\rho)$$
$$= \frac{-2}{3} hI \otimes \nabla h : [\frac{1}{\rho}(e_\phi \otimes e_\phi \otimes e_\rho + e_\phi \otimes e_\rho \otimes e_\phi + e_\theta \otimes e_\theta \otimes e_\rho + e_\theta \otimes e_\rho \otimes e_\theta)]$$
$$= \frac{-2}{3} hI \otimes \nabla h : [\frac{1}{\rho}(e_\phi \otimes e_\phi \otimes e_\rho + e_\theta \otimes e_\theta \otimes e_\rho)]$$
$$= \frac{-2}{3\rho} h(\delta_{ij} \nabla h_k (e_\phi)_i (e_\phi)_j (e_\rho)_k + \delta_{ij} \nabla h_k (e_\theta)_i (e_\theta)_j (e_\rho)_k)$$
$$= \frac{-2}{3\rho} h \nabla h \cdot e_\rho$$

$$h^2 \nabla(e_\rho \otimes e_\rho) : \nabla(e_\rho \otimes e_\rho) = h^2 [\frac{1}{\rho}(e_\phi \otimes e_\phi \otimes e_\rho + e_\phi \otimes e_\rho \otimes e_\phi + e_\theta \otimes e_\theta \otimes e_\rho + e_\theta \otimes e_\rho \otimes e_\theta)] : [\frac{1}{\rho}(e_\phi \otimes e_\phi \otimes e_\rho + e_\phi \otimes e_\rho \otimes e_\phi + e_\theta \otimes e_\theta \otimes e_\rho + e_\theta \otimes e_\rho \otimes e_\theta)]$$
$$= \frac{h^2}{\rho^2}(e_\phi \otimes e_\phi \otimes e_\rho : e_\phi \otimes e_\phi \otimes e_\rho + e_\phi \otimes e_\rho \otimes e_\phi : e_\phi \otimes e_\rho \otimes e_\phi + e_\theta \otimes e_\theta \otimes e_\rho : e_\theta \otimes e_\theta \otimes e_\rho + e_\theta \otimes e_\rho \otimes e_\theta : e_\theta \otimes e_\rho \otimes e_\theta)$$

$$= \frac{h^2}{\rho^2}(1+1+1+1) = \frac{4}{\rho^2}h^2$$

Since h is just a function of ρ, $\nabla h = [e_\rho(\partial/\partial\rho) + e_\phi(1/\rho)(\partial/\partial\phi) + e_\theta(1/\rho\sin\theta)(\partial/\partial\theta)]h = h'e_\rho$. This simplifies (A.7):

$$\begin{aligned}
|\nabla Q|^2 &= \nabla Q : \nabla Q \\
&= |\nabla h|^2 - \frac{2}{3}|\nabla h|^2 + \frac{1}{3}|\nabla h|^2 - \frac{2}{3\rho}h\nabla h \cdot e_\rho + \frac{4h^2}{\rho^2} \\
&= \frac{2}{3}|\nabla h|^2 - \frac{2}{3\rho}h(e_\rho\frac{\partial}{\partial\rho} + \frac{1}{\rho}e_\phi\frac{\partial}{\partial\phi}h + \frac{1}{\rho\sin\theta}\frac{\partial}{\partial\theta})h \cdot e_\rho + \frac{4h^2}{\rho^2} \\
&= \frac{2}{3}h'^2 - \frac{2}{3\rho}hh' + \frac{4h^2}{\rho^2}
\end{aligned} \tag{A.8}$$

We also expand the bulk terms and express them in terms of h:

$$\begin{aligned}
\text{tr } Q^2 = |Q|^2 = Q : Q &= h^2(e_\rho \otimes e_\rho - \frac{1}{3}I) : (e_\rho \otimes e_\rho - \frac{1}{3}I) \\
&= h^2(e_\rho \otimes e_\rho : e_\rho \otimes e_\rho - \frac{2}{3}I : e_\rho \otimes e_\rho + \frac{1}{9}I : I) \\
&= h^2(1 - \frac{2}{3}\delta_{ij}(e_\rho)_i(e_\rho)_j + \frac{1}{3}) \\
&= h^2(1 - \frac{2}{3} + \frac{1}{3}) = \frac{2}{3}h^2 \\
\text{tr } (Q^2)^2 &= (\frac{2}{3}h^2)^2 = \frac{4}{9}h^4
\end{aligned} \tag{A.9}$$

For tr Q^3, we begin by expanding Q^3:

$$\begin{aligned}
Q^3 &= h(e_\rho \otimes e_\rho - \frac{1}{3}I)_{ij}h(e_\rho \otimes e_\rho - \frac{1}{3}I)_{jk}h(e_\rho \otimes e_\rho - \frac{1}{3}I)_{kl} \\
&= h^3[(e_\rho \otimes e_\rho)_{ij}(e_\rho \otimes e_\rho)_{jk} - \frac{2}{3}(e_\rho \otimes e_\rho)_{ik} + \frac{1}{9}\delta_{ik}](e_\rho \otimes e_\rho - \frac{1}{3}I)_{kl} \\
&= h^3(\frac{1}{3}e_\rho \otimes e_\rho + \frac{1}{9}I)_{ik}(e_\rho \otimes e_\rho - \frac{1}{3}I)_{kl} \\
&= h^3[\frac{1}{3}(e_\rho \otimes e_\rho)_{ik}(e_\rho \otimes e_\rho)_{kl} - \frac{1}{9}(e_\rho \otimes e_\rho)_{il} + \frac{1}{9}(e_\rho \otimes e_\rho)_{il} - \frac{1}{27}I_{il}] \\
&= h^3[\frac{1}{3}(e_\rho \otimes e_\rho) - \frac{1}{27}I]
\end{aligned}$$

Taking the trace gives:

$$\begin{aligned}
\text{tr } Q^3 &= \text{tr } (h^3(\frac{1}{3}(e_\rho \otimes e_\rho) - \frac{1}{27}I)) \\
&= \frac{h^3}{3}(e_\rho \otimes e_\rho - \frac{1}{9}I)_{ii} \\
&= \frac{h^3}{3}[(e_\rho \otimes e_\rho)_{ii} - 1/3] \\
&= \frac{h^3}{3}[(\cos\theta \sin\phi)^2 + (\sin\theta \sin\phi)^2 + (\cos\phi)^2 - 1/3] \\
&= \frac{h^3}{3}(\sin^2\phi + \cos^2\phi - 1/3) \\
&= \frac{h^3}{3}(1 - 1/3) = \frac{2}{9}h^3
\end{aligned} \tag{A.10}$$

From (A.8), (A.9), and (A.10), we can express the Landau-de Gennes integral energy expression over a sphere of radius R as:

$$\begin{aligned}
I[h] &= \int_0^R \int_0^\pi \int_0^{2\pi} \left[\frac{1}{2}(\frac{2}{3}h'^2 - \frac{2}{3\rho}hh' + \frac{4h^2}{\rho^2}) - \frac{2}{3}h^2 + \frac{\mathcal{B}}{3}\frac{2}{9}h^3 + \frac{\mathcal{C}}{4}\frac{4}{9}h^4\right] \rho^2 \sin\phi \; d\theta d\phi d\rho \\
&= \int_0^R \int_0^\pi \int_0^{2\pi} \left[\frac{1}{3}h'^2 - \frac{1}{3\rho}hh' + (\frac{2}{\rho^2} - \frac{2}{3})h^2 + \frac{2\mathcal{B}}{27}h^3 + \frac{\mathcal{C}}{9}h^4\right] \rho^2 \sin\phi \; d\theta d\phi d\rho \\
&= \int_0^R \int_0^\pi 2\pi \left[\frac{1}{3}h'^2 - \frac{1}{3\rho}hh' + (\frac{2}{\rho^2} - \frac{2}{3})h^2 + \frac{2\mathcal{B}}{27}h^3 + \frac{\mathcal{C}}{9}h^4\right] \rho^2 \sin\phi \; d\phi d\rho \\
&= \int_0^R 4\pi \left[\frac{1}{3}h'^2 - \frac{1}{3\rho}hh' + (\frac{2}{\rho^2} - \frac{2}{3})h^2 + \frac{2\mathcal{B}}{27}h^3 + \frac{\mathcal{C}}{9}h^4\right] \rho^2 \; d\rho
\end{aligned}$$

A.3 Derivation of $h(r)$ in Cylindrical Coordinates

We assume that Q is the three-by-three matrix given by (4.2) and consider the energy density $\frac{1}{2}|\nabla Q|^2 - \text{tr } Q^2 + \frac{\mathcal{B}}{3}\text{tr } Q^3 + \frac{\mathcal{C}}{4}(\text{tr } Q^2)^2$. This derivation will be similar to that done for spherical coordinates in Section A.2 and the general expression for $\nabla Q : \nabla Q$ will look identical with r replacing ρ:

$$\begin{aligned}
\nabla Q : \nabla Q = (e_r \otimes e_r \otimes \nabla h : e_r \otimes e_r \otimes \nabla h) &- (\frac{2}{3}e_r \otimes e_r \otimes \nabla h : I \otimes \nabla h) \\
&+ (2e_r \otimes e_r \otimes \nabla h : h\nabla(e_r \otimes e_r)) + (\frac{1}{9}I \otimes \nabla h : I \otimes \nabla h) \\
&- (\frac{2}{3}h\nabla(e_r \otimes e_r) : I \otimes \nabla h) + (h\nabla(e_r \otimes e_r) : h\nabla(e_r \otimes e_r)),
\end{aligned}$$

where e_r is the radial basis vector for cylindrical coordinates. When we expand these terms, many will be similar to the spherical case, but care must be taken when the terms involve

$\nabla(e_r \otimes e_r)$. Using the fact that in cylindrical coordinates, $\nabla = e_r\partial/\partial r + e_\theta(1/r)\partial/\partial\theta + e_z\partial/\partial z$, we have

$$\begin{aligned}(e_r\frac{\partial}{\partial r} + e_\theta\frac{1}{r}\frac{\partial}{\partial\theta} + e_z\frac{\partial}{\partial z}) \otimes (e_r \otimes e_r) &= e_\theta \otimes \frac{1}{r}(\frac{\partial}{\partial\theta}e_r \otimes e_r + e_r \otimes \frac{\partial}{\partial\theta}e_r) \\ &= \frac{1}{r}(e_\theta \otimes e_\theta \otimes e_r + e_\theta \otimes e_r \otimes e_\theta).\end{aligned}$$

Any term in $|\nabla Q|^2$, which do not involve $\nabla(e_r \otimes e_r)$ will be equal to those the spherical case with r replacing ρ, and therefore we only need to expand the 3rd, 5th and 6th terms:

$$\begin{aligned}2e_r \otimes e_r \otimes \nabla h : h\nabla(e_r \otimes e_r) &= 2he_r \otimes e_r \otimes \nabla h : \frac{1}{r}(e_\theta \otimes e_\theta \otimes e_r + e_\theta \otimes e_r \otimes e_\theta) \\ &= 0\end{aligned}$$

$$\begin{aligned}\frac{-2}{3}h\nabla(e_r \otimes e_r) : I \otimes \nabla h &= \frac{-2}{3}hI \otimes \nabla h : \nabla(e_r \otimes e_r) \\ &= \frac{-2}{3}hI \otimes \nabla h : \frac{1}{r}(e_\theta \otimes e_\theta \otimes e_r + e_\theta \otimes e_r \otimes e_\theta) \\ &= \frac{-2h}{3r}\delta_{ij}\nabla h_k((e_\theta)_i(e_\theta)_j(e_r)_k + (e_\theta)_i(e_r)_j(e_\theta)_k) \\ &= \frac{-2h}{3r}|e_\theta|^2\nabla h \cdot e_r \\ &= \frac{-2h}{3r}\nabla h \cdot e_r\end{aligned}$$

$$\begin{aligned}h^2\nabla(e_r \otimes e_r) : \nabla(e_r \otimes e_r) &= \frac{h^2}{r^2}(e_\theta \otimes e_\theta \otimes e_r + e_\theta \otimes e_r \otimes e_\theta) : (e_\theta \otimes e_\theta \otimes e_r + e_\theta \otimes e_r \otimes e_\theta) \\ &= \frac{h^2}{r^2}(e_\theta \otimes e_\theta \otimes e_r : e_\theta \otimes e_\theta \otimes e_r + e_\theta \otimes e_r \otimes e_\theta : e_\theta \otimes e_r \otimes e_\theta) \\ &= \frac{2h^2}{r^2}\end{aligned}$$

Since h depends only on r, $\nabla h = (e_r\frac{\partial}{\partial r} + e_\theta\frac{1}{r}\frac{\partial}{\partial\theta} + e_z\frac{\partial}{\partial z})h = h'e_r$ and

$$\begin{aligned}|\nabla Q|^2 &= \nabla Q : \nabla Q \\ &= \frac{2}{3}|\nabla h|^2 - \frac{2h}{3r}h' + \frac{2h^2}{r^2}\end{aligned}$$

The expansion of the bulk terms will not vary from Section A.2 and the integral energy expression over a cylinder of radius R and height K can be expressed in the following way:

$$\begin{aligned}I[h] &= \int_0^K \int_0^{2\pi} \int_0^R \left[\frac{1}{3}h'^2 - \frac{hh'}{3r} + (\frac{1}{r^2} - \frac{2}{3})h^2 + \frac{2\mathcal{B}}{27}h^3 + \frac{\mathcal{C}}{9}h^4\right]\ r\ dr\ d\theta\ dz \\ &= 2\pi K \int_0^R \left[\frac{1}{3}h'^2 - \frac{hh'}{3r} + (\frac{1}{r^2} - \frac{2}{3})h^2 + \frac{2\mathcal{B}}{27}h^3 + \frac{\mathcal{C}}{9}h^4\right]\ r\ dr\end{aligned}$$